Design of a Permanent Magnet Generator for a Sustainable Wind Energy Capture and Storage System

by

Hartmut Jagau

A dissertation submitted to the Department of Electrical Engineering, University of Cape Town, in complete fulfillment of the requirements for the degree of

Masters of Science in Engineering

September 2011

Declaration

I know the meaning of plagiarism and declare that all the work in the present document, save for that which is properly acknowledged, is my own. This dissertation is submitted to the Department of Electrical Engineering, University of Cape Town, in complete fulfillment of the requirements for the degree of Master of Science in Electrical Engineering. It has not been previously submitted in any form to the University of Cape Town or any other institution for assessment for any other purpose.

Signed by candidate

....

Hartmut Jagau Date

Acknowledgments

First and above all, I give all the glory to Yahweh, my gracious father in heaven and to his beloved son Jesus Christ, who saved me by pure grace alone. I thank my God for providing me with the opportunity and granting me the capability to successfully complete this work. I have grown incredibly during the process of completing this degree and I am excited about what God has installed for me in the future.

A research project is never the work of one alone. The contributions of many people, each in their unique way, have made this dissertation possible. I would like to express my deepest appreciation and gratitude to those who supported me in any respect during the completion of the project.

I am heartily thankful to my supervisor Dr. M.A. Khan and my co-supervisor Dr. P.S. Barendse for their assistance and guidance throughout the process of this work. I want to thank Dr. Khan whose help, stimulating suggestions, encouragement and genuineness made my work very enjoyable. I want to acknowledge Chris for the patience and kindness, which he has shown me throughout my studies by always being available to help me. I also want to thank Philip for his assistance in the laboratory. I am deeply indebted to my dear friend Wanjiku, who helped me in every way during this dissertation; from teaching me invaluable insights in the machine design field to proof reading this work. And besides that, I don't know how I can thank you for your willingness to always help me finish the too big lunches that Anneke prepared for me. Ernest, it was a privilege to walk the Masters road with you. Your incredible calmness and optimism are very inspirational and have given me much joy. I also want to thank Marlene of the Electrical Engineering department for all your work to manage our numerous investments in the machine laboratory.

To my dear friends from the AMES family who supported me in my research work. Ashwill, Henry, Jaques, Direshni, Barbz, Manuela, Akrama, Richard and the rest of the AMES family, I want to thank you for your support, help, valuable hints and encouragement.

My earnest appreciation goes to my Christian brothers and sisters in our Small Group. Michael, Nelleke, Zane, Sunette, Rianna and Ian, you have truly become our family. Thanks for your friendship and for making us feel home in Cape Town. I also want to thank my dear friend Dana, my grandmother Omingel and my mom for their daily prayers throughout my entire life. Your faithful prayers have been answered by our God over and over and are carrying me every day.

And of course, I would like to express my deepest gratitude to my family for their ongoing support throughout my entire studies. What a privilege to have a mom and dad, who care and provide for you. I cannot thank my dad enough for working so incredible hard in order to provide for our family.

My greatest appreciation is for my dear wife, Anneke. Being able to call you my wife fills me with an incredible joy. Your continuous encouragement, love, faithfulness and patience are truly appreciated.

Lastly, this dissertation would not have been possible without the financial assistance from TUCSIN/DAAD.

Abstract

Renewable energy is the fastest growing source of electricity generation in the world. This considerable growth in the renewable energy sector is contributing to sustainable development, environmental conservation and most importantly providing affordable energy to remote rural communities in developing countries. Small-scale renewable energy solutions, such as wind and solar, are particularly well suited for generating small amounts of electricity in these remote areas. Unfortunately, conventional small-scale renewable energy solutions are still very expensive and cheaper solutions need to be developed. Contrary to the many deficiencies the world is experiencing today, electrical and electronic waste (e-waste) is being produced and accumulated at an alarming rate. In fact, e-waste is one of the fastest growing waste streams in the world. E-waste is loaded with contaminants, which poses a threat to the environment.

This dissertation proposes a sustainable low-cost wind energy system that can generate and store small amounts of electricity in remote locations. The system components are built from cheap, readily available and recycled e-waste materials, achieving the sustainability. A topology for the sustainable wind energy capture and storage system is presented and a sizing methodology for the system components is developed. A wind energy conversion system captures wind energy to supply a low-power demand household. The excess electrical energy is stored in an electromechanical flywheel and is made available when the wind generator does not meet the demand of the household.

The main objective of this dissertation is the detailed design, sizing, analysis and experimental validation of the sustainable wind generator. The proposed machine topology for the generator uses permanent magnets (PMs) from discarded hard disk drives (HDDs). The PM configuration inherently produces a non-uniform airgap flux-density distribution and the pole pitches of the PMs are relatively small. This would result to an unbalanced generator output and a number of stator inter-connecting leads, if conventional tooth-concentrated non-overlapping winding configurations are used. Hence, a concentrated full-pitch overlapping wave winding configuration is developed, which overcomes the aforementioned challenges.

The proposed sustainable coreless axial flux generator is then analyzed with classical machine theory and verified by finite element analysis (FEA) software. It is shown that the traditional sizing approach for axial flux machines needs modification to accommodate the design of the proposed machine topology. For the numerical analysis, 3D-FEA is used to verify the 2D model which is subsequently employed in the numerical analyses.

It was shown that by reusing and recycling e-waste, 11.4 Wh of electrical energy can be stored in the flywheel. With no wind, the flywheel can supply 14 W to the household for up to 12 min. At rated wind speed of 8 m/s, the generator needs to have an output power of 277 W when loaded with a phase current of 3 A. At this specific loading point, the shaft speed and phase voltage of the generator were 347 rpm and 30.78 V respectively. Two generator stages connected in series met the requirements, of which one was prototyped and tested.

The experimental results obtained from the 3-phase prototype compared well with the theoretical and numerical results. The generator had a poor voltage regulation and the copper losses were excessive, which can be attributed to the relatively high phase resistance of 3.33 Ω associated with the overlapping winding configuration. The output power of the experimental generator at a shaft speed of 600 rpm and a load current of 3.3 A was 328 W. Its efficiency at this specific loading point was 70.2 %, which is acceptable for small machines. Therefore, it can be concluded that a reasonable amount of electrical energy can be generated and stored by implementing the proposed wind energy capture and storage system built from sustainable materials.

The phase resistance and the associated copper losses of the overlapping concentrated full-pitch wave winding were relatively high, methods to minimize the resistance should be explored. The tooth-concentrated single layer non-overlapping winding configuration with unequal tooth widths should be investigated, since they have less copper losses and could minimize voltage unbalance.

Contents

List of Figures

List of Tables

Nomenclature

The following constants, symbols and abbreviations are used throughout the work.

Constants

Symbol	Value and Unit	Definition
μ_0	$= 4\pi \times 10^{-7}\,\mathrm{Vs/Am}$	Permeability of vacuum
μ_{air}	$= 1.8 \times 10^{-5}\,\mathrm{Pa\,s}$	Dynamic viscosity of air at 1atm and 20°C
ρ_{air}	$= 1.2\,\mathrm{kg/m^3}$	Specific mass density of air at 1atm and 20°C
$\rho_{cu,m}$	$= 8960\,\mathrm{kg/m^3}$	Specific mass density of copper at 20°C
$\rho_{cu,R}$	$= 1.68\mathrm{e}^{-8}\,\Omega\mathrm{m}$	Resistivity of copper at 20°C

List of Symbols and Notations

Symbol	Unit	Definition
α_i		Ratio of the average to peak value of the flux-density
δ	m	Skin depth or depth of penetration
ΔP_{core}	W	Core losses
ΔP_{cu}	W	Copper losses
$\Delta P_{e,w}$	W	Eddy current losses in the stator windings
ΔP_{PM}	W	Eddy current losses in the backing plates and PMs
$\Delta P_{rot/f\&w}$	W	Rotational or friction & windage losses
ΔP_{rotor}	W	Eddy current losses in the rotors
ϵ		Phase EMF-to-phase voltage ratio
η	%	Efficiency
η_d		Coefficient of distortion
λ		Tip speed ratios or specific permeance
μ_r		Relative permeability
ω_e	rad/s	Electrical angular speed
ω_{fly}	rad/s	Angular speed of the flywheel
ω_m	rad/s	Mechanical angular speed
ϕ_g	Wb	Airgap flux

Symbol	Unit	Definition
ϕ_M	Wb	Magnet flux
ϕ_p	Wb	Flux per pole
ψ	Wb-turns	Flux Linkage
ρ	kg/m^3	Specific mass density or resistivity of conductor
τ_c	m	Coil pitch
τ_{d1}		Differential leakage factor
τ_m	s	Mechanical time constant
τ_p	m	Pole pitch
θ_{re}	deg	Coil-width-angle
ξ_v	W/m^3	Power density of the machine related to its volume
ξ_m	W/kg	Power density of the machine related to its mass
A_g	m^2	Airgap area
A_M	m^2	Area of the magnets
A_s	A/m	Peak specific electric loading
B	kg m^2/s	Equivalent viscous friction constant
B_{avg}	T	Average airgap flux-density
B_{mg}	T	Peak/plateau value of airgap flux-density
b_p	m	Magnet/pole arc
B_r	T	Remanent flux-density
C_ϕ		Flux focusing/concentration factor
C_p		Aerodynamic efficiency
c_f		Coefficient of drag for turbulent flow
d	m	Diameter of conductor
E_{fly}	Wh	Energy stored in the flywheel
E_f or EMF	V	No-load back-EMF per phase
f	Hz	Electrical frequency
F_D	N	Drag Force
F_L	N	Lift Force
f_{LKG}		Leakage coefficient
g	m	Effective airgap
g_m	m	Mechanical airgap
g'	m	Equivalent airgap
h_M	m	Height of magnet in the axial direction
h_r	m	Thickness of the rotors
h_w	m	Depth of the stator in the axial direction
I_a	A	RMS phase current
J	kg m^2 or A/mm^2	Mass moment of inertia or current density
k_d		Inner-to-outer PM radius ratio

Symbol	Unit	Definition
k_{fb}	m^2/s^2	Bearing specific coefficient
k_{dn}		n_{th} harmonic distribution factor
k_{pn}		n_{th} harmonic pitch factor
k_{w1}		Fundamental winding factor
k_{wn}		n_{th} harmonic winding factor
L_a	H	Mutual/armature reaction inductance
L_l	H	Leakage inductance
L_s	H	Synchronous inductance
l_a	m	PM length in the radial direction
$l_{a,w}$	m	Active length of stator winding in the radial direction
l_{avg}	m	Average length of a turn
l_e	m	Average end winding length of a turn
l_{in}	m	Length of inner end-winding
l_{out}	m	Length of outer end-winding
l_{stk}	m	Axial stack length
m_1		Number of phases
m_{gen}	kg	Mass of generator
n	rpm	Rotational speed
n_s	rps	Rotational shaft speed
N_c		Number of turns per coil
N_{ph}		Total number of turns per phase
p		Number of poles
P_{ag}	W	Airgap power
P_{el}	W	Electrical output power of generator
P_{in}	W	Input power
P_{out}	W	Output power
$P_{s,bldc}$	W	Shaft powers of the BLDC motor
$P_{s,turb}$	W	Shaft power of the wind turbine
P_{sh}	W	Shaft power of generator
q		Number of slots per pole per phase
Q_c		Number of stator coils
Q_s		Total number of slots
R	m	Radius of the wind turbine
R_{ac}	Ω	AC Winding resistance
R_{dc}	Ω	DC Winding resistance
R_e		Reynolds number for a rotating disc
r_e	m	Average PM radius
r_i	m	Inner PM radius

Symbol	Unit	Definition
r_o	m	Outer PM radius
S_{elm}	VA	Apparent electromagnetic power
T_α	Nm	Accelerating torque
T_{elm}	Nm	Electromagnetic torque
T_{fly}	Nm	Rotational loss torque of the flywheel
$T_{s,bldc}$	Nm	Shaft torque of the BLDC motor

List of Abbreviations

Abbreviation	Definition
AFPM	Axial Flux Permanent Magnet machine
AMES	Advanced Machines and Energy Systems
BLDC	Brushless DC machine
CRO	Continuous Reliable Operation
CRT	Cathode Ray Tube
CSP	Concentrated Solar Thermal Power
DFIG	Doubly Fed Induction Generator
DIY	Do It Yourself
EESG	Electrically Excited Synchronous Generator
EIA	Energy Information Administration
EMF	Electromotive force or the no-load voltage
EU	European Union
eWASA	e-Waste Association of South Africa
e-Waste	Electrical and Electronic Waste
FEA	Finite Element Analysis
GW	Giga Watt
GWh	Giga Watt hour
HAWT	Horizontal Axis Wind Turbine
HDD	Hard Disk Drive
IT	Information Technology
KE	Kinetic Energy
kW	kilo Watt
kWh	kilo Watt hour
LED	Light-Emitting Diode
MDF	Medium Density Fiberboard
MWh	Mega Watt hour
NdFeB	Neodymium-Iron-Boron magnets
PM	Permanent Magnet

Abbreviation	**Definition**
PMSG	Permanent Magnet Synchronous Generator
PV	Photovoltaic
PVC	Polyvinyl Chloride
RE	Renewable Energy
RFPM	Radial Flux Permanent Magnet machine
RMS	Root Mean Square
SCIG	Squirrel-Cage Induction Generator
SEIG	Self-Excited Induction Generator
SG	Synchronous Generator
TSR	Tip Speed Ratio
TWh	Terra Watt hour
US	United States
USD	US Dollars
VAWT	Vertical Axis Wind Turbines
VSD	Variable Speed Drive
WECS	Wind Energy Conversion Systems
WRIG	Wound Rotor Induction Generator
ZAR	South African Rand

Chapter 1

Introduction

1.1 Background

South Africa is currently one of the most economically divided countries in the world. On the one end of society, people can afford to live in developed suburbs and enjoy amenities similar to those in first world countries. In contrast, 36 % (when using the expanded definition, accounting for the discouraged workers) of its population is unemployed and in this group are many people that live in immense poverty [1]. These people lack access to basic services like: sanitation, clean water and electricity. Today, around 2 billion people lack access to electricity worldwide. In South Africa, about 30 % of its population has no access to electricity [2]. Unelectrified areas are usually far away from the grid, or located in mountainous areas, which may not be economically viable to reach. Renewable energy sources, such as wind and solar energy, have the potential to deliver affordable electricity to such areas. However, conventional renewable energy solutions are still very expensive. The Energy Information Administration (EIA) estimates that by 2016 the levelized cost of new generation will be USD 0.0961 per kWh for onshore wind, USD 0.243 per kWh for offshore wind and USD 0.211 per kWh for solar photovoltaic (PV) [3]. The installation cost for onshore wind and solar PV is currently around USD 1400 per kW and USD 2000 per kW respectively [3][4]. Consequently, cheaper renewable energy solutions need to be explored, which can generate small amounts of electricity locally.

Contrary to the many shortages the modern world is experiencing today, waste is being produced and accumulated at a tremendous rate. As a result of the ever increasing need for new, smaller, and faster technology, e-waste is now one of the fastest growing waste streams in the world. E-waste is hazardous and loaded with contaminants that are toxic to the environment. Greenpeace estimates that 20 - 50 million tons of e-waste is discarded globally every year, which makes up 5 % of all municipal solid waste worldwide [5]. According to the US Environmental Protection Agency, discarded electronics in the US totaled about 2 million tons in 2005 [5]. It is estimated that only about 15-20 % of this was recycled [5]. The e-waste Association of South Africa (eWASA) estimates that between 1.1 and 2.1 million tons

of potential e-waste is available for recycling in South Africa annually [6]. A need therefore exists to provide innovative solutions to these unique problems faced in South Africa and other developing countries.

Conservation of energy is particularly encouraged when it is obtained from intermittent renewable sources. The provision of electricity by means of small-scale stand-alone systems will therefore be one of the viable options for improving livelihoods in rural Africa. Energy storage by means of electrochemical batteries or electromechanical flywheels can be used with stand-alone systems to store excess energy or return energy in case the overall system experiences an energy deficit.

This dissertation proposes a low-cost wind energy system that can capture and store electricity in a sustainable manner, whilst also addressing the aforementioned challenges of e-waste. The proposed sustainable wind energy capture and storage system makes use of an axial flux permanent magnet synchronous generator (PMSG) which is directly connected to the wind turbine. The alternating output of the generator is rectified and regulated to a fixed DC bus voltage, from which the DC loads a fed. Excess energy is stored in a flywheel, which supplies the load with electrical power in case the wind generator does not produce enough power. Sustainability of the system is achieved by reusing discarded materials. The wind generator for example, uses PMs from HDDs and the flywheel is built from a used car tire. The dissertation presents a sizing methodology for the complete system, but its main focus is the detailed design of the sustainable wind generator.

1.2 Literature Review

A brief literature review on sustainable low-cost wind generator topologies is presented in this section. The most important winding configurations for sustainable low-cost machines are described, and an appropriate winding configuration for the proposed wind generator topology is presented. The traditional sizing approach for axial flux PM machines is briefly outlined and it is shown that it needs modification to accommodate the design of the proposed machine topology. Lastly, 3D-FEA of axial flux machines is reviewed.

1.2.1 Sustainable Low - Cost Wind Generator Topologies

The main objective of this research is to develop a sustainable low-cost wind generator, which forms a part of the complete sustainable wind energy capture and storage system.

The simplest way to build a low-cost wind generator is to use an automotive alternator as the electrical generator. These are very robust, readily available and can be reused/recycled without any modifications. In [7], a low-cost wind generator concept was developed to meet

the demands of low-income groups in South Africa, which are not connected to the utility grid. This specific alternator produced 78 W when rotated at 1120 rpm. The main problem with using automotive alternators for wind power is that they are designed to rotate at too high speeds to be effective in wind power applications. Implementing a gearbox/pulley system overcomes this challenge, but introduces new challenges, such as high maintenance and losses. Additionally, the brushes and slip rings of the alternator wear out, which requires more maintenance and controlling the field excitation current of the alternators is difficult.

Another candidate for low-cost wind generators is a 3-phase self-excited induction generator (SEIG). Induction machines are cost competitive when compared to other kinds of generators and can also be reused/recycled without any alterations [8]. However, the output voltage of the SEIG is considerably affected by the impedance of the load and the rotor speed, and a controlled converter is required, which regulates the output voltage of the generator [8]. This increases the cost and complexity of the system.

PMSG are most widely used as electrical generators in small-scale wind energy systems. Most of these machines utilize a coreless axial flux machine topology, with high density rare-earth PMs. In [9], a low-cost machine topology, which uses rectangular-shaped magnets, is presented. The generator utilizes a concentrated full-pitch overlapping winding configuration and has an output power of 50 W at 1000 rpm. This speed is high for a direct-drive wind generator operating in low or moderate wind speed regimes, for which the latter generator has been designed. Furthermore, the PMs are manufactured according to the design specification, which reduces its sustainability.

A machine topology that reuses PMs and can produce a reasonable amount of power at lower shaft speeds can be regarded as sustainable and is envisaged. Sustainable wind generators, which reuse the PMs from HDDs and use cheap and readily available materials, have been built by many hobbyist [10][11]. However, these generators are all designed and built intuitively and no methodical design approach is recorded. The poles of the HDD magnets are usually separated from each other, in order to obtain a single N- and S-pole. This magnet configuration will be referred to as “cut magnets”. In so doing, conventional non-overlapping winding configurations can be used. In [12], a single phase generator has been built using the latter machine topology. The generator produced 12.5 W at 450 rpm. The PMs found in HDDs are extremely brittle and separating the two poles is very cumbersome and often deteriorates the PMs. Also, the backing plates of the PMs are discarded, which reduces its sustainability. Thus, a topology, which uses the actual PM configuration found in the HDDs, will be considered in this work. This magnet configuration will be referred to as “uncut magnets”. A low-cost machine, which is constructed with the proposed machine topology, is presented [13]. However, the generator had a relatively low output power, since it was only designed as a single phase machine. Additionally, the generator was not thoroughly tested and no methodical design approach is presented, which will therefore be developed in this dissertation.

1.2.2 Appropriate Winding Configuration for a Sustainable Wind Generator

The most popular choice for the winding configurations of coreless axial flux PM machines is the tooth-concentrated non-overlapping windings. In [14], it is shown that axial flux machines, which have many poles and utilize non-overlapping winding configurations, can have similar or better torque performance than machines with concentrated full-pitch overlapping windings. Additionally, concentrated windings use less copper and consequently have less copper losses.

The uncut HDD magnets of the proposed machine topology inherently produce a non-uniform airgap flux-density distribution, since the magnets/poles do not cover the entire backing plate. As a result, conventional tooth-concentrated non-overlapping winding configurations cannot be utilized, as they produce an unsymmetrical and unbalanced 3-phase output. However, concentrated full-pitch overlapping windings produce a symmetrical and balanced output. The phase coils of conventional coreless axial flux winding configurations are usually pre-formed by means of a bobbin form. The set-back of these winding configurations, when used in machines with many poles and relatively small coil pitches, is the large proportion of coil inter-connecting leads. Hence, a concentrated full-pitch overlapping winding is adapted to resemble a conventional wave winding of brushed DC machines. This winding configuration overcomes the aforementioned challenges and will be referred to as the "concentrated full-pitch overlapping wave winding".

1.2.3 Sizing of Sustainable Axial Flux Machines

The traditional sizing approach for axial flux machines uses the *inner-to-outer PM radius* ratio (k_d) as the sizing parameter [15][16]. This ratio is chosen to meet certain optimized design objectives, e.g. 0.68 for maximum efficiency and about 0.7 for minimum magnet volume [17]. For a machine with a specific output power requirement, the outer radius can then be calculated. With the outer radius and k_d known, the inner PM radius can finally be determined. For machines which use the magnets of HDDs, the ratio k_d can no longer be used as a sizing parameter, since the PM length in the radial direction (l_a) is constant. As a result, k_d is dependent on the outer radius and cannot be set to meet the desired design objective. Hence, the traditional sizing methodology needs to be modified to accommodate the design of the proposed machine topology, which uses l_a as a sizing parameter.

1.2.4 3D-FEA of Axial Flux Machines

During normal operating conditions, axial flux machines exhibit radial, axial and tangential flux components. Due to these complex flux paths and the inherent 3D geometry of axial flux machines, a 3D-FEA model is necessary for accurate analysis of a design [15][18]. Building of

a 3D model is a very time consuming task and extensive computational power is necessary. As a result, 3D analysis of axial flux machines is usually avoided and some literature available. A single sided axial flux PM generator has been analyzed with the 3D-FEA in [19]. The double sided axial flux PM machine topology is most common and some have been analyzed using the 3D-FEA in [18][20][21]. The building process of the 3D models is usually outlined briefly, but none (including the tutorials of the FEA softwares) give a detail account of the modeling process, e.g. information about how the airgap area is meshed. For FE packages that utilize a sliding surface between the rotating parts, the airgap area needs to be meshed very specifically to ensure correct results. The proposed sustainable wind generator is analyzed with the 3D-FEA and the modeling, meshing and simulation procedures are described in detail.

1.3 Research Questions and Objectives

In the process of developing the sustainable wind energy system, together with the detailed design of the sustainable wind generator, the following key questions were formulated:

- What are the most common topologies for sustainable wind energy capture and storage systems?
- Which sustainable materials are effective and readily available to be used for the individual system components?
- What is the most suitable topology for sustainable wind generators, which can be built from redundant materials?
- Which winding configuration overcomes the unsymmetrical voltage production problem when using HDD PMs, and significantly reduces the large proportion of coil interconnecting leads for machines with relatively small coil pitches?
- How does the peculiar shape and magnetization of the HDD PMs affect the electromagnetic performance of the generator?

The objectives of this dissertation can be summarized as follows:

- Develop an appropriate topology for the sustainable wind energy capture and storage system.
- Identify suitable sustainable materials for the individual system components and develop a methodical sizing approach for these components.
- Design and develop a sustainable wind generator topology, which uses uncut HDD magnets and overcomes the challenges associated with this PM configuration.
- Formulate a methodology for designing, sizing and analyzing the proposed sustainable wind generator.

- Analyze and investigate the 3D electromagnetic behavior of the sustainable PM wind generator by means of 3D-FEA.
- Verify the developed machine topology with experimental results.

1.4 Research Significance

The significance of this research to sustainability and low-cost wind energy capture and storage systems includes the following:

- Development of a topology for a sustainable wind energy capture and storage system, which is built from redundant parts and e-waste.
- The developed wind energy system harnesses renewable energy for electricity production, stores excess energy in a sustainable flywheel and returns energy in case the overall system experiences an energy deficit.
- Development of a methodical sizing approach for the individual system components of the sustainable wind energy capture and storage system. The methodology incorporates the experimental results of a prototyped sustainable flywheel in order to size the system components, thereby ensuring a realistic approach to the problem.
- Formulation of a methodology for designing, sizing and analyzing the proposed sustainable wind generator, which uses uncut HDD magnets and utilizes a concentrated full-pitch overlapping winding configuration.
- A methodical sizing approach for the sustainable wind generator is formulated, which uses the PM length in the radial direction as the sizing parameter compared to the conventional sizing approach, which uses the *inner-to-outer PM radius* ratio.
- The developed methodologies are verified by the experimental generator.

1.5 Scope and Limitations

The topology of the sustainable wind energy capture and storage system is presented. A sizing methodology is then presented for each of the system components. However, only the detailed design of the wind generator is considered in the dissertation. Furthermore, the research presented in this dissertation is limited to the electromagnetic design, analysis and performance of the generator.

1.6 Dissertation Outline

The topic and problems associated with this dissertation is introduced in chapter 1.

Chapter 2 presents an overview of the current trends in wind energy systems. The most important utility-scale and small-scale concepts are outlined.

In chapter 3, the sizing methodology of a sustainable wind energy capture and storage system is developed and suitable sustainable materials are identified for the individual system components.

Chapter 4 presents the detailed design of the sustainable wind generator. A sustainable wind generator topology is proposed and a theoretical model is developed.

In chapter 5, the proposed machine topology is analyzed thoroughly by means of 2D- and 3D-FEA.

In chapter 6, the prototyping and testing of the experimental generator is presented and the results obtained from the prototype are discussed and compared with the theoretical and numerical results.

Lastly, the conclusions and recommendations are presented in chapter 7.

Chapter 2

Current Trends in Wind Energy Systems

This chapter reviews the current trends in renewable energy and specifically in wind energy. In addition, utility-scale and small-scale wind energy conversion systems (WECSs) are discussed. Finally, a sustainable wind energy capture and storage system is introduced.

2.1 Renewable Energy

The earth's natural resources are being depleted at an alarming rate. Over 80 % of the global final energy consumption (sum of the energy supplied to the final user for all energy uses, such as transportation, industrial and residential) and approximately 68 % of the global electricity production is generated from fossil fuels, which undeniably will be depleted in the future [22]. Although renewable energy is the fastest growing source of electricity generation, in 2010 it only accounted for 3.3 % of the global electricity consumption, when large-scale hydropower is not included. If large-scale hydropower is included, the figure rises to roughly 20 % [22]. Sweden is leading the renewable energy front with 51 % of its final energy consumption being produced from renewables. On the other hand, the United States and China have a penetration of renewable energy in the final energy consumption of 10.9 % and approximately 9 % respectively [22]. The figures for the electricity generation from renewable energy are generally higher, since the transportation sector and others are still heavily dependent on fossil fuels. In 2010, China produced 18 % of its electricity from renewable sources and India approximately 29 %. It should to be noted that India produces 25 % of its electricity from hydropower and only 4 % is produced from other renewable energy sources [22].

By the end of 2010, wind power had the largest share in the worldwide renewable energy market with 198 GW of installed capacity (63.5 %). Biomass power and solar PV had installed capacities of 62 GW (19.9 %) and 40 GW (12.8 %) respectively [22]. Geothermal power, ocean power, concentrated solar thermal power (CSP) and others make up for the rest of the renewable energy generation mix (3.8 %). The renewable energy generation mix for the total world, developing countries, EU and top five countries is shown Fig. 2.1.

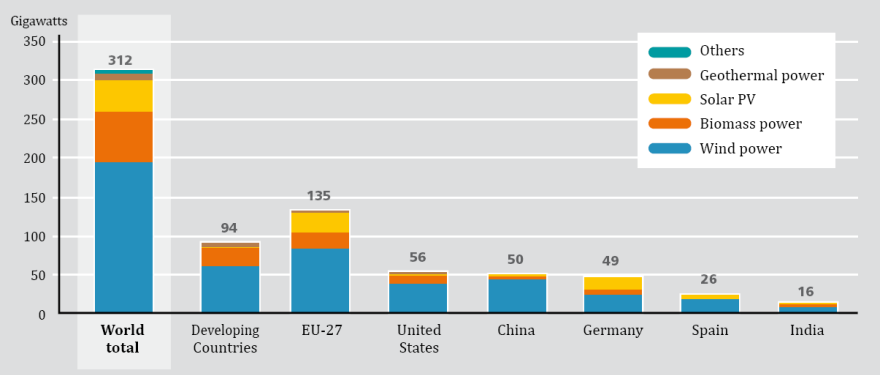

Figure 2.1: Global renewable energy generation mix, excluding hydropower, 2010 [22]

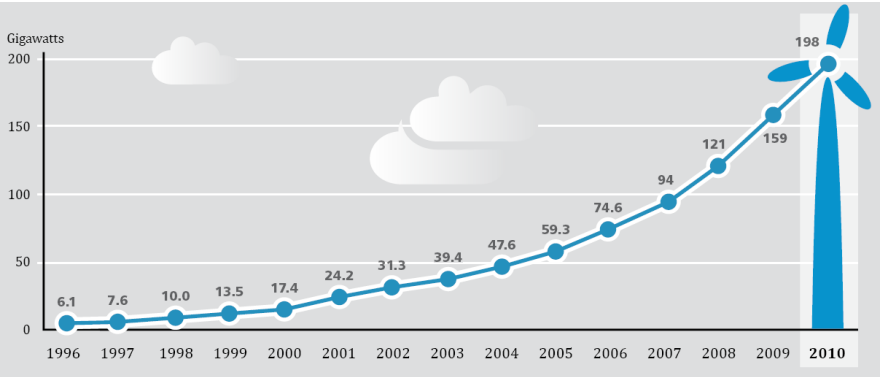

Figure 2.2: Global Wind Power Cumulative Capacity, 1996 - 2010 [22]

2.2 Wind Energy

Wind energy is the world's fastest growing renewable energy source, which had an average annual growth rate of appropriately 30 % during the last ten years. Furthermore, the net installed wind capacity has grown from 121 GW to 159 GW between 2008 and 2009. This translates to a 31.4 % increase in wind capacity [22][23]. This rapid growth trend in wind capacity is clearly visible in Fig. 2.2. In 2010, China had the largest share of the installed capacity, by having overtaken long time leader Germany and the United States as shown in Fig. 2.3 [23]. The Chinese market represents more than half of the world market for new wind turbine installations. In 2010 China installed 18.9 GW of wind capacity, which was equal to 50.3 % of the global installed capacity during that year [22][23]. Despite this significant penetration of wind power, only 1 % of China's electricity consumption was from wind. However, it should be noted that this electricity consumption is twice as much as the previous year [22]. Denmark is the country with the highest penetration of wind power for electricity production (22 %), followed by Portugal (21 %), Spain (15.4 %), Ireland (10.1 %) and Germany (6 %) [22]. The wind farms in Spain produced more electricity (43 TWh) than in Germany (36.5 TWh), despite having less wind capacity in operation. This is mainly due

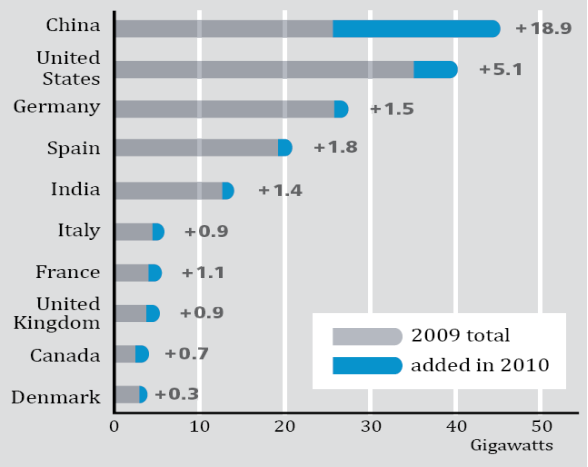

Figure 2.3: Wind Power Capacity - Top 10 countries, 2010 [22]

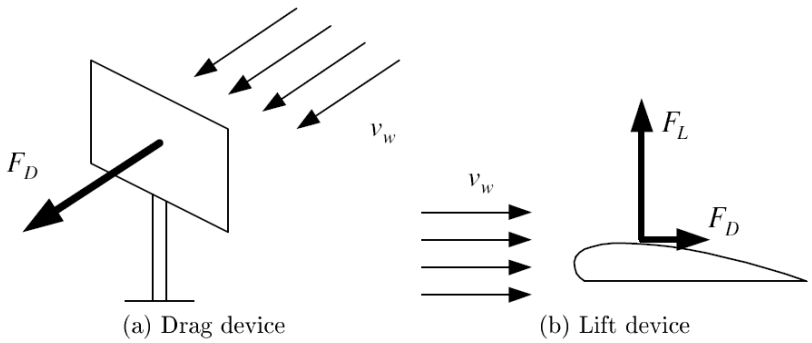

Figure 2.4: Figures of drag and lift devices [24]

to the high wind speeds in Spain and to more advanced turbine technologies, which highlights the importance of choosing the appropriate technology and site for the turbines [22].

2.3 Wind Energy Conversion Systems

The first attempt to generate electricity by means of a wind turbine with aerodynamically formed rotor blades was made over half a century ago. After the 1960s, cheaper fossil fuels made wind energy technology economically uninteresting, and it was only in the 1970s that it returned to the spotlight due to rising fuel prices [25]. However, a rapid increase in the development of new technologies and the roll-out thereof is clearly noticeable from the 1990s onwards. This growth is mainly driven by the increasing awareness of the importance of environmentally friendly technologies, which offer a considerable scope for the reduction of the ever-increasing environmentally damaging emissions.

The kinetic energy in the wind is captured by the wind turbine, which converts it into

(a) HAWT supported by guy wires

(b) VAWT mounted on top of a building

Figure 2.5: Commercial small-scale wind turbines

mechanical energy. The incident wind strikes the blades of the turbine, thereby exerting a drag force and a lift force onto the blades. For turbines with high drag coefficients, the drag force (F_D) is dominant over the lift force (F_L) and are therefore known as drag devices as shown in Fig. 2.4a. These operate at low tip speed ratios (typically: $1 \leq \lambda \leq 2$) and have low aerodynamic efficiencies ($C_p < 0.2$) [26]. The tip speed ratio (λ) is the ratio of the linear speed of the tip of a turbine blade to the actual speed of the wind and can be expressed by eqn (3.7). For lift devices, the lift force is dominant over the drag force and the resultant lift force is converted into mechanical energy. This is illustrated in Fig. 2.4b. Lift devices operate at much higher tip speed ratios (typically: $4 \leq \lambda \leq 7$) and have higher aerodynamic efficiencies (typically: $0.25 \leq C_p \leq 0.4$) than that of drag devices [27][28].

Wind turbines can be classified into vertical axis wind turbines (VAWT) and horizontal axis wind turbines (HAWT), depending on the orientation of the turbine's axis. The three-bladed HAWT concept is the most popular concept for small and large-scale WECS. This concept seems to be the obvious choice from a power delivery and financial perspective. In order for a HAWT to be rotated by the wind, the turbine is required to face the incident wind. This is achieved by means of a tail vane or automatic yawing. The yaw mechanism is not required for the VAWT concept, thereby reducing its cost. This often favors the use of VAWTs in small-scale applications.

WECSs are generally separated into 2 main categories, which include: utility-scale (large-scale) and small-scale systems. The rated output power of utility-scale systems ranges from 50 to 7500 kW, and small-scale having output powers less than 50 kW. The E-126 wind turbine,

manufactured by German producer ENERCON, is a direct-drive system with a rated output power of 7.5 MW [29], but the 3 MW systems are most widely installed. Small-scale systems are usually installed in isolated locations for end-user applications, such as PCs, radios and lightning. Fig. 2.5 shows a small-scale HAWT supported by guy wires and a VAWT mounted on top of a building.

2.3.1 Utility-Scale WECS Concepts

Various wind turbine concepts have been developed and different wind generators have been built in the megawatt range. These are generally classified on the basis of the rotational speed, rating of the power electronic converter and drive train components, and can be summarized as follows:

1. Rotational speed of the wind turbine:
    a) fixed speed
    b) limited variable speed
    c) variable speed
2. Rating of power electronic converter relative to the generator capacity:
    a) partial-rating
    b) full-rated power electronic converter
3. Topology of the drive train:
    a) geared-drive
        i. single-stage gearbox
        ii. multi-stage gearbox
    b) direct-drive

The most common utility-scale concepts are the fixed-speed wind turbine with a squirrel-cage induction generator (SCIG), the variable-speed wind turbine with a doubly fed induction generator (DFIG) and the variable-speed wind turbine connected directly to a synchronous generator (SG). Fig. 2.6a shows the share of different wind turbine concepts in the yearly installed wind power capacity. It can be seen that the DFIG concept is preferred over the SCIG concept, which is due to its wider operating speed range. The limited variable-speed wound rotor induction generator (WRIG) concept seems to be outdated and is slowly losing its share of the wind energy market as shown in Figs. 2.6a and 2.6b. On the other hand, direct-drive concepts such as the electrically excited synchronous generator (EESG) and the PMSG are

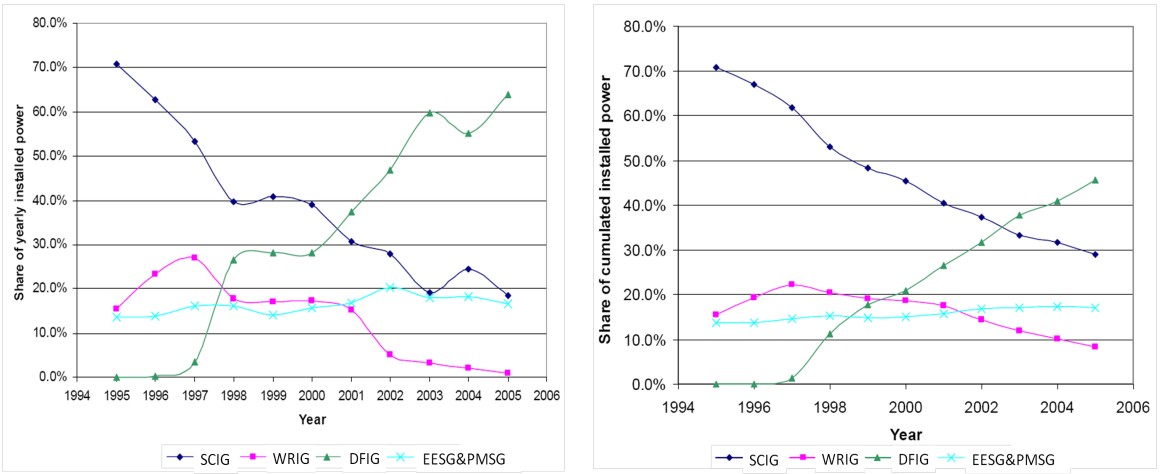

(a) Yearly installed wind power capacity **(b)** Cumulative installed wind power

Figure 2.6: World share of different wind turbine concepts [30]

becoming more interesting since the gearbox is omitted. This concept experiences a slow but steady increase over the past years, which is noticeable when looking at the cumulative installed capacity worldwide as shown in Fig. 2.6b. Furthermore, their technology seems very promising for large wind farms, in which the future for wind energy lies [30].

Considering the penetration of the different concepts in the market, three concepts will only be considered in this work, i.e. SCIG, DFIG and PMSG. In [31] these concepts have been thoroughly described and will briefly be summarized in the following paragraphs.

2.3.1.1 Fixed-Speed SCIG Concept

This concept utilizes a fixed-speed SCIG which is directly connected to the utility grid via a transformer as shown in Fig. 2.7. The speed of the generator is not controllable, since the SCIG only operates closely above synchronous speed. In order to allow for a more variable speed operation, the system is equipped with a multiple-stage gearbox. The SCIG concept has some disadvantages. The wind speed fluctuations result in direct torque pulsation, which cause high mechanical and fatigue stresses on the system. The three-stage gearbox represents a large fraction of the investment costs and a large mass in the nacelle. Furthermore, the

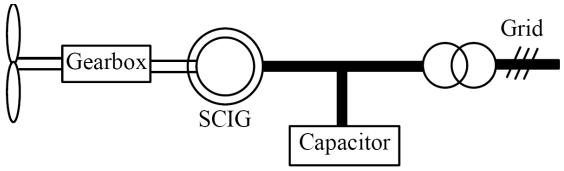

Figure 2.7: Scheme of a fixed-speed concept with SCIG system [31]

system always draws reactive power from the grid, which makes it impossible to support grid voltage [31]. In order to compensate for the reactive power consumption, capacitors are connected in parallel as illustrated in Fig. 2.7 [31]. However, the SCIG is robust, easy and relatively cheap to manufacture and therefore still has a large market share [30].

2.3.1.2 Variable-Speed DFIG Concept

A variation of the of the SCIG is the DFIG and is the most popular choice in current wind generation installations [30][32]. The DFIG concept is a variable speed wind turbine with a WRIG and a partial-rating power electronic converter as illustrated in Fig. 2.8. The converter is connected to the rotor circuit and consequently only needs to be rated at 25-30 % of the generator capacity. It controls the frequency of the wound rotor of the generator. This allows the system to operate over a wider speed range, which is typically ±30 % around the synchronous speed [32]. This concept can perform reactive power compensation and consequently has the capability to support the grid voltage. Moreover, the energy in the rotor windings can be fed back into the grid via the converter. However, a multi-stage gearbox is still required since the speed range of the DFIG is much higher than the turbine speed. The slip rings used to transfer power from the rotor, require regular maintenance and reduce the reliability of the system.

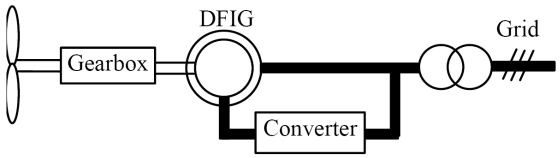

Figure 2.8: Scheme of a variable-speed concept with DFIG system [31]

2.3.1.3 Variable-Speed Direct-Drive Concept

The newest trend in wind generator concepts is the direct-drive (gearless) systems. In these systems a wind turbine is coupled directly to a SG, which is connected to the utility grid via a full-rated power electronic converter. The concept is illustrated in Fig. 2.9. The SG can either make use of a wound rotor that is electrically excited (EESG), or PMs can provide for the necessary excitation flux (PMSG). The generator rotates at low speeds, since it is directly coupled to the wind turbine and therefore needs to produce a high torque. Consequently, the generator size and volume increases substantially [31]. Advantages of direct-drive systems are the simplified drive train, high overall efficiency, reliability and low maintenance due to the absence of the gearbox [31].

PMSG machines have become more attractive in recent years, because the performance of PM materials is improving and the associated cost is decreasing. PM machines can be classified

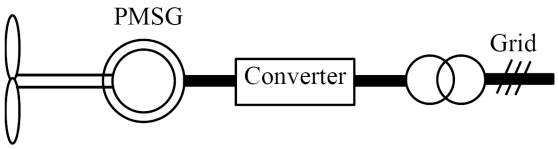

Figure 2.9: Scheme of a variable-speed direct-drive PMSG system [31]

into the radial flux and axial flux, based on the direction of the flux penetration. Transverse flux machines exist, but do not seem to have gained a foothold in wind power generation [33]. The radial flux machine is the most common type of the PM machine used in the industry. These machines higher torque capability and higher efficiency than conventional induction machines [34]. However, axial flux PM machines have become very popular in the recent years and are more and more incorporated into wind turbine concepts, since they can be designed to possess higher power densities than radial flux PM machines [15][33]. Moreover, they are ideal for modular machine designs and can accommodate a higher number of poles [15]. The latter advantage is very desirable for direct-drive machines due to their relatively large outer diameters. The high axial forces between the stator and rotor can be omitted by making use of a coreless stator structure. Air cored axial flux PM machine topologies are becoming popular and are commercially available in the sub-MW range [35][36].

2.3.2 Small-Scale WECS Concepts

In order to shift from a fossil fuel driven economy to a renewable energy dominated economy, investigation is needed, not only on the large-scale renewable systems, but also on the small-scale systems. Renewable energy sources, such as solar and wind, are suitable for small-scale electricity generation and have the potential to deliver affordable electricity to islands, mountainous, and desolate areas, which are isolated from the utility grid [37]. Electricity in remote locations is often generated by means of diesel generators, which use fossil fuel and pollute the environment.

Wind power has been used throughout history to grind corn and to pump water from underground wells. The so-called “western wheel” wind turbine is one of the most widely installed turbines and is typically used for water pumping and irrigation. A photograph of a classical “western wheel” turbine type is shown in Fig. 2.10. By the end of the 1930s, some 8 million units had been built and installed [25]. In recent years, small-scale wind energy systems have received renewed interest, and have become popular for small-scale electricity production. In low-cost stand-alone systems, the stator of the wind generator is usually connected directly to a battery by means of an uncontrolled rectifier [24]. Energy is transferred from the turbine to the batteries, once the rectifier output exceeds the battery voltage. An increase in speed will result in a higher current flowing to the batteries, thereby increasing the reaction torque

Figure 2.10: Classical "western wheel" wind turbine

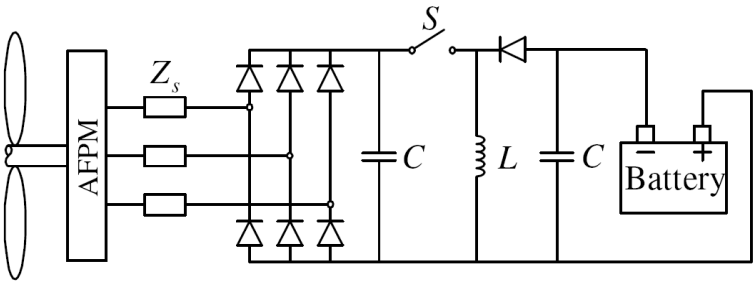

Figure 2.11: Schematic diagram of a wind energy system using a DC-DC converter connected between the rectifier and battery bank [24]

experienced by the generator, which tends to slow it down. Thus, the speed of the generator is kept relatively constant, and the terminal voltage of the generator is kept close to the battery bank voltage. When a threshold voltage at the battery banks is exceeded, it signifies that either too much current is flowing to the batteries or that they are fully charged, a dump load is connected in parallel with the load, which slows down the turbine. The dump load usually consists of a resistor bank or light bulbs.

The main disadvantage of direct battery charging is that maximum power from the turbine under variable wind speed conditions is not obtained. Power cannot be transferred to the batteries for wind speeds, where the rectified voltage is lower than that of the battery bank. In order to maximize the power captured by the turbine, a controller is required to regulate the battery voltage under varying wind speeds.

Many concepts are presented in literature to optimize the power captured from the turbine. The most common method makes use of a controlled unidirectional DC-DC converter. The

Figure 2.12: Sustainable wind energy system built from discarded materials [38]

converter is connected between the uncontrolled rectifier and the battery bank as shown in Fig. 2.11. The output voltage of the generator is therefore controlled actively, which results in maximum power to be extracted from the wind.

2.4 Sustainable Wind Energy Capture and Storage System

Sustainability can be summarized by the well known three R's: reduce, reuse and recycle. By reducing the world's energy consumption, by reusing materials from discarded components, and by recycling broken or unusable components, a sustainable society can be realized. The concept of a Green Economy is summarized succinctly by Gunter Pauli in his book: "The blue economy" [39]. He argues that many green products have become a luxury commodity, since they are more expensive than regular products. Effort therefore needs to be made to ensure the affordability of green products. This can be achieved by imitating the cascading principle of ecosystems, in which the output of one process becomes the input of another process [39]. Sustainability can therefore only be achieved when the entire system, i.e. energy source, materials used and the manufacturing process is done is a sustainable manner. Thus, great care needs to be taken when choosing the components and the materials of the system.

One of the most popular and inspiring sustainable wind energy systems was constructed by William Kamkwamba [38]. He used an old bicycle dynamo as a generator and designed and constructed his wind turbine system from blue gum trees, bicycle parts, and materials collected in a local scrap yard. Fig. 2.12 shows one of his sustainable wind turbines. Many

other sustainable home-built wind generator concepts have been constructed. Nearly all systems utilize a coreless axial flux PM machine topology. The PMs are usually taken from discarded HDDs and the generator is constructed by the do-it-yourself (DIY) principle. Most small-scale WECS use electrochemical batteries to store the energy in order to deal with the intermittent nature of the wind as a resource. However, this diminishes the sustainability of the system. Hence, an alternative system topology will be presented in this work.

This dissertation proposes a sustainable wind energy capture and storage solution for electrification of rural and impoverished areas prevalent in most developing countries. All system components are built from cheap, readily available and sustainable materials. Wind energy is captured by means of the sustainable PM generator and is stored in a sustainable flywheel, thereby guaranteeing continuous power delivery to the household. The dissertation furthermore addresses the challenges associated with the huge amount of e-waste that is produced and dumped daily, by proposing a sustainable machine topology, which reuses and recycles e-waste. Thus, the proposed system has a "double" green benefit, since it reuses e-waste to generate electricity from the abundantly available wind.

Chapter 3

Sizing of a Sustainable Wind Energy Capture and Storage System

This chapter presents the topology and sizing methodology for a sustainable wind energy capture and storage system. The individual components are described and alternative sustainable materials are discussed for the main components of the system.

3.1 Sustainable Topology

Renewable energy sources such as wind require energy storage, due to the intermittent nature of the natural resource. Conventional small-scale wind energy capture and storage systems use electrochemical lead-acid batteries mainly for energy storage. However, these are potentially toxic for human beings, detrimental to the environment, require high maintenance, have limited charge/discharge cycles and have low charge/discharge efficiencies. On the other hand, electromechanical batteries such as flywheels are environmentally friendly, require minimal maintenance, have high charge/discharge cycles capability and moderate charge/discharge efficiencies. A flywheel energy storage device can furthermore be built in a sustainable manner from reused and recycled components. The sustainable wind energy capture and storage system presented in this chapter has a wind generator coupled to a flywheel energy storage system device. The generated electricity is either consumed directly in a load or stored in the electromechanical flywheel energy storage device. As already mentioned, low-cost WECSs are typically used in electrochemical battery charging applications, which do not require a system controller. On the other hand, if a flywheel is used for energy storage, a system controller is required, which manages the overall power flow of the system [40][37]. Fig. 3.1 shows the overall system topology and power flow and a detailed block diagram of the proposed sustainable wind energy capture and storage system is shown in Fig. 3.2.

The alternating output voltage of the PMSG is first rectified via a full-bridge diode rectifier. A DC-DC converter then boosts the rectifier output voltage to a desired DC bus voltage, which supplies a DC load directly. Excess energy, which is not consumed by the load, is fed to the

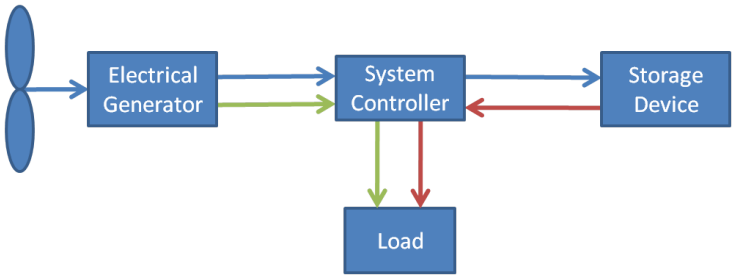

Figure 3.1: Overall system topology and power flow

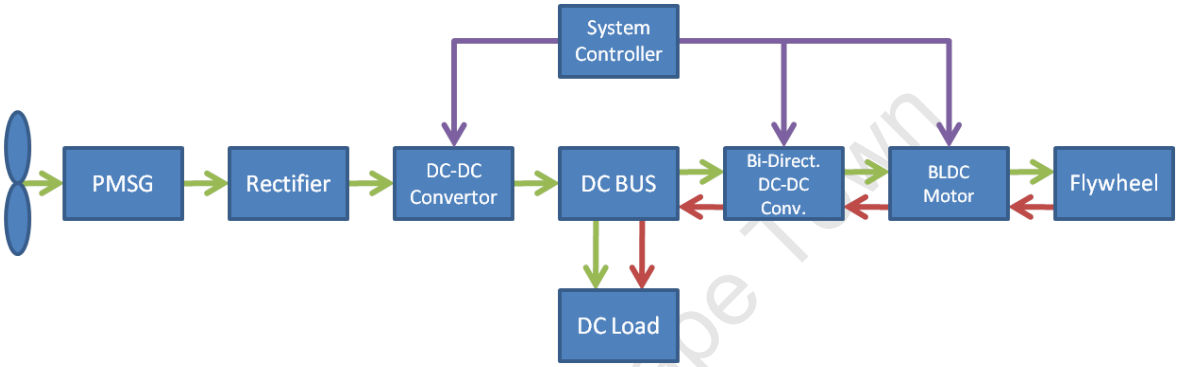

Figure 3.2: Detailed block diagram of sustainable wind energy capture and storage system

flywheel through the bi-directional DC-DC converter and a brushless DC (BLDC) machine that drives the flywheel. If an energy deficit occurs in the system, the flywheel supplies the load with the extra energy required. This ensures that maximum energy is being captured by the wind turbine and that the stored energy in the flywheel is made available for use by the load. In order for the flywheel to store and provide electrical energy, the BLDC machine can either operate as a motor (energy flowing from the wind generator to the flywheel) or as a generator (energy flowing from flywheel to load). A system controller controls the DC-DC converters, the BLDC machine and manages the power flow in the system.

3.2 Components and Materials of the Sustainable System

The individual components of the sustainable wind energy capture and storage system are described in this section. Sustainable materials for the components, which are sourced from redundant parts, are presented as well.

3.2.1 Wind Turbine

The wind turbine converts the kinetic energy in the wind into mechanical energy. The wind turbine considered for the sustainable system is a HAWT, and is chosen over a VAWT due to

(a) VAWT made from old 200 l drums [41] **(b)** HAWT made from PVC piping [42]

Figure 3.3: Home-built wind turbines

its higher efficiency and higher tip speed ratio, which leads to a higher rotational speed at the shaft. High rotational speeds are preferred since the efficiency of the generator increases with speed. A sustainable wind turbine can be built from the following sustainable materials: wood, discarded drums (plastic or steel) and PVC piping. A sustainable VAWT built from discarded 200l steel drums is shown in Fig. 3.3a and Fig. 3.3b shows a sustainable HAWT made from discarded PVC piping. For home-built systems, the turbine blades are mostly built from PVC piping, since they can relatively easily be cut and shaped into a blade profile and are easy to source. Hence, the envisaged turbine topology will be built from discarded PVC piping.

3.2.2 Generator and Motor

In essence only two components are needed to generate electricity, that is an electromagnetic field and an electrical conductor, which cuts through the field. PMs used in speakers and HDDs, produce an electromagnetic field and are suitable components for a sustainable wind generator. The magnets found in HDDs are made from high energy density rare-earth neodymium-iron-boron (NdFeB) magnets. Fig. 3.4 shows a schematic of an open HDD. These are preferred over ferromagnetic magnets found in speakers, since the latter have a peculiar shape and magnetization, and use ferrite magnets, which have a low energy density. The conductors for the machines can be sourced from the following discarded components: transformers of

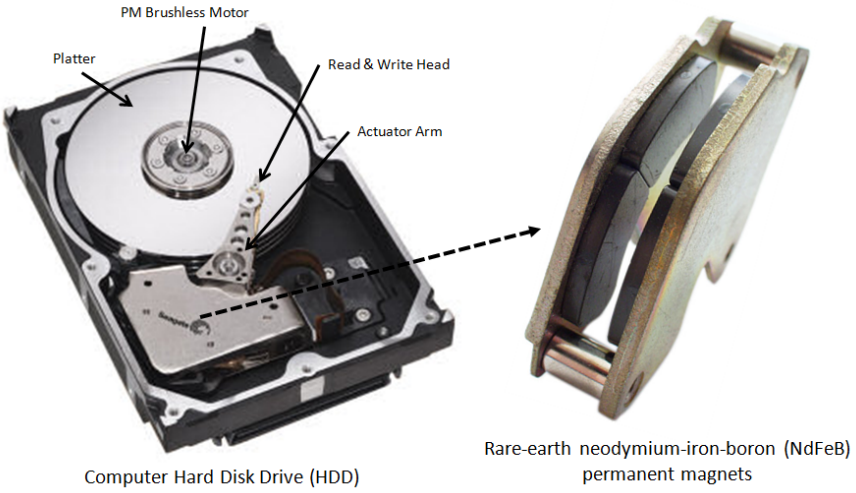

Figure 3.4: Computer HDD with PMs

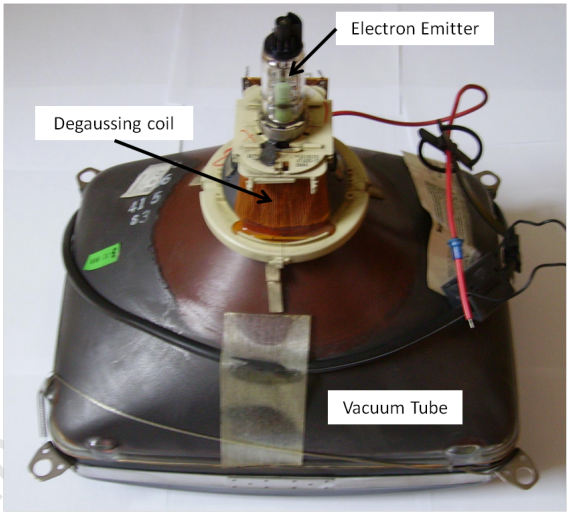

Figure 3.5: Degaussing coil in CRTs

old microwaves, coils from old motors and generators, as well as from degaussing coils of old cathode ray tubes (CRTs). It is however very difficult to unwind the wire of discarded components without damaging the insulation, since the coils are usually cured in epoxy resin. The degaussing coil of a CRT is seen in Fig. 3.5.

A sustainable machine topology using PMs from discarded HDDs and its detailed design process is presented in chapter 4.

3.2.3 Flywheel

A flywheel consists of a rotating mass, which stores energy in the form of kinetic energy (KE). The amount of energy stored in a flywheel is given by

$$KE = \frac{1}{2} J \omega^2 \tag{3.1}$$

where J is the mass moment of inertia and ω the angular velocity. It can be seen in equation (3.1) that the energy stored is proportional to its mass, but proportional to the square of its velocity. When using reused and recycled materials, it is unlikely and unsafe to achieve high speeds, i.e. beyond 1500 rpm. Thus, the mass of the flywheel needs to be maximized while keeping losses minimal. Good candidates for a sustainable flywheel include the following: flywheels sourced from vehicles, pressing cans into a flywheel shape or using sheet material to form a flywheel. All the aforementioned options require an extensive manufacturing process. The best option for a sustainable flywheel seems to be a vehicle tire filled with solid material, such as concrete [43]. A sustainable flywheel using the latter technique has been successfully prototyped under the co-supervision of the author of this dissertation and is recorded in [43]. The flywheel consists of a discarded car tire, which is filled with a special mixture of concrete to ensure mechanical integrity and is shown in Fig. 3.6a. The bearing and axle of an old car are levitating the wheel above the ground as shown in Fig. 3.6b. In order to ensure a safe working space, a safety case was constructed around it. Fig. 3.7 shows the assembled flywheel without the safety mesh.

3.2.4 DC-DC Converters and System Controller

In order to maximize the overall efficiency of the system, a DC-DC converter and a system controller is required. The proposed topology uses a DC-DC converter to boost the rectified voltage to the desired bus voltage and a bi-directional DC-DC converter manages the energy flow to and from the flywheel. There are four potential scenarios for the power flow: Firstly, from the generator to the load and to the flywheel, in cases when the PMSG generates excess energy. Secondly, from the generator to the load and from the flywheel to the load, in cases when the generator does not meet the power demand of the load. Thirdly, all the energy generated is consumed directly by the load. Finally, the power demand of the load is entirely met by the flywheel, in cases when the wind dies down completely. In [40], a similar system topology using a buck-boost and a bi-directional converter was implemented with a solar energy source and a flywheel energy storage device. It is recorded that the overall efficiency is greatly improved when using the aforementioned system topology. The DC-DC converter, system controller and bi-directional DC-DC converter can be built from readily available electronic components, as was done in [40] and [37].

(a) Discarded car tire filled with a special mix of concrete

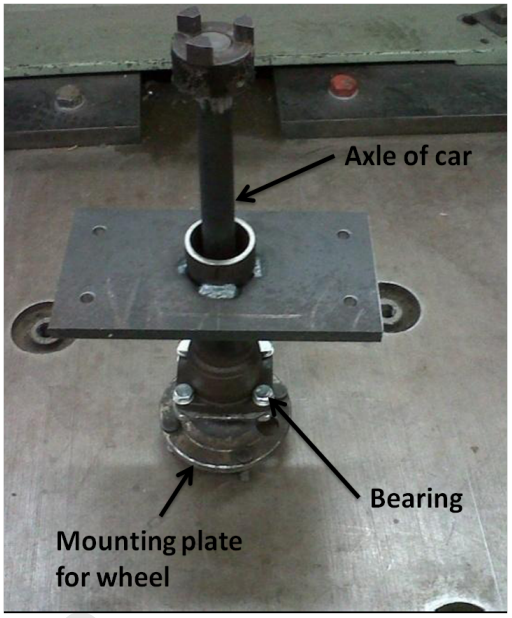

(b) Bearing/axle structure of old car

Figure 3.6: Parts of sustainable flywheel [43]

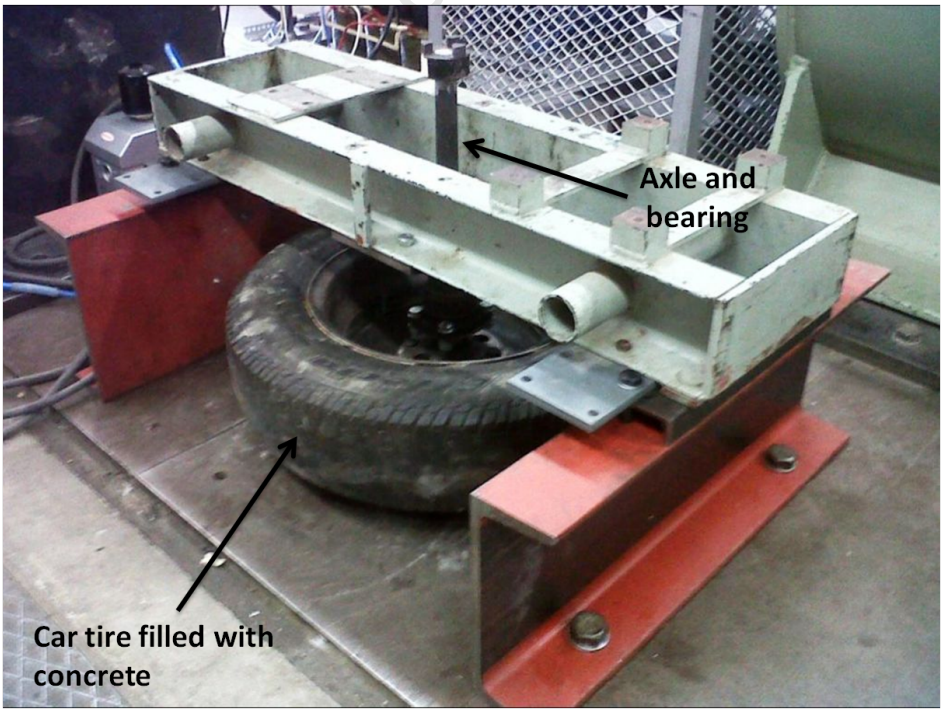

Figure 3.7: Assembled sustainable flywheel [43]

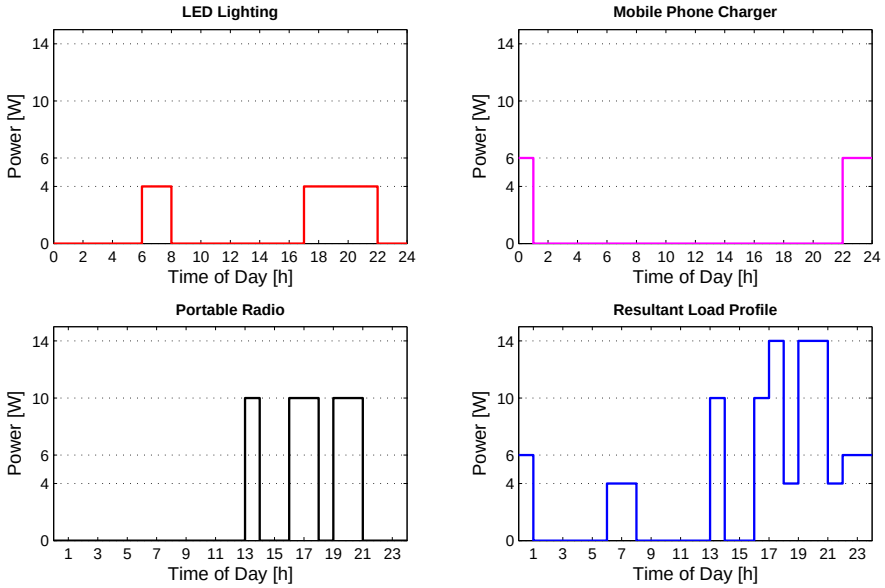

Figure 3.8: Developed load profile for a rural household

3.3 Sizing of the System Components

The sustainable wind energy capture and storage system topology, together with its components and materials were presented in the previous sections. The sizing procedure for the individual system components will be outlined in this section.

The rated wind speed (v), the tip speed ratio (λ), the aerodynamic efficiency of the turbine (C_p), the regulated DC bus voltage (V_{bus}), the efficiencies of the individual components, and the amount of energy stored in the flywheel (E_{fly}) are used as inputs to the sizing procedure.

3.3.1 Development of Electrical Load Profile

The sustainable wind energy capture and storage system will be assumed to supply a rural or impoverished urban household, which consists of four LED lights, a portable radio and two mobile phones. Assuming the electrical appliances are switched on as illustrated in Fig. 3.8, the total energy per day equates to 96 Wh with its peak and minimum power demands of 14 W and 4 W respectively [37][44]. The lights are assumed to be switched on for two hours during the morning hours (6-8 AM) and from sunset (5 PM) till 10 PM. The two mobile phones will be charged during the night time for three hours. The portable radio is assumed to be operated for one hour during lunch time, from 4-6 PM in the afternoon and from 7-9 PM in the evening, before the family goes to bed. The power rating of the appliances is shown amongst others in Table 3.1.

Table 3.1: Electrical appliances of household

Description of Load	Power Rating [W]	Number of Loads	Number of Hours Used	Energy Consumption [Wh]
LED light	1	4	7	28
Portable Radio	10	1	5	50
Mobile Phone Charger	3	2	3	18
Total	**14**	**7**	**15**	**96**

3.3.2 Flywheel Sizing

Ideally the flywheel should store at least one day's energy consumption, since the wind may not be available for up to one day. Nevertheless, it is nearly impossible for a sustainable flywheel to store energy for more than one day at reasonable costs. A sustainable flywheel using a discarded car tire filled with concrete was successfully prototyped in [43] and will furthermore be used in the sizing and design procedure presented here. The flywheel has a moment of inertia (J) of 3.33 $\mathrm{kg\,m^2}$ and its maximum speed was specified as 1500 rpm. Using eqn (3.1) the amount of energy stored in the prototyped flywheel was calculated to be 11.4 Wh. Assuming a depth of discharge of 90 % for the flywheel, the gross energy available from the flywheel is 10.3 Wh, when it is decelerated down to 474 rpm.

The dynamic equation for the mechanical system is given by [45]

$$T_{s,bldc} = B\,\omega_{fly} + J\,d\omega_{fly} \tag{3.2}$$

$$= T_{fly} + T_{\alpha} \tag{3.3}$$

where B is the equivalent viscous friction constant, ω_{fly} is the angular velocity of the flywheel, T_{fly} represents the rotational loss torque of the system, T_{α} is the torque needed to accelerate the flywheel and $T_{s,bldc}$ is the resultant shaft torque of the BLDC motor. In order to determine the period over which the flywheel can supply the load with power, its no-load run-down curve needs to be determined. The run-down curve is given by [45]

$$\omega_{fly}(t) = \omega_{fly0}\, e^{-t/\tau_m} \tag{3.4}$$

where ω_{fly0} is the initial angular velocity of the flywheel and $\tau_m = J/B$ is the mechanical time constant of the system. The time constant τ_m equals to 6.1 min in the case of the prototyped sustainable flywheel. Unfortunately this means that the flywheel has a high self discharge rate, which indicates that it is inefficient. However, it should be noted that no optimization was done since the first sustainable flywheel was prototyped. Assuming that an optimized flywheel results in an overall efficiency improvement and a τ_m of 30 min, the available energy in the flywheel under no-load condition can be calculated by using eqn (3.4). Constant power

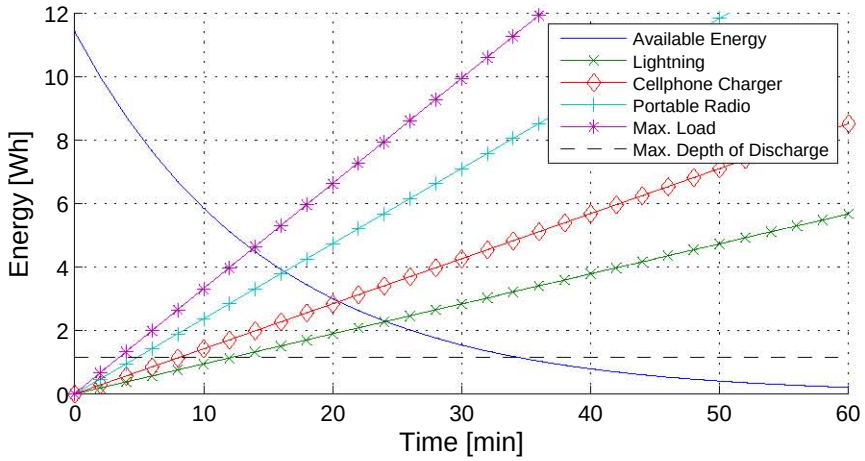

Figure 3.9: Available energy of the flywheel under no-load condition and linear energy consumptions of the different loading points

is drawn from the flywheel according to Fig. 3.8, which results in a linear energy consumption, since $E = \int P\,dt = P\,t$ for constant power. The energy consumption of the different loading points at the DC bus can be calculated by taking into account estimates of the efficiencies of the BLDC motor and bidirectional DC-DC converter of 75 % and 94 % respectively. The available energy of the flywheel under no-load conditions, together with the linear energy consumptions of the different loading points are shown in Fig. 3.9.

The self discharge losses of the flywheel can be calculated by multiplying the rotational loss torque (T_{fly}) with the angular velocity of the flywheel (ω_{fly}). Assuming that only the LED lights are switched on, the total power drawn from the flywheel is the sum of the flywheel losses and the constant power required by the LED lights as illustrated in Fig. 3.10. Integrating the total power with respect to time, gives the total energy drawn from the flywheel. The maximum period of time over which the flywheel can deliver power to the load is reached when the stored energy of 10.3 Wh is exceeded. The worst case scenario assumes that no power is captured by the wind turbine and that maximum power is demanded by the household. In this case, energy can be supplied to the load up to 12 min, the radio can be used for 14.1 min, the mobile phones charged for 17.3 min and the LED lights switched on for 19.9 min, provided they are used separately.

3.3.3 Wind Turbine Sizing

The flywheel was sized with respect to the developed load profile in the previous sub-section. This sub-section presents the sizing procedure for the wind turbine system.

With the viscous friction constant (B) and mechanical time constant (τ_m) known, the maximum torque of the flywheel ($T_{fly,max}$) can be computed to be 0.29 Nm. In order to keep the flywheel

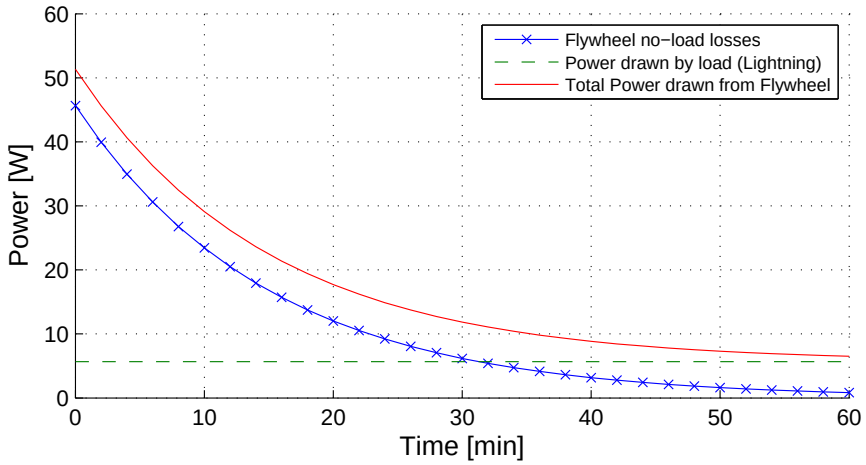

Figure 3.10: Total power drawn from the flywheel if the LEDs are switched on

spinning at 1500 rpm, 45.6 W is needed at the shaft of the BLDC. The maximum time for the flywheel to reach its rated speed is of great importance in the design procedure, in order to ensure that the flywheel is ready for discharge within the desired acceleration period. Allowing the flywheel to reach its maximum speed in one hour, the resultant shaft torque equates to 0.336 Nm, which requires a shaft power of 52.8 W. With the minimum power specified, the shaft power at the turbine can be determined by including estimates of the efficiencies of all components between the flywheel and the turbine. This can be expressed as

$$P_{s,turb} = \frac{P_{s,bldc}}{\eta_{gen}\,\eta_{rect}\,\eta_{dcdc}\,\eta_{bidir}\,\eta_{bldc}} \tag{3.5}$$

where $P_{s,turb}$ and $P_{s,bldc}$ are the shaft powers of the turbine and BLDC motor respectively, η_{gen}, η_{rect}, η_{dcdc}, η_{bidir}, η_{bldc} are the average efficiencies of the generator, rectifier, DC-DC converter, bidirectional DC-DC converter and BLDC motor respectively. The resultant shaft power of the generator determined in this manner is 110.5 W, if average efficiencies of 72 %, 98 %, 96 %, 94 % and 75 % are assumed for the generator, rectifier, DC-DC converter, bidirectional DC-DC converter and BLDC motor respectively.

The power captured by a wind turbine from the incident wind can be expressed as [28]

$$P_{s,turb} = \frac{1}{2}\rho_{air}\pi R^2 v^3 C_p \tag{3.6}$$

where ρ_{air} is the density of air at the height of the turbine, R the radius of the wind turbine. C_p is a function of the tip speed ratio (λ), at which the turbine is operating and can be expressed as [28]

$$\lambda = \frac{\omega_m R}{v} \tag{3.7}$$

where $\omega_m = 2\pi n/60$ is the mechanical angular velocity and n the rotational speed in rpm.

With the shaft power of the generator being determined and assuming that the turbine operates at cut-in wind speed of 4.35 m/s, λ is set to 7, and C_p to a low value of 0.3 (due to the fact that the turbine is proposed to be built from reused materials such as PVC piping), the radius of the turbine can be calculated to 1.54 m by solving eqn (3.6) for R. The rotational velocity of the turbine can then be computed by inserting R into eqn (3.7) and by multiplying with the result with $60/(2\pi)$, which equals to 188 rpm in this case.

Having determined the radius of the wind turbine and the power rating of the generator at cut-in wind speed, the generator can be designed and sized next.

3.3.4 Wind Generator Sizing

The generator needs to be designed for the maximum allowable wind speed, since this operating point produces maximum back-EMF and consequently maximum power. Inserting the maximum allowable wind speed of 8 m/s into eqn (3.7), the maximum shaft speed can be calculated to 347 rpm. The voltage rating of the generator is determined on the basis that the bus voltage (V_{bus}) is fixed at 72 V and the DC-DC boost converter operates at a duty cycle of zero for the maximum wind speed. Under these conditions, the phase voltage (V_{ph}) for a wye connected generator can be written as [46]

$$V_{ph} = \frac{V_{bus}\pi}{3\sqrt{6}} \tag{3.8}$$

The generator phase voltage calculated in this manner is 30.78 V. Furthermore, the maximum current is set to 3 A, as the maximum current density for a coreless generator should not exceed 8 A/mm^2 [28]. When using a conductor with a diameter of 0.7 mm, the current density is to 7.8 A/mm^2. The maximum power that can be extracted from the generator under the above conditions equals to 277 W. This results in an acceleration time of the flywheel from 0 - 1500 rpm in just less than 9 minutes.

A third operating scenario will be considered for the sustainable wind energy capture and storage system. When the wind speed drops below the designed cut-in wind speed of 4.35 m/s, the turbine cannot capture enough power to keep the flywheel running at 1500 rpm. However, it might still capture enough power to supply the household according to Fig. 3.8. Assuming the same efficiencies of the components and using the maximum power of 14 W required at the bus, the minimum generator power calculated in this manner is 15.2 W. An absolute minimum wind speed of 2.5 m/s is determined by inserting 15.2 W into eqn (3.6) and solving for v.

Considering all limitations, constraints and operation points discussed so far, the wind generator and BLDC motor can be sized accordingly.

3.3.5 DC-DC Converter Sizing

The bus voltage needs to be regulated and is achieved by means of the boost converter before the bus. It has been mentioned that at the maximum allowable wind speed the duty cycle is set to zero. When the wind speed drops, the converter boosts the rectified voltage to 72 V, thereby regulating the bus voltage. The maximum boosting occurs when the turbine operates at lowest wind speed of 2.5 m/s. In this case the duty cycle is 0.57. The maximum current passing through the converter can be determined by dividing the maximum bus power of 260.64 W by the regulated bus voltage, which then equates to be 3.62 A. The bidirectional DC-DC converter is rated for the same current as the boost converter. Depending on the design of the BLDC motor, the duty cycles for the different operation points of the flywheel can be determined next.

3.4 Conclusion

A summary of the sizing results are given in Table 3.2. A topology for a sustainable wind energy capture and storage system was formulated and a methodical sizing approach of the individual components was presented. Sustainable topologies for the individual components, together with alternative sustainable materials for these topologies, were outlined. The system was designed around an existing sustainable flywheel and the rest of the system components could then be sized accordingly. It can be concluded that materials sourced from e-waste are available and can be used for the envisaged sustainable topology. By reusing and recycling e-waste, 11.4 Wh of electrical energy can be stored in a sustainable flywheel. At the rated wind speed of 8 m/s, the sustainable generator produced 277 W of electrical power. The turbine was designed to capture the wind power from a wide range of wind speeds, i.e. from 2.5 - 8 m/s. This guarantees maximum supply of power to the DC load. Furthermore, the low-power load profile developed in this chapter was linked to three operation points of the

Table 3.2: Summary of results

Wind Speed [m/s]	**8**	**4.35**	**2.5**	**< 2.5**
Turbine radius [m]				1.54
Shaft speed of generator [rpm]	347	188	108	-
Phase voltage of generator [V]	30.78	17.67	13.36	-
Output power of generator [W]	277	79.57	15.16	-
Rectifier voltage [V]	72	41.33	31.25	-
Time needed to accelerate the flywheel from 0 to 1500 rpm [min]	8.71	60	-	-
Period over which the flywheel can deliver 14 W to the household [min]		-	12	12

system, thereby the operation limits of the wind energy system could be calculated. In case the wind dies down completely, the flywheel can supply 14 W to the household for up to 12 min, before the wind needs to pick up again. With the wind blowing at very low speeds (> 2.5 m/s), the system is capable of supplying the household continuously with power.

Chapter 4

Detailed Design of a Sustainable Wind Generator

The chapter reviews the most common machine topology for a sustainable wind generator built from redundant materials, and a suitable topology is presented and discussed in detail. The most important winding configurations, together with their advantages and disadvantages are reviewed, from which a concentrated overlapping full-pitch wave winding configuration is developed. The performance of the machine is predicted using classical machine theory. A new sizing approach for the sustainable machine is derived, which uses the PM length in the radial direction as the sizing parameter. Finally, the sustainable generator is sized according to the requirements specified in the previous chapter and its dimensions are calculated.

4.1 Sustainable Wind Generator Topologies

The construction of the most common DIY machine topology built from HDD magnets is discussed together with its advantages and disadvantages. A machine topology will be presented thereafter, which is based on the work done in [12][13].

4.1.1 DIY - Wind Generator Topology

Sustainable generators have been successfully built with the DIY principle by many hobbyist and several have been published on the internet [10][11]. Fully functional wind generator kits, which are based on the DIY principle, are commercially available, e.g. from Hugh Piggott [47]. However, these generators are all designed and built intuitively without a methodical design approach.

Some of these generators use NdFeB PMs from HDDs, whilst others use custom made PMs for flux production and utilize coreless stators fitted with tooth-concentrated non-overlapping windings. A typical sustainable machine utilizing a rotor structure with PMs from HDDs and concentrated non-overlapping windings is shown in Fig. 4.1. In this machine, the PMs

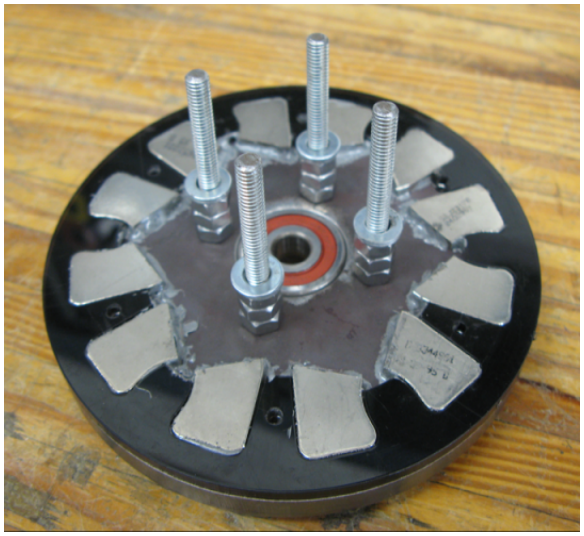

(a) Rotor using cut PMs from HDD

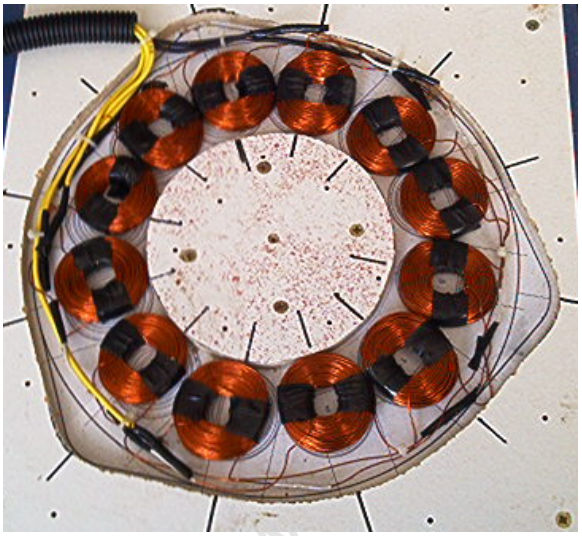

(b) Coreless stator fitted with double-layer tooth-concentrated non-overlapping windings

Figure 4.1: Typical DIY generator [12]

are removed from their backing plates, cut and fixed to steel rotor discs as shown in Fig. 4.1a. The stator is generally formed using double-layer tooth-concentrated non-overlapping windings as shown in Fig. 4.1b.

The HDD magnets have a peculiar shape and magnetization, which results in some challenges with the machine design. The N-pole is adjacent to the S-pole and both poles are secured to a ferromagnetic backing plate as shown in part 1 of Fig. 4.2a. Therefore, to be able to use conventional winding configurations, the poles are generally removed from the backing plate and separated as shown in part 2 and 3 of Fig. 4.2a. The cut magnets have a uniformly distributed airgap flux-density, whereas uncut magnets on their existing backing plates have a non-uniform flux-density distribution as shown in Fig. 4.3. It is practically impossible to create an array of uncut HDD magnets with backing plates, since the poles do not cover the entire backing plate. The effect of the "imaginary or missing poles", which are shown in Fig. 4.2b, on the airgap flux-density distribution can clearly be seen in Fig. 4.3.

The sustainable wind generator topologies which use cut HDD PMs have two main setbacks. Firstly, NdFeB magnets are extremely brittle and separating the two poles from each other is very cumbersome and often deteriorates the PMs. Secondly, the backing plates of the PMs are discarded, which requires the use of a ferromagnetic rotor, which increases the cost and diminishes its sustainability. Thus, a topology which uses uncut PMs with their backing plates is proposed and discussed in the following sub-section.

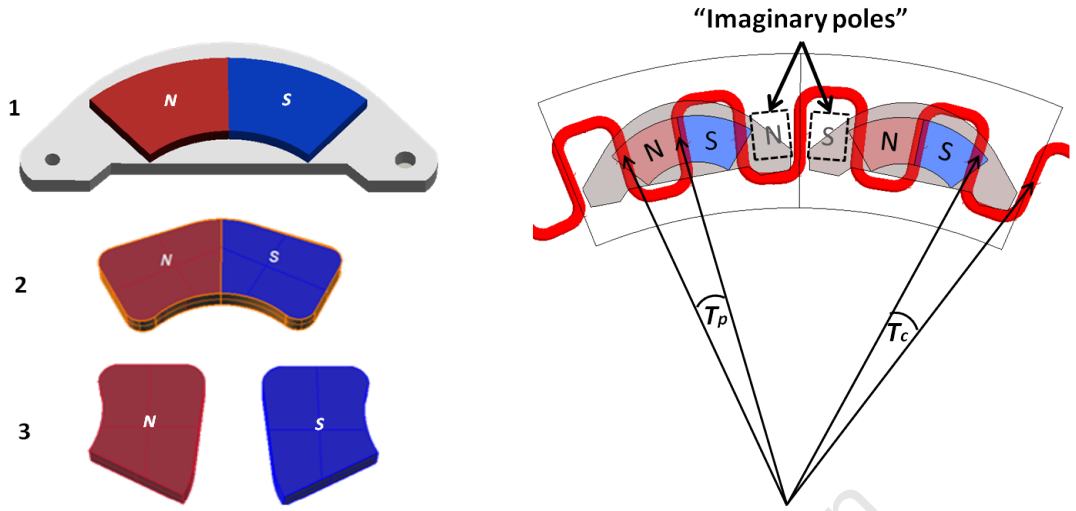

(a) Typical geometry of a HDD magnet

(b) Wave winding with 2 HDD magnets and "imaginary poles"

Figure 4.2: HDD magnets and wave winding

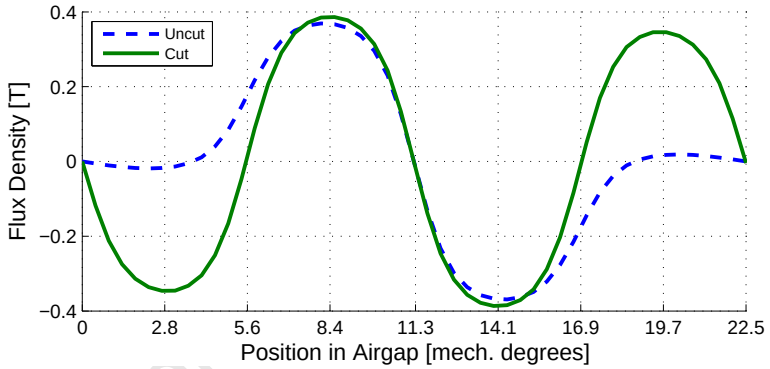

Figure 4.3: Flux-Density distribution for cut and uncut magnets

4.1.2 Proposed Generator Topology

The proposed generator topology is an axial flux PMSG, which uses uncut HDD magnets on their existing backing plates. The magnets are distributed uniformly around the periphery of the rotor disc, whilst ensuring that the distance between each magnet is exactly two pole pitches as illustrated in Fig. 4.2b. The absent poles can be described as "imaginary poles" (see Fig. 4.2b), since they indeed do act as poles by increasing the electrical frequency of the generator as expressed in eqn (4.19). However, they do not contribute to the performance of the machine, since their flux-density is nearly zero. Therefore, they do not contribute to the EMF in the machine according to eqn (4.21).

The non-uniform flux-density distribution results in unsymmetrical back-EMF production if conventional 3-phase non-overlapping winding configurations are used. Fig. 4.4 shows

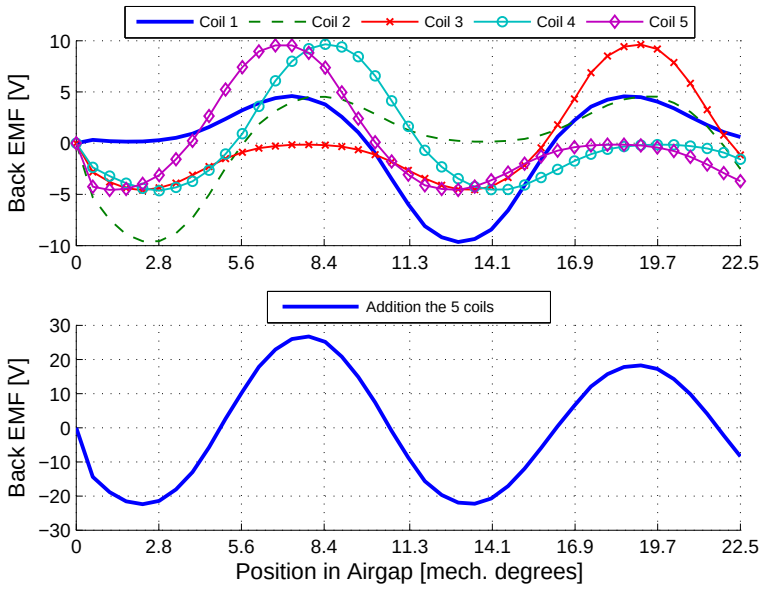

Figure 4.4: Back-EMF production of a double layer tooth-concentrated non-overlapping winding configuration with 5 coils per phase group ($p = 64$, $Q_s = 60$)

the back-EMF production per phase for a double layer tooth-concentrated non-overlapping winding configuration for a machine with 64 poles and 60 slots. For this specific winding configuration, five coils per phase are situated next to each other before the next phase group starts (phase grouped winding with $u = 5$ according to eqn (4.2)). The top graph in Fig. 4.4 shows the EMF induced in each of the five coils, when it is exposed to the non-uniform airgap flux-density distribution. Each of the five coils produces a back-EMF waveform which is similar to that of the non-uniform airgap flux-density waveform. Since the coil pitch of the tooth-concentrated non-overlapping winding configuration is not equal to a pole pitch of the machine, the resultant phase voltage is unsymmetrical, i.e. the peak value of the phase voltage is varying as shown in the bottom graph in Fig. 4.4. This calls for a suitable winding configuration that will produce a symmetrical voltage waveform. Hence, a concentrated full-pitch overlapping winding is adapted to resemble a conventional wave winding of brushed DC machines. This "wave winding" behaves the same as a concentrated full-pitch overlapping winding, but only differs in the way the phase coils are wound. This winding configuration produces a symmetrical sinusoidal back-EMF waveform regardless of the non-uniform flux-density distribution, provided that the coil pitch is equal to the pole pitch. A portion of the described wave winding is shown in Fig. 4.2b. The wave winding spans over one complete pole pitch and runs along the entire circumference of the rotor and has N_c turns per coil.

Fig. 4.5 attempts to explain the EMF production of the wave winding. Each coil side experiences a non-uniform flux-density distribution as the uncut PMs move over it (e.g. Side 1 in Fig. 4.5a). The second coil side (Side 2) is displaced by one pole pitch and is inverted,

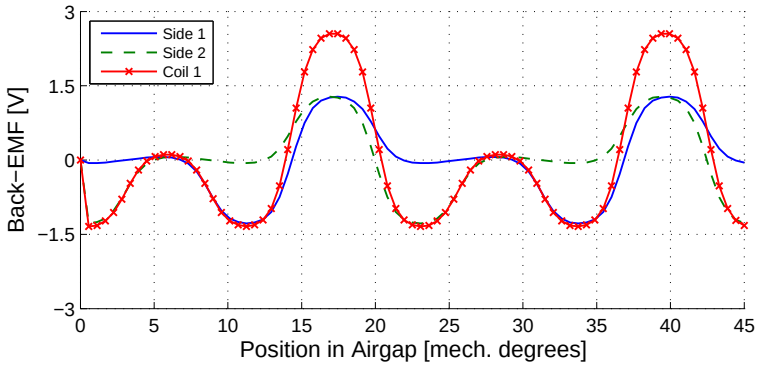

(a) Back-EMF induced in a single coil when exposed to the non-uniform airgap flux-density distribution

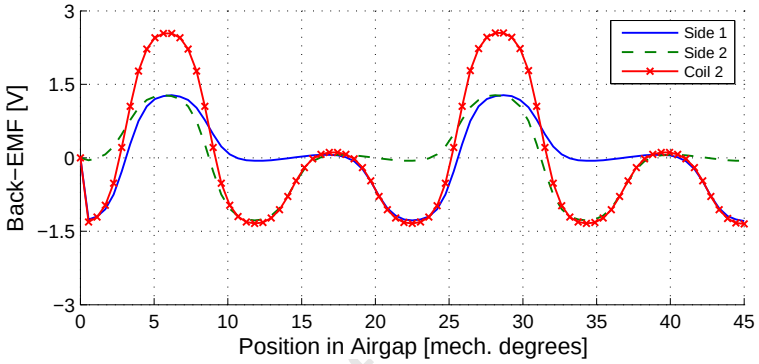

(b) Back-EMF induced in a second coil, which is displaced by two pole pitches

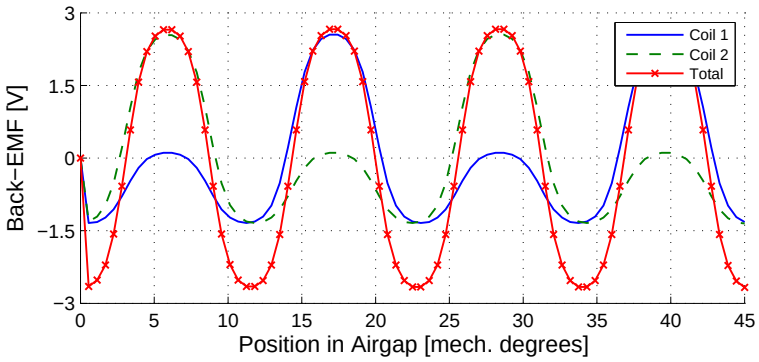

(c) Resultant back-EMF when both coils are summed up (Coil 1 + Coil 2)

Figure 4.5: Back-EMF production of the concentrated full-pitch overlapping winding configuration

since it resembles the return path of the coil. The resultant EMF experienced by a single coil is the sum of both coil sides (Coil 1 in Fig. 4.5a). Two coils (or any even number of coils) connected in series produce a symmetrical sinusoidal waveform as shown in Fig. 4.5c. The back-EMF is proportional to the number of coils connected in series. The advantage of the wave winding over a concentrated full-pitch overlapping winding is the reduction of the coil inter-connecting leads, since it consists of only one "coil" with two end-leads. Its main and

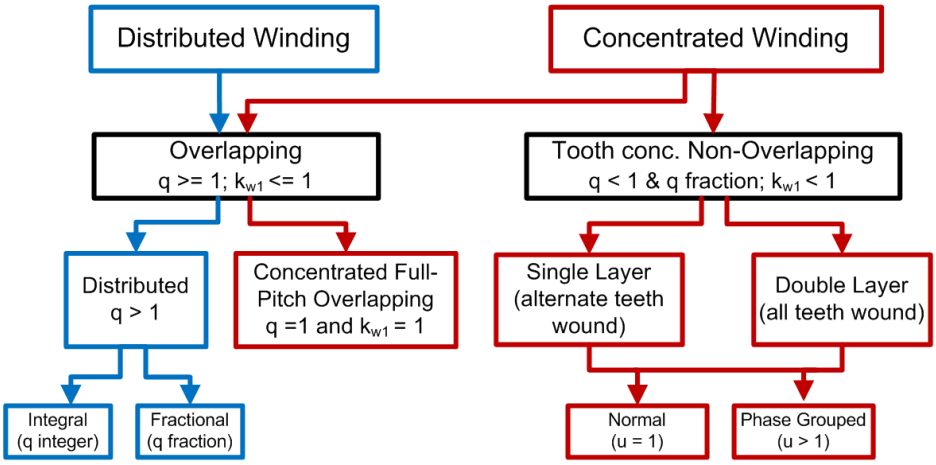

Figure 4.6: Overview of winding configurations of electrical machines; q from eqn (4.1); u from eqn (4.2); k_{w1} is the fundamental winding factor

most important advantage over tooth-concentrated non-overlapping windings is the fact that it produces symmetrical sinusoidal voltage waveforms and a balanced 3-phase system despite the non-uniform airgap flux-density distribution.

4.2 Winding Configurations

The interpretation of winding configurations in literature varies, and is sometimes confusing. Literature is furthermore not consistent in naming and classifying different winding configurations. However, the underlying principle of the winding configurations is the same throughout literature [45][48][49][50]. The following paragraphs attempt to summarize the most common winding configurations. Fig. 4.6 shows an overview of different winding configurations.

The number of slots per pole per phase, q is commonly used for classification of winding configurations and is given by:

$$q = \frac{Q_s}{p m_1} \tag{4.1}$$

where Q_s is the total number of total slots, p is the number of poles and m_1 is the number of phases.

Winding configurations are generally referred to as concentrated or distributed depending on the span and grouping of coils which form the winding. For distributed windings, as found in classical synchronous and induction motors, q is greater than unity [45], meaning that the machine has a large number of slots per pole per phase. This ensures that for a small number of poles (normally 2,4,6), the stator and rotor structure is utilized better. They can further be

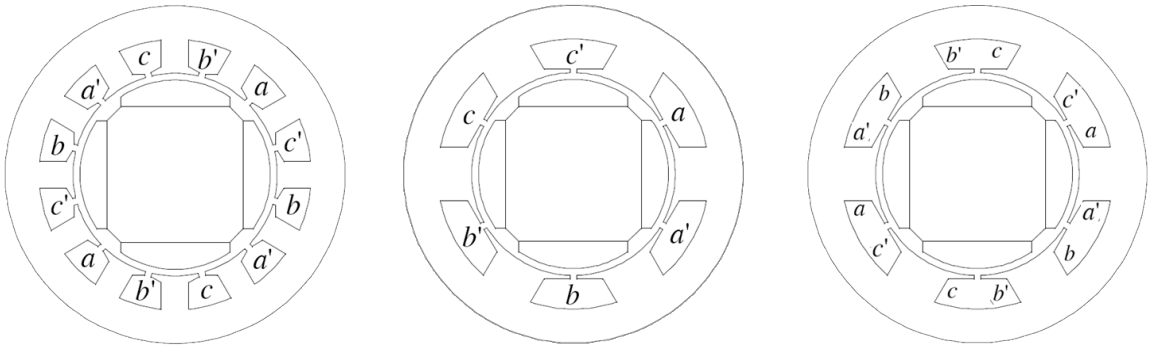

(a) Concentrated full-pitch overlapping winding

(b) Tooth-concentrated single-layer winding

(c) Tooth-concentrated double-layer winding

Figure 4.7: Winding configurations of radial flux iron-cored machines, adapted [24]

divided into integral (q an integer) and fractional (q a fraction) windings [50]. By distributing the phase coils in several slots, compared to concentrating all coils in two slots, the back-EMF production of the machine becomes more sinusoidal, but results in a winding factor of less than unity. For distributed windings, the phase coils need to overlap in order to ensure an appropriate winding configurations.

Another overlapping winding configuration is the concentrated full-pitch overlapping winding, which has q equal to unity. This ensures that the coil pitch (τ_c) is equal to the pole pitch (τ_p), which results in a winding factor of 1. Since the coil and pole pitches are equal, the phase coils need to overlap. Nevertheless, these windings are concentrated and not distributed, since all coils are concentrated in two slots. The concentrated full-pitch overlapping winding for an iron-cored machine and a coreless axial flux machine are shown in Fig. 4.7a and Fig. 4.8a. The overlapping phenomenon is clearly noticeable as the return path of a phase coil is not located in an adjacent slot to the go-path.

In tooth-concentrated windings, no need exists for the phase coils to overlap, since both coil sides of a coil are placed in two adjacent slots and the coil is concentrated around a single tooth as shown in Figs. 4.7b and c. This results in the coil pitch being shorter than the pole pitch, hence the term short-pitching. The short-pitching of the coils lead to a phase shift in the back-EMF production in the series connected coils of a phase, which results in a winding factor less than unity. 4.8b shows a coreless tooth-concentrated non-overlapping winding and the short-pitching of the coils is noticeable. The tooth-concentrated non-overlapping windings are furthermore separated into single layer and double layer windings. In single layer or alternate teeth wound configurations the slot is only occupied by one coil side, whereas in double layer or all teeth wound windings two coil sides share one slot as shown in Figs. 4.7b and c respectively. They can further be divided into "normal" non-overlapping windings and phase-grouped windings. The only difference between them is the number of coils per phase group (u) and is given by eqn (4.2) [48].

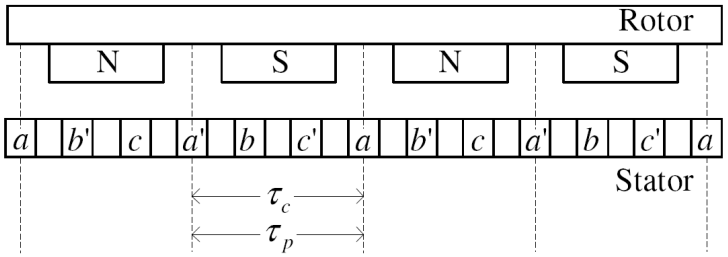

(a) Concentrated full-pitch overlapping winding

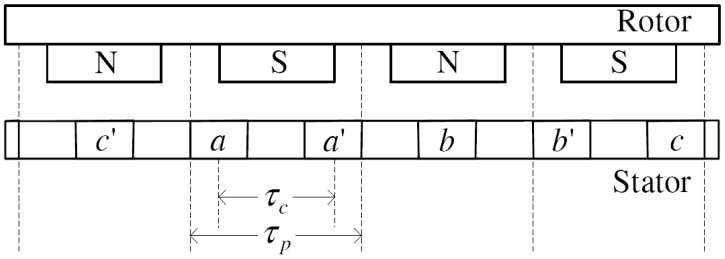

(b) Tooth-concentrated non-overlapping winding

Figure 4.8: Winding configuration for coreless axial flux machines [24]

$$u = \frac{Q_s}{m_1} W_s \tag{4.2}$$

where W_s is the number of winding sections and is given as [48]:

$$W_s = \gcd(p, Q_s) \tag{4.3}$$

where gcd is the greatest common divisor. When u is 5 for example, five coils of phase A lie next to each other, before the next phase group starts as illustrated in Fig. 4.9.

The major advantage of tooth-concentrated windings over classical distributed windings is the shorter end-windings, since the phase coils in distributed windings spans several slots and need to overlap in order to realize a valid winding configuration. Distributed windings have the highest copper losses followed by tooth-concentrated single layer windings, with tooth-concentrated double layer windings having the least [51][52].

The following sub-sections discuss three winding configurations, namely the tooth-concentrated non-overlapping windings, the concentrated full-pitch overlapping winding and the concentrated full-pitch overlapping wave winding.

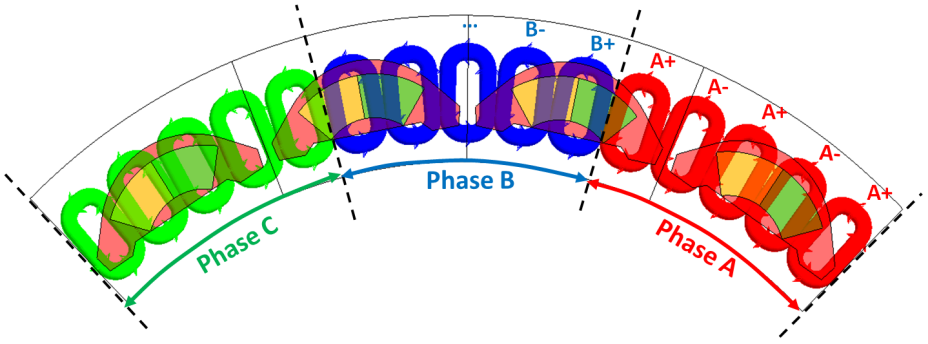

Figure 4.9: Tooth-concentrated phase-grouped double layer winding configuration with five coils per phase group ($u = 5$)

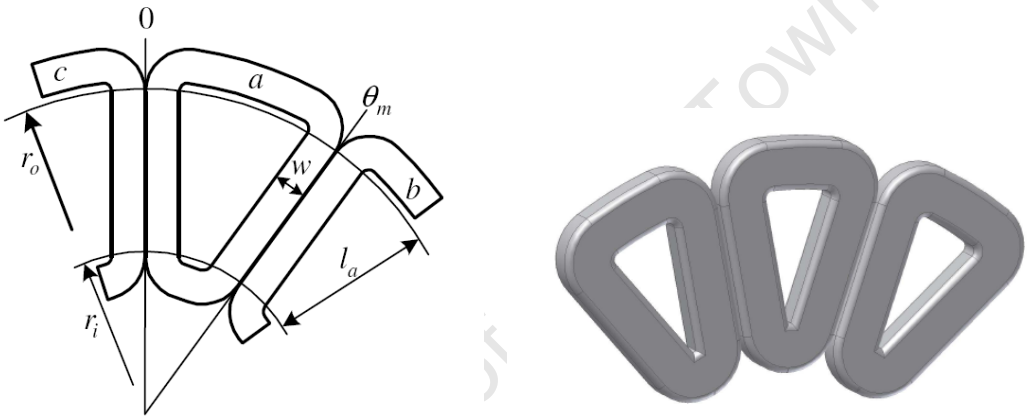

(a) Schematic view **(b)** 3D drawing

Figure 4.10: Coreless tooth-concentrated non-overlapping winding configuration [24]

4.2.1 Tooth-concentrated Non-Overlapping Winding Configurations

In tooth-concentrated non-overlapping winding configurations the individual coils lie adjacent to each other as illustrated in Fig. 4.10. As already discussed, this topology does not require any bending of the end-windings, consequently reducing the total volume of copper used. Also, their winding factors are less than unity (usually between 0.84 - 0.95 [50]), due to the short-pitching of the coils. Nevertheless, a lot has been done to improve the winding factor and to optimize non-overlapping windings [48][49][50].

The coils of coreless non-overlapping windings are usually pre-formed by means of a bobbin form. The coils are then grouped and inter-connected by means of leads to form the phase winding. This can be very cumbersome for machines with many poles. This is especially true when the number of poles is high for a relatively small circumference of the rotor. For an axial flux PM machine with average radius of 0.1955 m and 64 poles for example, the pole pitch equates to 19.19 mm or 5.625 mechanical degrees. When using a double layer non-overlapping winding configuration with $q = 5/16$, the coil pitch of a coil is 4.25 mechanical degrees, which

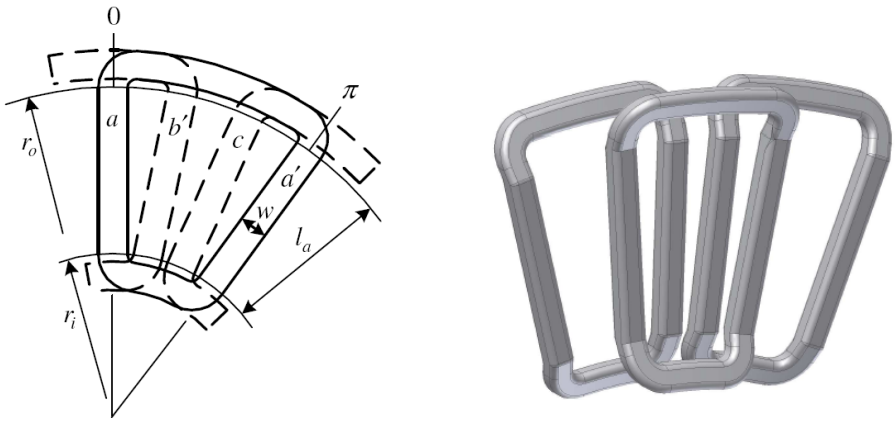

(a) Schematic view **(b)** 3D drawing

Figure 4.11: Coreless concentrated full-pitch overlapping winding configuration [24]

is equal to 7.25 mm for the coil radius. Practically, it is extremely difficult to wind and inter-connect the individual coils to each other. In addition, as discussed in section 4.1, this type of winding configuration is not applicable to the uncut HDD magnets, since it does not produce a symmetrical back-EMF. Hence, other winding configurations need to be explored.

4.2.2 Concentrated Full-Pitch Overlapping Winding Configuration

In concentrated full-pitch overlapping winding configurations, the individual coils also lie next to each other in the same plane as shown in Fig. 4.11. Since the coil pitch is equal to that of a pole pitch, the end-windings of the coils need to overlap each other in order to ensure correct sequence and polarity. The end-winding structure is physically obtained by bending the end-windings to ensure the least end-winding length and least mechanical clearance between the rotor and stator structure as shown in Fig. 4.11b. These have one slot per pole per phase ($q = 1$), which results in an ideal winding factor of 1 [24].

Unlike non-overlapping windings, concentrated full-pitch overlapping windings are able to produce a balanced 3-phase system from a non-uniform airgap flux-density distribution given that the coil pitch is equal to that of a pole pitch. Nevertheless, the set-backs associated with the large proportion of coil inter-connecting leads and the small radii of the bobbin-wound coils for concentrated overlapping windings still remain, since the coils are wound in the same way as the concentrated non-overlapping windings.

This calls for a suitable winding configuration that minimizes the end-connections, ensures a simpler way for winding the phase coils and guarantees a balanced 3-phase output. The concentrated full-pitch overlapping wave winding overcomes the aforementioned challenges and is described in the next sub-section.

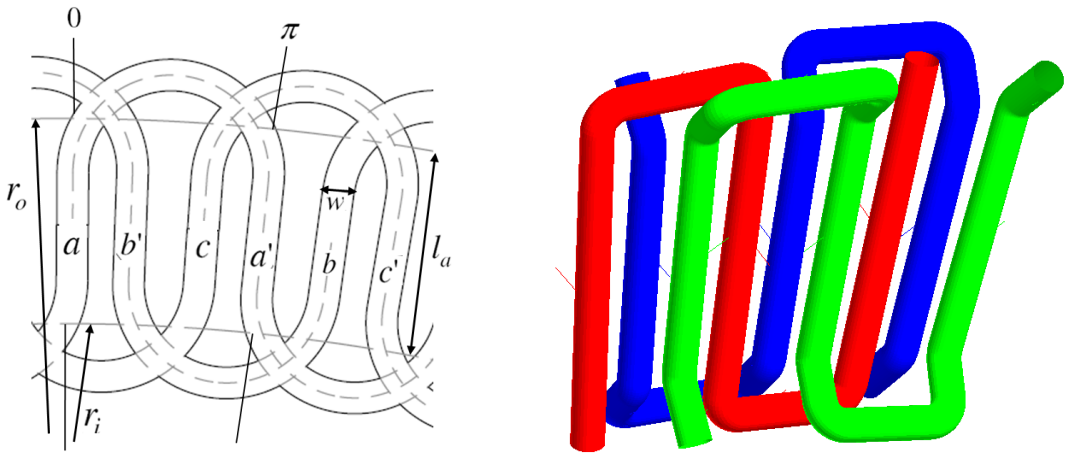

(a) Schematic view **(b)** 3D drawing

Figure 4.12: Coreless concentrated full-pitch overlapping wave winding configuration

4.2.3 Concentrated Full-Pitch Overlapping Wave Winding Configuration

As already mentioned the wave winding is similar to the concentrated full-pitch overlapping winding and is shown in Fig. 4.12. The only difference to a concentrated full-pitch overlapping winding is the end-windings. Instead of using bobbin-wound coils, the wave winding makes use of a continuous "coil", which is similar to a wave winding of conventional brushed DC machines and resembles a wave; thus its name: wave winding. The coils are not wound in a loop as is the case with conventional windings, but rather wound from one slot to another, always skipping two slots as shown in Fig. 4.12a. The coils lie in the same plane, and the end winding structure is the same as of the concentrated full-pitch overlapping winding as illustrated in Fig. 4.12b. Since the wave winding consists of only one continuous coil, the entire phase coil can be wound at once with a single mold, thereby introducing a simple winding technique. The mold for winding the phase coils is shown in Fig. 6.9a.

The wave winding overcomes the challenges encountered with the other winding configurations, by reducing the coil inter-connecting leads and by producing a symmetrical waveform and a balanced 3-phase output system, despite the non-uniform flux-density distribution.

4.3 Analytical Design and Theoretical Performance Analysis of the Sustainable Generator

This section presents the analytical design and theoretical performance analysis of the sustainable axial flux PMSG. The conventional sizing approach uses the ratio of *inner-to-outer PM radius* as the sizing parameter, which cannot be used for the proposed machine topology since the ratio is fixed for a specific radius based on the dimensions of the HDD PMs. Hence, a new sizing approach for the sustainable machine is derived, which uses the PM length in the radial direction as the sizing parameter.

4.3.1 Magnetic Flux

Since the dimensions of axial flux PM machines are dependent on the radius, the electromagnetic torque is produced over a continuum of radii unlike in cylindrical machines, where the torque is produced at a fixed airgap radius. For this reason, the machine performance parameters will be shown to be dependent on the inner radius (r_i) and outer radius (r_o) of the machine [15].

Approximate Calculation of Airgap Flux-Density

The peak/plateau value of the magnetic flux-density (B_{mg}) produced at the center of the effective airgap (g) by a PM with a linear demagnetization curve and height (h_M), placed in a magnetic circuit with infinite permeability can be approximated as [16] [52]:

$$B_{mg} = \frac{B_r}{\frac{1}{C_\phi f_{LKG}} + \frac{\mu_r g}{h_M}} \tag{4.4}$$

where B_r is the remanent flux-density, μ_r the relative permeability of the PM. C_ϕ is the flux focusing/concentration factor and can be expressed as the ratio of airgap area (A_g) to the area of the magnets (A_M), whereas f_{LKG} is the leakage coefficient, which is the ratio of airgap flux (ϕ_g) to the magnet flux (ϕ_M) as shown in eqn (4.5) and eqn (4.6) respectively [16].

$$C_\phi = \frac{A_g}{A_M} \tag{4.5}$$

$$f_{LKG} = \frac{\phi_g}{\phi_M} \tag{4.6}$$

The effective length of the airgap (g) is measured between the opposite magnets on the rotors and is given by:

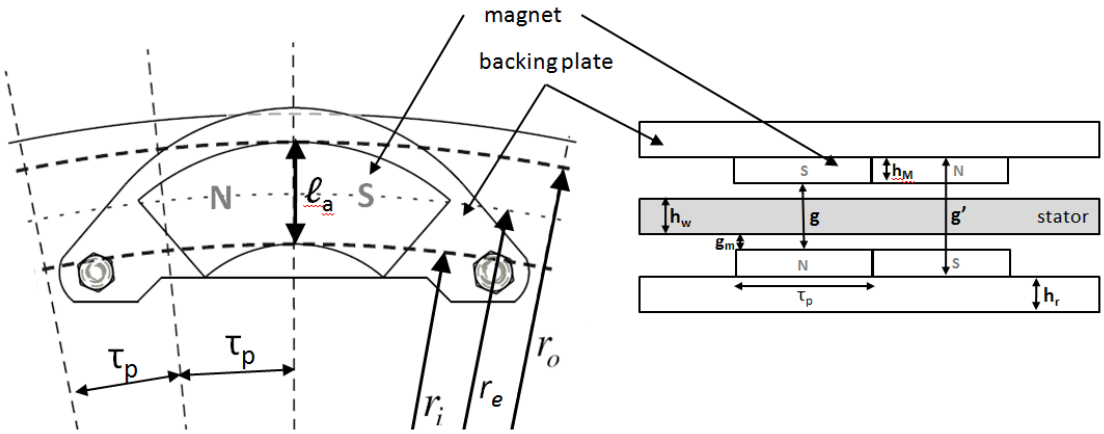

Figure 4.13: Dimensions of the sustainable axial flux PM machine topology

$$g = 2g_m + h_{\mathrm{w}} \tag{4.7}$$

where h_{w} is the depth of the stator in the axial direction and g_m is the mechanical clearance between the PM and the stator surface as shown in Fig. 4.13. For coreless machines, g is crucial because of the absence of a ferromagnetic stator and needs to be maintained as small as possible to ensure a reasonable airgap flux-density distribution.

Flux per Pole

The average value of a sinusoidal flux-density distribution is given by $B_{avg} = 2/\pi\, B_{mg}$, where B_{mg} is the peak value of the flux-density distribution. For a non-sinusoidal distribution $B_{avg} = \alpha_i B_{mg}$ holds, where α_i is the ratio of the average to peak value of the magnetic flux-density at the center of the airgap, i.e. [15]:

$$\alpha_i = \frac{B_{avg}}{B_{mg}} \tag{4.8}$$

$$= \frac{b_p(r)}{\tau_p(r)} \tag{4.9}$$

where the pole pitch ($\tau_p(r)$) and the magnet/pole arc ($b_p(r)$) are both functions of the radius. Hence, α_i is normally independent of the radius [15].

Since the incremental surface area per pole is $2\pi r/p\, dr$, the magnetic flux per pole (ϕ_p) can be expressed as [15]:

$$\phi_p = \int_{r_i}^{r_o} B_{avg} \frac{2\pi}{p} r dr \tag{4.10}$$

$$= B_{avg} \frac{\pi}{p} (r_o^2 - r_i^2) \tag{4.11}$$

For conventional machines, it is convenient to define and use the ratio of *inner-to-outer PM radius*, i.e. $k_d = r_i/r_o$, since the magnet shape can be manufactured according to the design specifications. Hence, the expression for the flux per pole takes the following form [15]:

$$\phi_p = \frac{B_{avg} \pi r_o^2}{p} (1 - k_d^2) \tag{4.12}$$

The factor k_d is optimum at either 0.57 or 0.63 for high torque to weight ratio or maximum power [53][54], 0.68 for maximum efficiency and about 0.7 for minimum magnet volume [17][52]. When using magnets with a fixed shape, as is the case with PMs from HDDs, k_d can no longer be set to an optimal value or used in the design procedure. The reason for this is that the PM length in the radial direction (l_a) is constant for magnets with a fixed shape and consequently k_d will vary with the radius at which the HDD PMs are placed. The length of the PMs in the radial direction (l_a) is calculated as the difference between the outer and inner radii of the magnet as:

$$l_a = r_o - r_i \tag{4.13}$$

The inner radius in eqn (4.11) is substituted with $r_i = r_o - l_a$ and yields the following expression for the flux per pole in terms of r_o and l_a:

$$\phi_p = B_{avg} \frac{\pi l_a}{p} (2r_o - l_a) \tag{4.14}$$

The flux per pole at the average radius of the stator winding (r_e) is the product of the average airgap flux-density (B_{avg}) and the pole pitch area ($\tau_p l_a$), i.e. [52]:

$$\phi_p(r_e) = B_{avg} \tau_p l_a \tag{4.15}$$

$$\phi_p = B_{avg} \frac{2\pi r_e l_a}{p} \tag{4.16}$$

where the pole pitch at the average radius is $\tau_p(r_e) = 2\pi r_e/p$ and r_e is given as [15][24]:

$$r_e = \frac{r_o + r_i}{2} \tag{4.17}$$

4.3.2 Back - EMF

The back-EMF at no load is defined by the change of the flux linking a coil with respect to time. By differentiating the first harmonic of the magnetic flux waveform, $\Phi_{p1} = \Phi_p \sin\omega_e t$ and by multiplying with $N_{ph}k_{\mathrm{w1}}$ the instantaneous back-EMF (e_f) can be written as [15]:

$$e_f = \omega_e N_{ph} k_{\mathrm{w1}} \Phi_p \cos\omega_e t \tag{4.18}$$

where N_{ph} is number of turns per phase, k_{w1} is the fundamental winding factor and ω_e is the electrical angular speed and is given by $\omega_e = 2\pi f$. The electrical frequency (f) can furthermore be expressed as:

$$f = \frac{n_s p}{2} \tag{4.19}$$

where n_s is the shaft speed in revolutions per second (rps). By dividing the peak value of eqn (4.18) by $\sqrt{2}$ and substituting eqn (4.19), the *rms* value of the back-EMF is obtained as:

$$E_f = \frac{2\pi f}{\sqrt{2}} N_{ph} k_{\mathrm{w1}} \Phi_p \tag{4.20}$$

$$= \frac{\pi}{\sqrt{2}} p N_{ph} k_{\mathrm{w1}} \Phi_p n_s = k_E n_s \tag{4.21}$$

where k_E is the EMF constant.

The back-EMF equation can be written, in terms of the PM length in the radial direction (l_a), by substituting eqn (4.14) into eqn (4.21). The EMF induced in the stator of the double rotor-inner (single) stator axial flux PM machine then takes the following form:

$$E_f = \frac{\pi^2}{\sqrt{2}} N_{ph} k_{\mathrm{w1}} B_{avg} n_s l_a (2r_o - l_a) \tag{4.22}$$

The average flux-density is $B_{avg} = B_{mg}/\alpha_i$ where B_{mg} is calculated according to eqn (4.4) and α_i according to eqn (4.8).

For a machine with a concentrated full-pitch overlapping winding configuration, the total number of slots is $Q_s = m_1 p$. The number of coils per phase (Q_c) is given by:

$$Q_c = \frac{Q_s}{2m_1} \tag{4.23}$$

The number of turns per phase (N_{ph}) is calculated by multiplying the number of coils per phase with the number of turns per coil as:

$$N_{ph} = Q_c N_c = \frac{Q_s}{3}\frac{N_c}{2} \tag{4.24}$$

The width of a coil in the circumferential direction (w) as shown in Fig. 4.12a can be approximated by [14]:

$$\mathrm{w} = 2r_e \sin\frac{\theta_{re}}{p} \tag{4.25}$$

where θ_{re} is the coil-width-angle at average radius r_e and is given as [14]:

$$\theta_{re} = (\frac{r_i - g}{r_e})\frac{\pi}{3} \tag{4.26}$$

The n^{th} harmonic winding factor (k_{wn}) consists of a distribution factor (k_{dn}) and a pitch factor (k_{pn}) and the general formulas are [45]:

$$k_{wn} = k_{dn}k_{pn} \tag{4.27}$$

$$= \frac{\sin(nq\tau_s/2)}{q\sin(n\tau_s/2)}\cos(n\tau_c) \tag{4.28}$$

where τ_s and τ_c are the slot pitch and coil pitch in electrical degrees respectively. The distribution factor is defined by the ratio of the phasor sum of the individual coil voltages to the arithmetic sum of the coil voltages, whereas the pitch factor is defined by the ratio of the voltage induced in a short-pitched coil to the voltage induced in a full-pitched coil.

4.3.3 Electromagnetic Torque

The average electromagnetic torque (T_{elm}) developed by an axial flux PM motor loaded with armature current (I_a) can be written as [15]:

$$T_{elm} = \frac{p}{\pi} m_1 N_{ph} k_{\mathrm{w}1} \phi_p I_a \tag{4.29}$$

In order to obtain the rms value for sinusoidal current, eqn (4.29) is multiplied by the coefficient $\pi\sqrt{2}/4 \approx 1.11$ to obtain the following expression for T_{elm} [15]:

$$T_{elm} = \frac{m_1}{2\sqrt{2}} p N_{ph} k_{\mathrm{w}1} \phi_p I_a = k_T I_a \tag{4.30}$$

where k_T is the torque constant.

The specific electric loading of a machine is defined as the peripheral current loading around the airgap perimeter, that is, the number of ampere-conductors per meter around the stator surface that faces the airgap. The specific electric loading is a function of the radius (r) and its peak value is given by [15][55]:

$$A_s(r) = \frac{\text{Total ampere} - \text{conductors}}{\text{Airgap perimeter}} \tag{4.31}$$

$$= \frac{\sqrt{2}\,2m_1N_{ph}I_a}{2\pi r} = \frac{\sqrt{2}\,m_1N_{ph}I_a}{\pi r} \tag{4.32}$$

By replacing the radius (r) with the following expression for the average radius (r_e):

$$r_e = \frac{2r_o - l_a}{2} \tag{4.33}$$

the peak specific electric loading formula then takes on the following form:

$$A_s(r_e) = \frac{2\sqrt{2}\,m_1N_{ph}I_a}{\pi(2r_o - l_a)} \tag{4.34}$$

For small PM machines, A_s is usually in the range of 10 000 - 40 000 A/m [53].

Furthermore, the *rms* current density for a conductor can be calculated as $J = 4I_a/(\pi d^2)$, where d is the diameter of the conductor in meters.

4.3.4 Losses and Efficiency

The losses in a machine can be separated into losses occurring in the stator and rotor. Fig. 4.14 shows a power flow diagram for a generator, and the losses occurring in the rotor (before the airgap) and in the stator (after the airgap) can be seen. For machines without stator

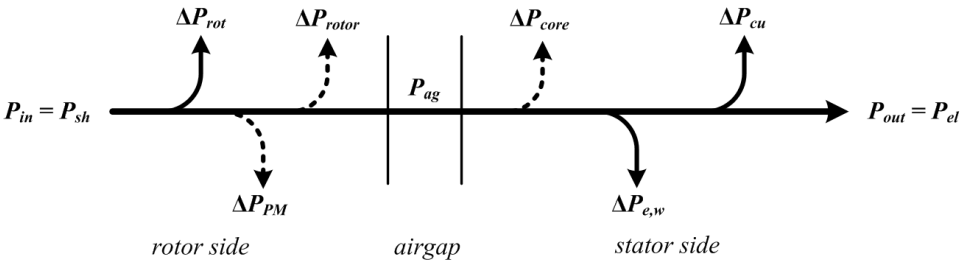

Figure 4.14: Power flow diagram for a generator

and rotor cores, the core losses (ΔP_{core}) and eddy current losses in the rotors (ΔP_{rotor}) are non-existent. In slotless machines like the sustainable generator, the flux does not change significantly in the ferromagnetic backing plates and PMs over time, since the field lines experience a constant permeability, unlike in slotted machines, where the permeability changes due to the slots of the machine [15]. Therefore, no eddy current losses will be induced in the backing plates and PMs ($\Delta P_{PM} = 0$). The only existing losses are the rotational losses (ΔP_{rot}), the eddy current losses in the stator windings ($\Delta P_{e,w}$) and the copper losses (ΔP_{cu}).

4.3.4.1 Stator Winding Losses (Copper Losses)

When current passes through a conductor with finite resistance, losses are produced in form of heat, which are known as copper losses or I^2R losses. The per phase stator (armature) resistance for DC current with the average length of one turn (l_{avg}) can be expressed as [15][16]:

$$R_{dc} = \frac{N_{ph} l_{avg} \rho(T)}{a s_a} \tag{4.35}$$

where a is the number of parallel paths or conductors, s_a the surface area of the conductor, $\rho(T)$ is the resistivity of copper at temperature T and can further be calculated by:

$$\rho(T) = \rho_{20}(1 + 0.0039(T_c - 20)) \tag{4.36}$$

where ρ_{20} is the resistivity of copper at 20 °C and T_c is the operating temperature measured at the windings. The average length of one turn (l_{avg}) is the addition of the total active length ($2l_a$) and the total end-winding length (l_e) of the stator winding and can be expressed as:

$$l_{avg} = 2l_a + l_e \tag{4.37}$$

The total end-winding length for the concentrated full-pitch overlapping winding (l_{eo}) is the sum of the inner end-winding turn (l_{in}) and the outer end-winding turn (l_{out}) and can be approximated by the following formula [14]:

$$l_{eo} = l_{in} + l_{out} = \frac{4\pi r_e}{p} + 4g \tag{4.38}$$

Eqn (4.35) gives the DC resistance of the stator winding. For AC current, the winding resistance increases as a result of the skin effect. When an alternating current flows through a conductor, circulating eddy currents are induced inside the conductor. These induced eddy currents oppose the direction of flow of the current and forces the current to the boundary

(skin) of the conductor. As a result the current experiences a decreasing surface area and thus an increasing resistance, which is called the AC resistance (R_{ac}). The skin depth or depth of penetration (δ) is defined as the depth below the surface of the conductor at which the current density (J) has fallen to $1/e$ (about 0.37) of the current density at the surface (J_s). At low frequencies, δ has high values and decreases as the frequency (f) increases. If δ is deeper than the center of the conductor, the current is not limited by the skin effect and the current is flowing uniformly throughout the entire cross sectional area of the conductor, which is equivalent to the DC resistance. Therefore, if δ reaches a value less than half the wire diameter ($d/2$), R_{ac} starts to increase. The skin depth for any material can be calculated from eqn (4.39). The skin depth for copper is given by eqn (4.40), with the relative permeability ($\mu_{r,cu} = 1$), the permeability of vacuum ($\mu_0 = 4\pi \times 10^{-7}\,\mathrm{Vs/Am}$) and the resistivity of copper ($\rho_{cu} = 1.68\mathrm{e}^{-8}\,\Omega\mathrm{m}$) [24][56].

$$\delta = \sqrt{\frac{\rho}{\pi \mu_r \mu_0 f}} \tag{4.39}$$

$$\delta_{cu} = \frac{0.065}{\sqrt{f}} \tag{4.40}$$

According to literature, the DC resistance is equal to the AC resistance for small motors with round armature conductors with frequencies of 50 or 60 Hz [15]. The proposed machine topology uses conductors with a diameter of 0.7 mm. The maximum speed of the machine is 600 rpm, which is equal to an electrical frequency of 320 Hz. The resultant skin depth is calculated with eqn (4.40) and is 3.6 mm and is far greater than half the conductor diameter. Hence, $R_{ac} = R_{dc}$ and the copper losses can be calculated as:

$$\Delta P_{cu} = m_1 I_a^2 R_{dc} \tag{4.41}$$

4.3.4.2 Eddy Current Losses in the Stator Windings

For axial flux machines with slotted stator cores, the eddy current losses in the stator windings are generally neglected as the magnetic flux penetrates through the teeth and yoke and only a small leakage flux penetrates the windings through the slot space with conductors. This is not the case with slotless machines. The stator windings are fully exposed to the airgap flux and the motion of the PMs relative to the stator windings produces an alternating magnetic field through each conductor and as a result induces eddy currents [15]. PM machines generally have a non-sinusoidal airgap flux-density waveform. Consequently, the stator flux contains many harmonics, which induce eddy currents in the conductors as well. Neglecting the proximity effect, the eddy current losses for round conductors may be calculated using the following classical formula [24][15]:

$$\Delta P_{e,w} = \frac{m_1 \pi^3 d^4 l_a N_{ph} f^2}{8\rho} \sum_{n=1}^{\infty} n^2 [B_{mxn}^2 + B_{mzn}^2] \quad (4.42)$$

$$= \frac{m_1 \pi^3 d^4 l_a N_{ph} f^2}{8\rho} [B_{mx1}^2 + B_{mz1}^2] \eta_d^2 \quad (4.43)$$

where ρ is the specific mass density of the conductor, n are all time harmonics, B_{mxn} and B_{mzn} are the harmonic components of the magnetic flux-density in the x (tangential) and z (normal) directions. η_d is the coefficient of distortion of the magnetic flux-density. For $\eta_d = 1$, eqn (4.43) gives the eddy current losses for a purely sinusoidal magnetic airgap flux-density distribution and may be expressed as [15]:

$$\eta_d = \sqrt{1 + \sum_{n=2}^{\infty} \frac{(nB_{mxn})^2 + (nB_{mzn})^2}{B_{mx1}^2 + B_{mz1}^2}} \quad (4.44)$$

In conventional machines with a uniform flux-density distribution, the even time harmonics tend to go to zero, and can therefore be neglected [15]. The uncut HDD magnets used in the proposed machine topology inevitably produce a non-uniform flux-density distribution. The non-uniform flux-density waveform may be divided into its Fourier coefficients and it can be shown that the even time harmonics are not negligible, but have a significant magnitude. Thus, when computing eddy current losses, all time harmonics should be considered as in eqn (4.44). In coreless axial flux PM the tangential field component (B_{mx}) is usually very small compared to the axial field component (B_{mz}) and can be assumed to be negligible [15].

4.3.4.3 Rotational Losses

The rotational or mechanical losses (ΔP_{rot}) can be separated into friction losses in the bearings (ΔP_{fr}), windage losses (ΔP_{wind}) caused by the rotating rotor discs and ventilation losses (ΔP_{vent}) if a forced cooling system exists, i.e.:

$$\Delta P_{rot} = \Delta P_{fr} + \Delta P_{wind} + \Delta P_{vent} \quad (4.45)$$

The friction losses in bearings of small machines can be estimated by using the following formula [15]:

$$\Delta P_{fr} = 0.0 k_{fb} (m_r + m_{sh}) n_s \quad (4.46)$$

where m_r and m_{sh} are the mass of the rotors and shaft respectively. The factor k_{fb} is a bearing specific coefficient and is usually in the range of $1 - 3\,\mathrm{m}^2/\mathrm{s}^2$ for small machines [15].

Moreover, the windage losses for a rotating disc can be expressed as:

$$\Delta P_{wind} = \frac{1}{2} c_f \rho_{air} (2\pi n_s)^3 (r_o^5 - r_{sh}^5) \tag{4.47}$$

where c_f is the coefficient of drag for turbulent flow and R_e is the Reynolds number for a rotating disc with its outer radius (r_o) and shaft radius (r_{sh}) and are given by [15]:

$$c_f = \frac{3.87}{\sqrt{R_e}} \tag{4.48}$$

$$R_e = \rho_{air} \frac{r_o v}{\mu_{air}} = \frac{2\pi n_s \rho_{air} r_o^5}{\mu_{air}} \tag{4.49}$$

The specific mass density of air (ρ_{air}) and the dynamic viscosity of air (μ_{air}) at 1 atm and 20 °C are 1.2 kg/m^3 and 1.8×10^{-5} Pa respectively. Small axial flux PM machines can be designed without a cooling fan since the PMs in surface mounted machines create a fanning effect, thereby cooling the windings. Thus, the ventilation losses are zero and the rotational losses are the sum of the friction and windage losses, $\Delta P_{rot} = \Delta P_{f\&w}$.

4.3.4.4 Efficiency

Generally, efficiency (η) of a machine is the ratio of the output power (P_{out}) to the input power (P_{in}). In case of a generator, the output power is equal to the electrical power measured at the terminals of the generator (P_{el}), and the input power is same as the power measured at the shaft of the generator (P_{sh}). For a 3-phase generator the input and output powers are calculated as:

$$P_{el} = 3 V_a I_a \cos\phi \tag{4.50}$$

$$P_{sh} = T \omega_m = P_{el} + \Delta P \tag{4.51}$$

where V_a and I_a are the *rms* voltage and current at the terminals of the generator, $\cos\phi$ is the power factor at which the machine is operating, T and ω_m are the *rms* torque and rotational speed measured at the shaft of generator, and ΔP is the summation of all losses occurring during operation. The total losses (ΔP) for a machine without stator and rotor cores is given by:

$$\Delta P = \Delta P_{cu} + \Delta P_{e,w} + \Delta P_{f\&w} \tag{4.52}$$

and the efficiency of the machine can be expressed as:

$$\eta = \frac{P_{out}}{P_{in}} = \frac{P_{el}}{P_{el} + \Delta P} \tag{4.53}$$

4.3.5 Coreless Winding Inductance

Unlike conventional slotted axial flux PM machines, literature does not present a clear definition for the main and leakage inductances in a coreless or slotless machine [15]. For a non-salient pole machine, i.e. the magnets are placed on the surface of the rotor, the synchronous inductance (L_s) consists of the mutual (armature reaction) inductance (L_a) and the leakage inductance (L_l), since the d-axis and q-axis inductances are equal to the synchronous inductance [15][16][57].

$$L_s = L_a + L_l \tag{4.54}$$

For surface mounted PM machines L_a can be expressed as [15][16]:

$$L_a = \frac{m_1 \mu_0}{\pi} \left(\frac{2 N_{ph} k_{\mathrm{w1}}}{p} \right)^2 \frac{r_o^2 - r_i^2}{g'} \tag{4.55}$$

The equivalent airgap (g') for a coreless stator is the distance between the two ferromagnetic rotor discs and is given by [15]:

$$g' = 2 \left[(g_m + 0.5 h_{\mathrm{w}}) + \frac{h_M}{\mu_r} \right] \tag{4.56}$$

The total per phase leakage inductance (L_l) is expressed analytically as a sum of three components, i.e. [15]:

$$L_l = L_{1s} + L_{1e} + L_{1d} \tag{4.57}$$

$$= 4 \mu_0 \frac{N_{ph}^2 l_a}{pq} \left(\lambda_{1s} + \frac{l_e}{2 l_a} \lambda_{1e} + \lambda_{1d} \right) \tag{4.58}$$

where L_{1s} and λ_{1s} are the inductance and specific permeance for the leakage flux around the radial portions of conductors respectively (corresponding to slot leakage in classical machines), L_{1e} and λ_{1e} are inductance and specific permeance for the leakage flux associated with the end connections respectively, and L_{1d} and λ_{1d} are the inductance and specific permeance for the differential leakage flux, which are caused by higher space harmonics respectively. For coreless machines it is difficult to derive an accurate analytical expression for λ_{1s} [15]. λ_{1e} is usually estimated on the basis of experiments. However, they can roughly be estimated from the following semi-analytical equation, which holds for most winding configurations [15][16]:

$$\lambda_{1s} \approx \lambda_{1e} \approx 0.3q \tag{4.59}$$

where q is the slots per pole per phase. An expression for the differential leakage inductance can be directly derived from the armature reaction inductance as shown in [57]. The specific permeance of the differential leakage flux is [15][16]:

$$\lambda_{1d} = \frac{m_1 q \tau_p k_{\mathrm{w1}}^2}{\pi^2 g' k_{sat}} \tau_{d1} \tag{4.60}$$

where τ_{d1} is the differential leakage factor, and determined according to eqn (4.61). For coreless machines the magnetic material seldom goes into saturation, therefore k_{sat} can be assumed to be unity [15][16].

$$\tau_{d1} = \frac{1}{k_{\mathrm{w1}}^2} \sum_{n=2}^{\infty} \frac{k_{\mathrm{wn}}^2}{n^2} \tag{4.61}$$

In practical calculations it is convenient to use the following formula [15][16]:

$$\tau_{d1} = \frac{\pi^2 (10q^2 + 2)}{27} \sin\left(\frac{\pi}{6q}\right) - 1 \tag{4.62}$$

For non-overlapping and distributed winding configurations with $k_{\mathrm{w1}} < 1$, eqn (4.62) holds as the differential leakage factor is small due to the quickly declining n^{th} harmonic winding factor (k_{wn}). However, this is not the case for concentrated full-pitch overlapping windings, where the fundamental winding factor is equal to the n^{th} harmonic winding factor, i.e. $k_{\mathrm{w1}} = k_{\mathrm{wn}} = 1$ [45]. Hence, eqn (4.61) should be used to compute the differential leakage factor. Fig. 4.15 shows the differential leakage factor for concentrated full-pitch overlapping windings with $k_{\mathrm{wn}} = 1$. Finally, it is not difficult to show that $L_{1d} = L_a \tau_{d1}$ [15][57]. The differential leakage inductance is small compared to the armature reaction inductance, since τ_{d1} is small because of the square of the harmonic in the denominator.

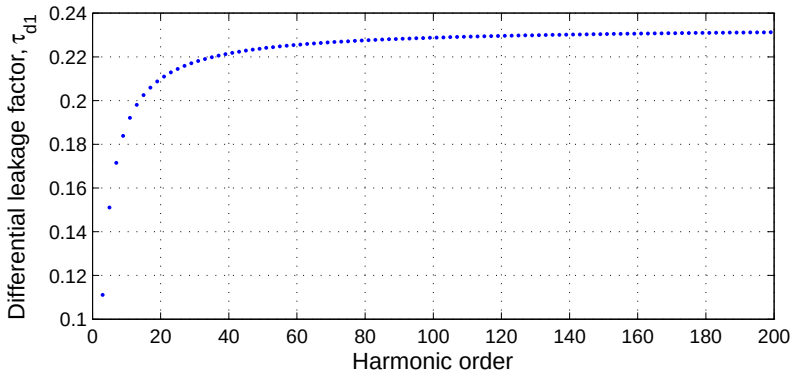

Figure 4.15: Differential leakage factor when using eqn (4.61)

4.3.6 Sizing Equations

Traditionally rotating machines are sized in relation with the $D_e^2 L_e$ sizing equation, which evaluates the machine on the basis of the airgap volume, electric and magnetic loading. D_e is the diameter at the center of the airgap and L_e is the effective stack length of a radial flux machine. However, sizing a machine in relation with its outer diameter (D_o) seems more reasonable, since it is more directly related to the volume and cost of the machine [54]. Hence, the sustainable generator is sized in relation to its outer radius (r_o). The formulas presented in this sub-section are derived from the classical axial flux machine theory presented in [54], where the *inner-to-outer PM radius* ratio (k_d) is kept constant. Due to the fixed shape of the magnets found in HDDs, the PM length in the radial direction (l_a) is used instead of k_d in the sizing procedure.

The main dimensions of a double rotor inner (single) stator axial flux PM machine can be calculated with the following parameters known: the PM length in the radial direction (l_a), the electric and magnetic loadings (A_s and B_{avg}), the rotational speed (n_s), the phase current flowing in the stator windings (I_a), the phase EMF-to-phase voltage ratio (ϵ), the power factor ($\cos\phi$) and the fundamental winding factor (k_{w1}).

By solving for I_a in eqn (4.34) and using eqn (4.22) the apparent electromagnetic power (S_{elm}) of the machine can be expressed as:

$$S_{elm} = m_1 E_f I_a \tag{4.63}$$

$$= \frac{\pi^3}{4} k_{\mathrm{w1}} B_{avg} A_s n_s l_a (2r_o - l_a)^2 \tag{4.64}$$

In terms of the active output power (P_{el}), S_{elm} can further be expressed as [28]:

$$S_{elm} = \frac{\epsilon P_{el}}{\cos\phi} \tag{4.65}$$

where ϵ is the phase EMF-to-phase voltage ratio ($\epsilon > 1$ for generators and $\epsilon < 1$ for motors) and is given by:

$$\epsilon = \frac{E_f}{V_a} \tag{4.66}$$

Inserting eqn (4.65) into eqn (4.64), the outer radius of the machine (r_o) in terms of the PM length in the radial direction (l_a) yields the following polynomial equation:

$$r_o^2 l_a - r_o l_a^2 + \frac{l_a^3}{4} - \frac{\epsilon P_{el}}{\pi^3 k_{\mathrm{w1}} B_{avg} A_s n_s \cos\phi} = 0 \tag{4.67}$$

Finally, the outer radius of the machine can be calculated for a specific output power (P_{el}) by finding the roots of the polynomial equation.

The power density, ξ of an axial flux machine can be expressed as [52]:

$$\xi_v = \frac{P_{el}}{\pi r_o^2 l_{stk}} \quad (\mathrm{W/m^3}) \tag{4.68}$$

$$\xi_m = \frac{P_{el}}{m_{gen}} \quad (\mathrm{W/kg}) \tag{4.69}$$

where the axial stack length of the axial flux PM machine is $l_{stk} = g' + 2h_r$, where g' is the equivalent airgap from eqn (4.56), h_r is the thickness of the rotors in the axial direction and m_{gen} is the total mass of the generator in kg. Protrusion of the end windings are neglected in eqn (4.68).

4.3.7 Dimensions of the Sustainable Generator

In chapter 3, a sustainable wind energy capture and storage system was presented and the requirements for the electrical generator were specified. With the theoretical model of the sustainable generator developed and the requirements specified, the dimension of the sustainable axial flux PMSG can be calculated.

The outer PM radius is the most important dimension of axial flux PM motors, since its output power increases to the cube of its outer radius [15]. An iterative design procedure was used to determine the dimensions of the generator. A flow chart of the procedure is shown in Fig. 4.16. The main objective of the iterative design procedure is to satisfy the requirements calculated in chapter 3, which are as follows:

- The electrical output power requirement is 277 W, with a phase current and phase voltage of 3 A and 30.78 V, respectively.
- The rated speed of generator is 347 rpm.
- The generator is assumed to supply a rectifier load, which can be approximated as a purely resistive load; therefore, the power factor is unity.
- The diameter of the stator winding wire is 0.7 mm.

Furthermore, the proposed sustainable generator topology inherently has the following constraints and constants:

- The dimensions of the HDD PMs selected for the generator are fixed. Various magnets from HDDs were investigated and it was found that the dimensions of the magnets vary. However, PMs with the dimensions according to Fig. 4.13 were chosen to be as follows:

  - The length of the PMs in the radial direction (l_a) is 0.015 m.
  - The magnet height (h_M) is 0.0029 m, the backing plate height (h_r) is 0.0038 m, the pole pitch at average radius ($\tau_p(r_e)$) is 0.01919 m, the remanent flux-density (B_r) is 1.32 T, the effective airgap (g) is 0.01 m and the peak specific magnetic loading (B_{mg}) equates to 0.403 T according to eqn (4.4). The average non-sinusoidal flux-density for the uncut magnets is $B_{avg} = B_{mg}/\alpha_i$ where α_i was computed with the 2D-FEA to be 0.38 (see Table 5.2).

- The fundamental winding factor (k_{w1}) is unity, because of the concentrated full-pitched overlapping wave winding configuration chosen.

Finally, the following initial assumptions for the iterative solution are made:

- The peak specific electric loading (A_s) is set to 15 000 A/m, in order to ensure thermal integrity of the coreless machine.
- The phase EMF-to-phase voltage ratio (ϵ) is set to 1.5, due to the relatively high resistance of the windings, resulting from the small diameter of the wire used.

The iterative design procedure was run according to Fig. 4.16 with the above mentioned constraints and variables. The outer radius of the sustainable generator was determined to 0.264 m. It was decided this machine of such a size cannot be built from redundant materials, due to concerns about the mechanical integrity of the machine. The outer radius was therefore required to be decreased to ensure mechanical integrity. In order to decrease the outer radius for the same output power, the following can be done: increasing the specific electric loading, increasing the number of turns per phase, increasing the flux per pole or cascading several individual generator stages axially. The stator conductors are held in position by an epoxy resin structure, which has a low thermal conductivity. Thus, the electric loading of the machine cannot be increased due to the risk of developing cooling issues with the machine. An increase in number of turns is limited, since the wire diameter selected was 0.7 mm and a bigger airgap cannot be tolerated due to the fact that the flux per pole for magnets sourced from HDDs is low and cannot be altered. Hence, the cascading technique seems to be the best option. This method is also used for increasing the power output of commercial coreless axial flux PM generators [35]. The cascaded generators can be connected in series or in parallel, thereby increasing either the total back-EMF or the total current of the cascaded generators respectively. Since the phase EMF-to-phase voltage ratio of the generator is relatively high ($\epsilon = 1.43$), which suggests a poor voltage regulation for the machine, a series connection of the generators is considered.

The iterative design procedure was run a second time with two generators connected in series. Since the generators are connected in series, the phase voltage of one generator is half for the same phase current. The resultant outer radius for each of the cascaded generators is found

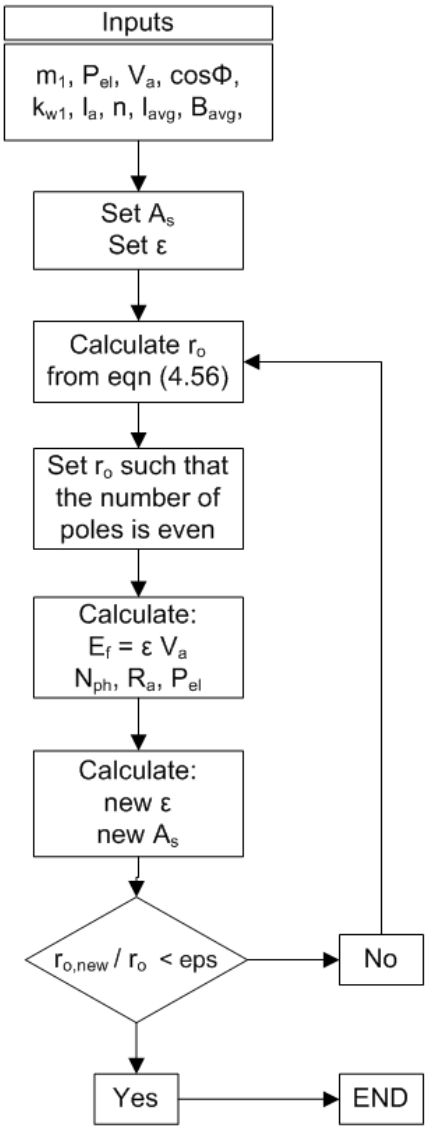

Figure 4.16: Flow chart of design procedure

to be 0.203 m. The machine specifications for both generator concepts are presented in Table 4.1.

Both concepts produce the required power, phase voltage and phase current. The current loading for both machine concepts is below the 15 000 A/m threshold, ensuring thermal integrity of the machines. The single generator concept has 20 poles more than the cascaded concept, which will lead to higher eddy current losses, due to the higher electrical frequency experienced by the windings. The total phase winding resistance of the cascaded generators is 6.78 Ω, and is 53 % higher than the resistance of the single generator concept (4.44 Ω). Thus, the voltage regulation of the single generator concept is better compared to that of

Table 4.1: Machine specifications for both generator concepts

Method Description	**Single Machine Concept**	**One Machine of Cascaded Machine Concept**
Average flux-density per pole, B_{avg} [T]		0.153
Phase current, I_a [A]		3
Power factor, $\cos\phi$		1
Fundamental winding factor, k_{w1}		1
Rotational speed, n [rpm]		347
Electrical output power, P_{el} [W]	276	138.5
Phase voltage, V_a [V]	30.68	15.39
Back EMF, E_f [V]	44	25.55
Number of uncut HDD magnets	21	16
Number of poles	84	64
Electrical frequency, f [Hz]	243	185
Number of turns per phase, N_{ph}	924	704
Number of turns per coil, N_c		22
Phase resistance, R_{ph} [Ω]	4.44	3.39
Peak specific electric loading, A_s [A/m]	14636	14588
Voltage regulation factor, ϵ	1.43	1.66
Outer radius, r_o [m]	**0.264**	**0.203**

the cascaded generator concept. Both concepts have 22 turns per coil, with the cascaded generators having 924 turns per phase and 704 turns per phase for the single generator concept. The total thickness of a coil with 22 turns and 0.7 mm wire was found to be between 5.5 - 6 mm, and is within the desired region as illustrated in Fig. 5.11.

4.4 Conclusion

The most common machine topology for a sustainable generator built from redundant materials were reviewed, together with the most important winding configurations. The proposed machine is an axial flux PM generator fitted with a concentrated full-pitch overlapping wave winding, which ensures a symmetrical and balanced phase voltage output, despite the non-uniform airgap flux-density distribution produced by the PMs of HDDs. Furthermore, it was shown that the proposed topology reduces the large proportion of coil inter-connecting leads associated with direct-drive wind generators which have many poles.

The performance of the proposed sustainable generator was predicted with classical machine theory. These results are compared to numerical and experimental results, and will be presented in a subsequent chapter. In order to accurately analyze the concentrated full-pitch overlapping wave winding, the theory of concentrated overlapping full-pitch windings

was adapted. Using the new sizing methodology presented in the chapter, the sustainable generator was sized according to the requirements specified in chapter 3 and its dimensions were calculated. Two machine concepts together with their advantages and disadvantages were presented and it was concluded that two generator stages should be connected in series, in order to ensure mechanical integrity of the machines.

The following chapter will present the numerical analysis of the proposed machine topology.

Chapter 5

Numerical Analysis of the Sustainable Generator

This chapter presents the numerical analysis of the proposed machine topology for the sustainable generator. Firstly, the 2D and 3D models are described and the electromagnetic simulation results are presented. A method for accurately calculating the flux per pole for the non-sinusoidal flux-density distribution of uncut HDD magnets is then presented. Finally, the influence of the PM dimensions on the machine performance is determined. Appendix A gives a comprehensive account of the numerical analysis process, presenting detailed descriptions of the techniques and circuits used to obtain the simulation results.

5.1 Model Description

The FEA-models were constructed according to the machine specifications determined in the previous chapters and are given in Table 5.1.

Table 5.1: Machine Specifications

Specification	**Value**
Outer radius, r_o [m]	0.203
Inner radius, r_i [m]	0.188
Number of HDD Magnets	16
Backing plate height, l_r [m]	0.0038
Magnet height, h_M [m]	0.0029
Magnet width, τ_p at r_e [m]	0.01919
Magnet depth, l_a [m]	0.015
Number of poles, p	64
Number of active poles, $p/2$	32
Effective airgap, g [mm]	10
Number of turns per coil, N_c	22
Remanent flux-density, B_r [T]	1.32

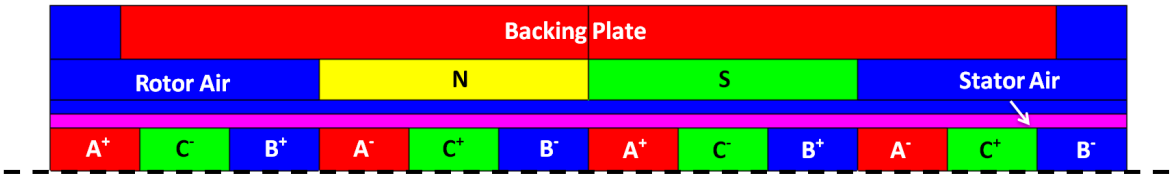

Figure 5.1: 2D-FEA model

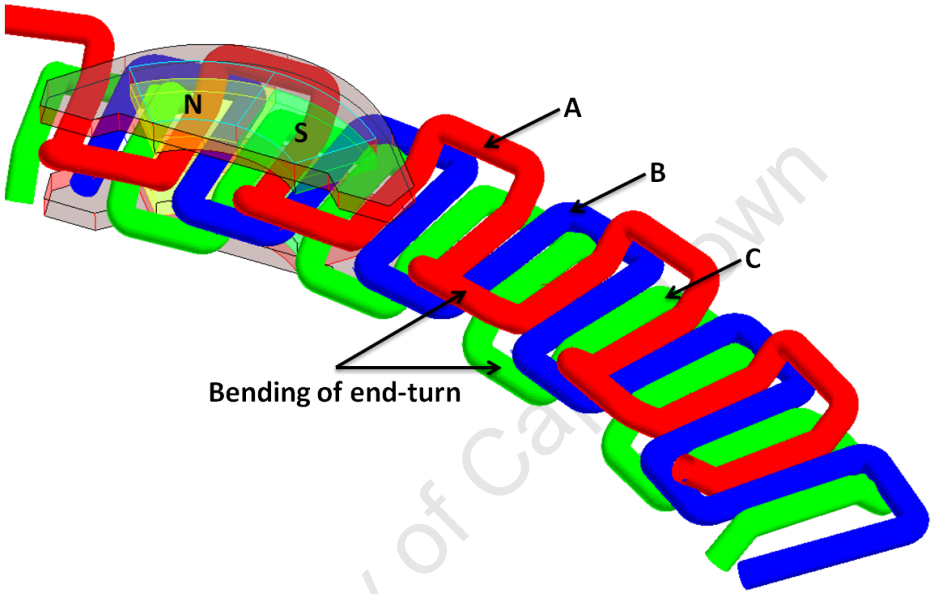

Figure 5.2: 3D-FEA model

In the 3D-FEA, the machine is modeled to scale, but periodicity and symmetry of the machine are taken into account. For the 2D-FEA, the axial flux machine is simulated by introducing a radial cutting plane at the average radius, which is then developed into a 2D flat model [15]. The machine is then analyzed as a linear machine as shown in Fig. 5.1. The 3D-FEA simulations are very time consuming and require significant computation power. Therefore, knowledge about the boundary conditions is of great importance. For the 2D model, Neumann boundary conditions (symmetry) is assigned along the dashed line in Fig. 5.1 and only half of the machine is modeled. Symmetry conditions could not be utilized for the 3D-model, since the complete winding could only be modeled in the 3D environment compared to half a winding in 2D as illustrated in Fig. 5.2 and Fig. 5.1 respectively. Dirichlet boundary conditions (tangent magnetic field) is applied to the top of the backing plate in the 2D-model, to ensure that the flux lines are constrained within the boundary. For the 3D-FEA, the complete model is placed in an infinity box, which resembles the air around the actual machine. Only one HDD magnet, i.e. a sixteenth of the PM rotor discs is modeled, because the PM rotor is repeatable after every HDD magnet. Since the number of poles for the modeled section is

even, even/cyclic periodical boundary condition is applied to the sides of both the 2D- and 3D-model. The depth of the 2D simulation was set to 15 mm, which is equal to the length of the magnets in the radial direction (l_a). Materials were defined for the different regions of the model. Also, the remanent flux-density of the PMs was defined. Since the magnet grade of the HDD PMs was unknown, the flux-density at the center of the airgap was measured with a Gaussmeter. The remanent flux-density of the 3D-FEA model was then adjusted until the airgap flux-density was equal to the measured value. The remanent flux-density value was found to be 1.32 T, which is equivalent to N42 grade NdFeB magnets. The geometry was then meshed and coupled to an external circuit. Details about the meshing process and the relevant circuits are presented in Appendix A. Finally, the model was solved by stepping the rotor along the stator. Post processing of the simulation was done to determine the performance of the machine.

5.2 Magnetic Flux

The flux path for the 2D-FEA model is shown in Fig. 5.3. As can be seen, the flux lines are more concentrated around the poles. The "imaginary poles" are clearly visible on the left and the right side of the model. The fringing flux at the ends of the poles in Fig. 5.3 is creating minor N- and S-poles as shown in Fig. 5.5. For 3D-FEA, the flux-density distribution is usually illustrated by means of magnetic field arrows or by introducing 2D-grids, since the graphical representation of the flux lines in 3D is meaningless. The airgap flux-density distribution for the 3D-model is shown on the left of Fig. 5.4 and the flux-density distribution of the HDD magnets and the backing plates is shown on the right.

Fig. 5.5 shows the normal component of the no-load airgap flux-density waveform at the average radius (r_e). There is good agreement between the 2D and 3D results, thereby verifying the accuracy of the 2D model. The fringing flux is exacerbated in the 2D model than in 3D, since the edges of the HDD PMs are straight in the 2D model compared to the skewed edges that exist in the actual PMs and the 3D model (see Fig. 5.1 and Fig. 5.2). The peak values of the airgap flux-density for the 2D-FEA and 3D-FEA at the average radius are 0.415 T and 0.406 T respectively. The tangential component of the flux-density is very small for coreless machines [15], and was found to be negligible.

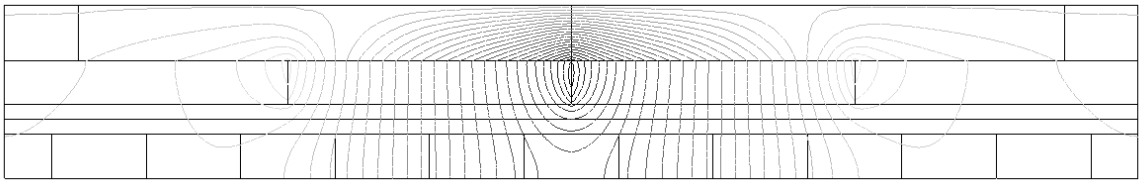

Figure 5.3: Flux paths of the 2D-FEA model

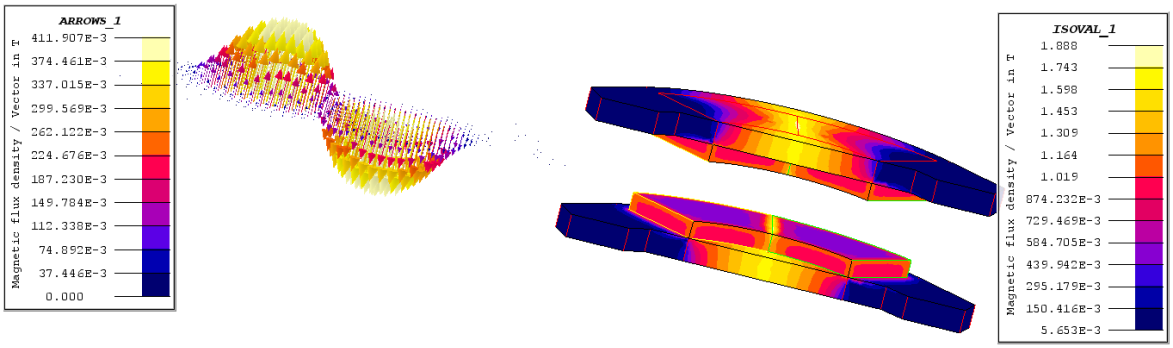

Figure 5.4: Flux-density distribution for the 3D-FEA model: In the airgap (left) and in the HDD magnets and the backing plates (right)

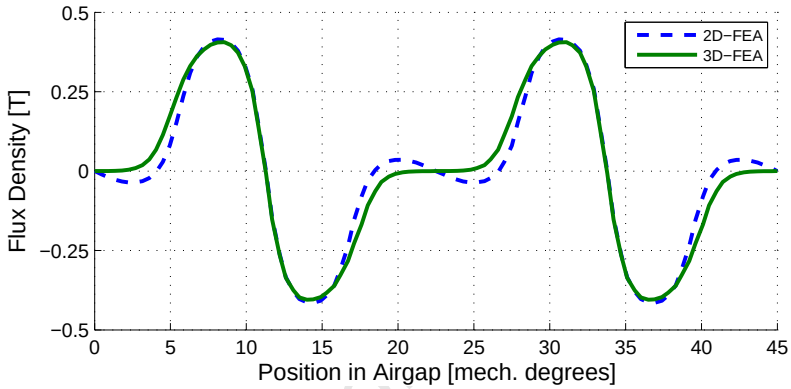

Figure 5.5: Normal component of the no-load airgap flux-density distribution at the average radius

5.2.1 Accurate Estimation of the Flux per Pole for the HDD magnets

In order to predict the theoretical machine performance precisely, the flux per pole of the uncut HDD PMs needs to be estimated accurately, which was achieved by means of the 2D- and 3D-FEA.

The uncut PMs from HDDs inherently produce a non-uniform flux-density distribution, since the magnets are not evenly distributed along the perimeter of the rotor. Fig. 5.6 shows the non-sinusoidal flux-density distribution for two pole pitches (= 11.25 electrical degrees) for the uncut magnets calculated with the 2D- and the 3D-FEA. The third trace in Fig. 5.6 is that of a sinusoidal flux-density distribution with a peak value equal to that of the uncut magnets. It is clearly visible that the total flux per pole (area under the curve) for the uncut magnets is greater than that of the sinusoidal flux-density distribution. In [58] the flux per pole was calculated by assuming a sinusoidal flux-density distribution for the uncut magnets, and it was shown that the performance of the machine was underestimated. Therefore, the flux per pole needs to be calculated on the basis of the non-sinusoidal flux-density distribution in the airgap.

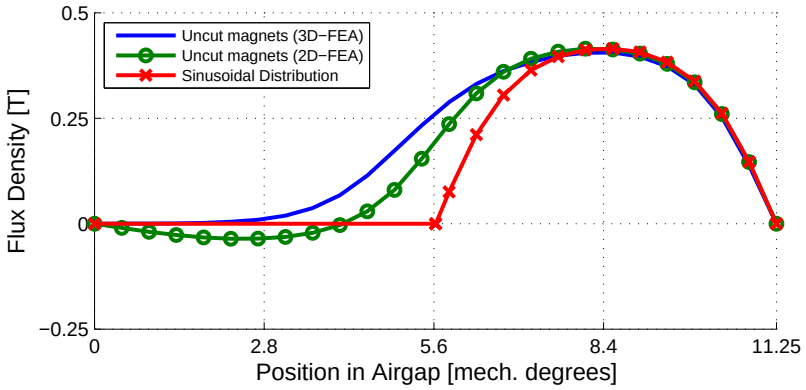

Figure 5.6: Flux-density distribution for the uncut magnets over two pole pitches

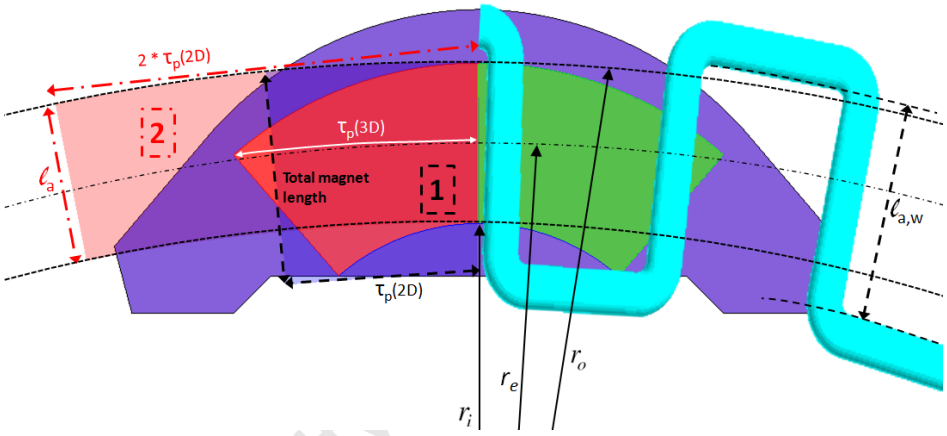

Figure 5.7: Illustration of uncut HDD magnet

The estimation of the average flux per pole is difficult, due to the peculiar shape of the magnets. From Fig. 5.7, it is noticeable that the active length of the stator winding ($l_{a,w}$) is not equal to the length of the PMs in the radial direction (l_a) as is the case in conventional machines. The discrepancy between both lengths can be attributed to the peculiar shape of the PMs. Hence, the pole area is greater than that calculated from eqn (4.15). Therefore, alternative methods for estimating the average flux per pole were investigated, and the results are shown in Table 5.2.

The flux per pole is the product of the average airgap flux-density and the pole area as given by eqn (4.11). The average flux-density for the non-sinusoidal distribution is given by eqn (4.8). As already mentioned, a sinusoidal flux-density distribution is assumed for the uncut magnets in [58], and this resultant flux per pole will therefore be taken as the reference (Method 1). The flux obtained from the 3D-FEA at average radius (Method 2) overestimates the average flux-density as shown in Fig. 5.6. From Fig. 5.7, it can be seen that the path at the average radius extends over the edges of the magnets, and consequently the longest length of the

Table 5.2: Methods for calculation of the flux per pole for uncut magnets

No.	Method Description	Flux [μWb]
1	Sinusoidal distribution over 1 pole pitch from 2D-FEA (reference)	36.95
2	Average over 2 pole pitches from 3D-FEA at average radius, r_e ($\alpha_i = 0.447$)	52.36
3	Average over 2 pole pitches from 2D-FEA ($\alpha_i = 0.38$)	44.17
4	Average over 1 pole pitch from 3D-FEA (2D-grid with total magnet length; No. 1 in Fig. 5.7)	45.77
5	Average over 2 pole pitches from 3D-FEA (2D-grid with active length, l_a; No. 2 in Fig. 5.7)	43.63

magnet ($\tau_p(3D)$ in Fig. 5.7) is taken, thereby overestimating the average flux-density. Method 3 uses the airgap flux-density distribution at the average radius of the 2D-model. Since, the 2D-model has a shorter pole pitch at the average radius ($\tau_p(2D)$ in Fig. 5.7), Method 3 gives a more accurate approximation of the flux. In order to verify Method 3, two 2D-grids were created in the 3D-FEA model and are labeled 1 and 2 in Fig. 5.7. The total flux is calculated by integrating the flux-density over the area of the grids. Grid no. 1 (Method 4) has a width of one pole pitch ($\tau_p(2D)$) and a depth of the total magnet length. Grid no. 2 (Method 5) has twice the width of grid no.1 ($2 \cdot \tau_p(2D)$), but has a shorter depth, which is equal to the PM length in the radial direction (l_a). Both methods yield similar results when compared to that of Method 3, with Method 4 having a 3.6 % higher value and Method 5 having a 1.2 % lower value for the flux per pole. Thus, the flux per pole determined with Method 3 was taken for the theoretical machine performance analysis.

5.2.2 Armature Reaction

When the armature current passes through the stator coils, an alternating magnetic field is created, which is known as the armature reaction. To obtain the airgap flux-density due to armature reaction, the magnets are deactivated and the full load current is injected into the phase windings. The armature reaction waveform at 3 A is shown in Fig. 5.8. The armature reaction has a magnitude of 8 mT, which is negligible when compared to the peak value of the no-load flux-density, which is 0.415 T for the 2D-FEA. This is expected due to the large airgap present in coreless machines. Thus, the load airgap flux-density is taken to be approximately equal to that of the no-load.

5.3 Back - EMF

The back-EMF was simulated under open-circuit conditions by connecting the terminals of machine to large resistors, thereby ensuring that no current flows through the windings (see Fig. A.4). Fig. 5.9 shows good agreement between the simulated back-EMF waveform for

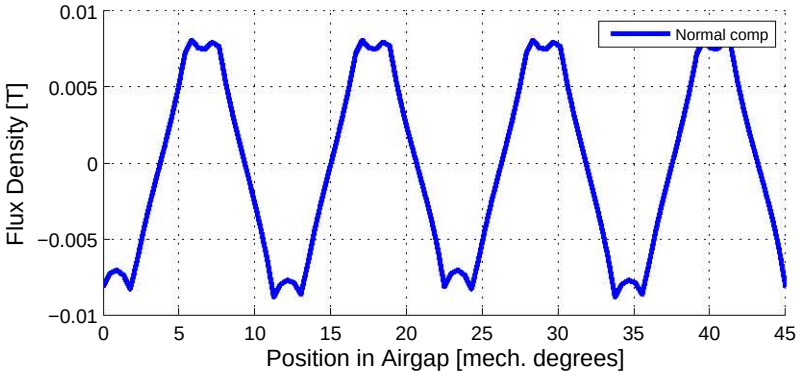

Figure 5.8: Armature reaction airgap flux-density at 3 A

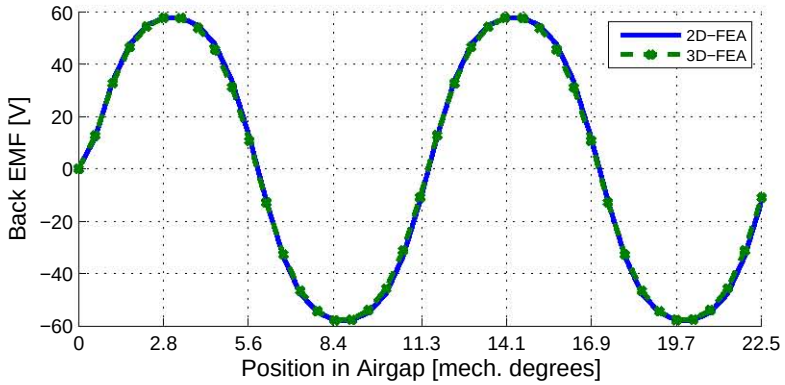

Figure 5.9: 2D and 3D-FEA results of no-load back EMF at 600 rpm

the 2D- and 3D-FEA. At 600 rpm, the *rms* value of the back-EMF for the 2D- and 3D-FEA was 44.68 V and 43.76 V respectively. The harmonic content of the back-EMF waveform was further investigated. In coreless machines, the flux linkage waveform is approximately sinusoidal in shape due to the absence of harmonics created by an iron core, stator slots and magnetic saturation [15][24]. Since the armature reaction is negligible, the only source of flux linkage harmonics are the flat shaped PMs, which inherently introduce some 3^{rd}, 5^{th} and 7^{th} harmonic components [17][24]. The harmonics in the back-EMF waveform determined from the FEA and experimentally are shown in Fig. 5.10. The total harmonic distortion (THD) for the back-EMF waveforms are 8.07 %, 6.46 % and 4.85 % for the 2D-, the 3D-FEA and the experimental prototype respectively. Note that eqn (5.1) is used to compute the THD [46].

$$V_{THD}[\%] = \frac{\sqrt{\sum_{k=2}^{max} V(k)^2}}{V(1)} \cdot 100 \tag{5.1}$$

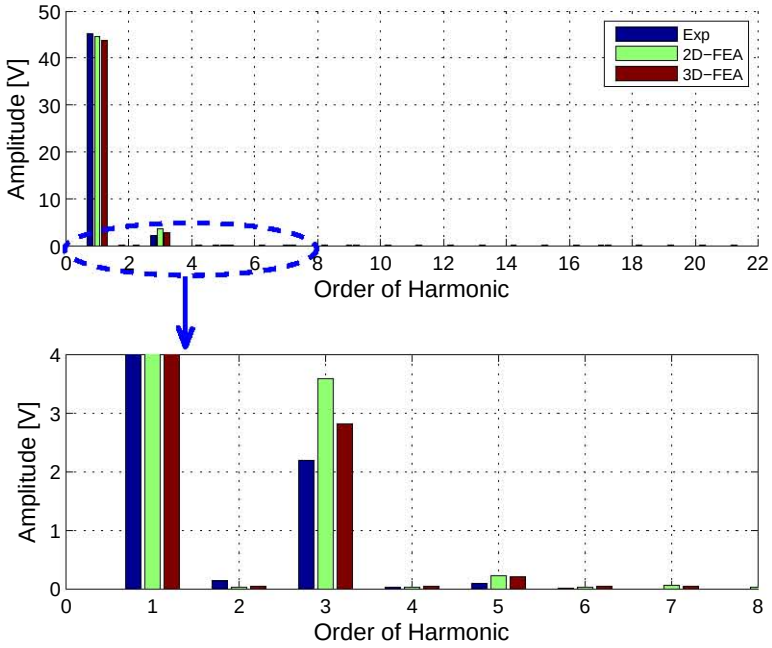

Figure 5.10: No-load back-EMF waveform harmonics at 600 rpm for the FEA simulations and prototype

Influence of the Thickness of a Coil Side on the back-EMF Production

In the theoretical analysis, the predicted back-EMF waveform is calculated under the assumption that the coils consists of only one infinitely thin conductor with N_{ph} number of turns. In reality, the conductors of a phase coil are spread across the coil side, which results in a small phase shift of the EMF waveforms of the individual conductors. If the thickness of a coil side exceeds a certain value, the back-EMF waveforms of some conductors cancel each other out, which reduces the EMF production. A 3D-FEA simulation was performed with varying thickness of a coil side, and the normalized back-EMF is shown in Fig. 5.11. It can be seen that the thickness of a coil side should not exceed 6 mm. Beyond this point, the back-EMF is substantially reduced.

5.4 Electromagnetic Torque

Electromagnetic torque in an axial flux PM machine is produced by the tangential interaction between the stator and the rotor. This torque is maximum when the angle between the current and the flux linkage vectors is 90^o [49]. Cogging torque is not present in coreless machines due to the absence of stator slots. Therefore, the torque ripple in an axial flux PM machine is caused by the current waveform that repeats itself every 90^o, since the electromagnetic

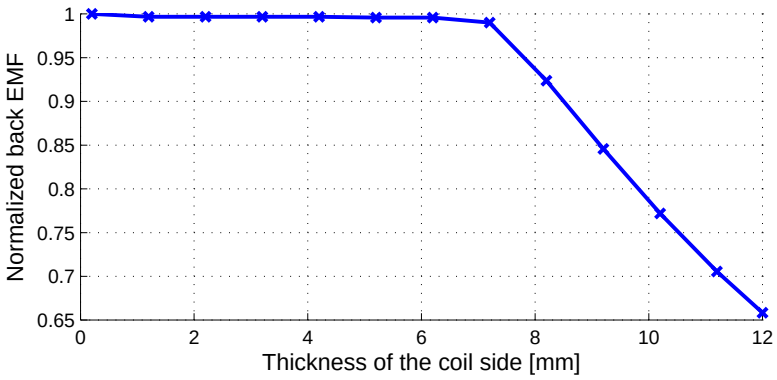

Figure 5.11: Influence of thickness of a coil side on back EMF production

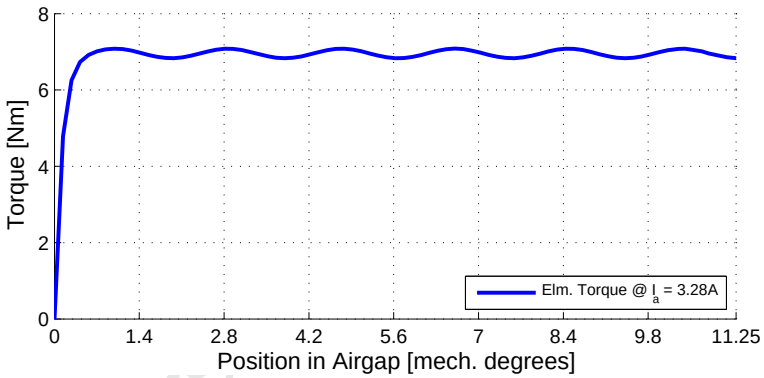

Figure 5.12: Torque ripple of the simulated coreless axial flux PM machine

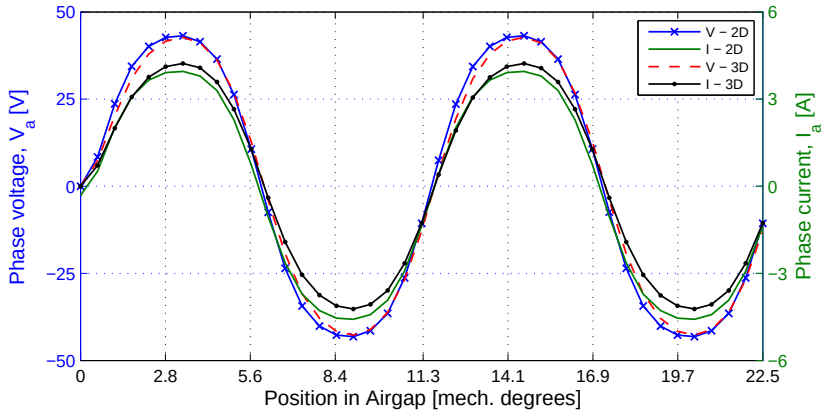

Figure 5.13: 2D and 3D-FEA results of phase voltage and current at 600 rpm

torque is proportional to the current according to eqn (4.30). This repetition introduces a 6^{th} harmonic component in the torque waveform [24]. The sub-harmonics of the torque ripple can be ignored due to the large effective airgap in coreless machines [17]. Fig. 5.12 shows the electromagnetic torque of the simulated sustainable generator loaded with a phase current of 3.28 A. The *rms* torque is 6.95 Nm and the torque ripple containing the 6^{th} harmonic component can clearly be seen in Fig. 5.12.

Fig. 5.13 shows the instantaneous phase voltage and current of the generator at a shaft speed of 600 rpm. Again, good agreement between the 2D and 3D results is clearly visible. For the 2D-FEA, the phase voltage is 33.13 V when loaded with a phase current of 3.29 A. The electrical output power of the generator measured at its terminals at this loading point is 327 W.

5.5 Eddy Current Losses

Eddy current losses in the stator windings were computed using the 2D model, since its accuracy has been verified by the 3D model. The eddy current losses for one electrical cycle at a shaft speed of 600 rpm are shown in Fig. 5.14. The frequency of the per phase eddy currents is twice that of the electrical frequency of the machine. This can be attributed to the positive and negative parts of the flux-density waveform, since eddy currents are induced regardless of the direction of the flux. The peak value of the per phase eddy current waveforms is 8 W and the total eddy current losses is the sum of all three phases, which is equal 9.1 W.

Eddy current losses were also computed in the backing plates and PMs. As expected, these were found to be in the microwatt region and can therefore be neglected.

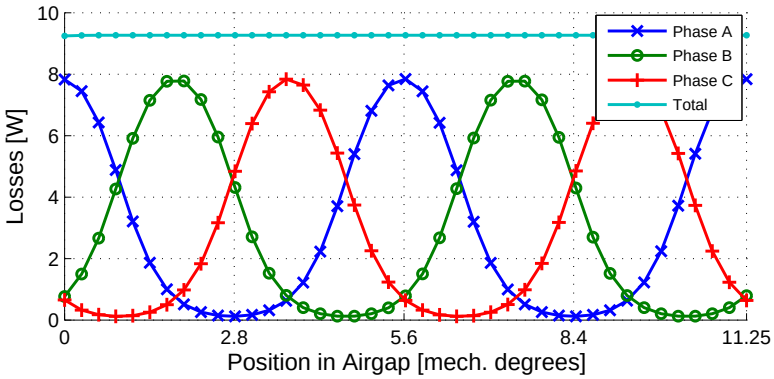

Figure 5.14: Eddy current losses induced in the stator windings at 600 rpm

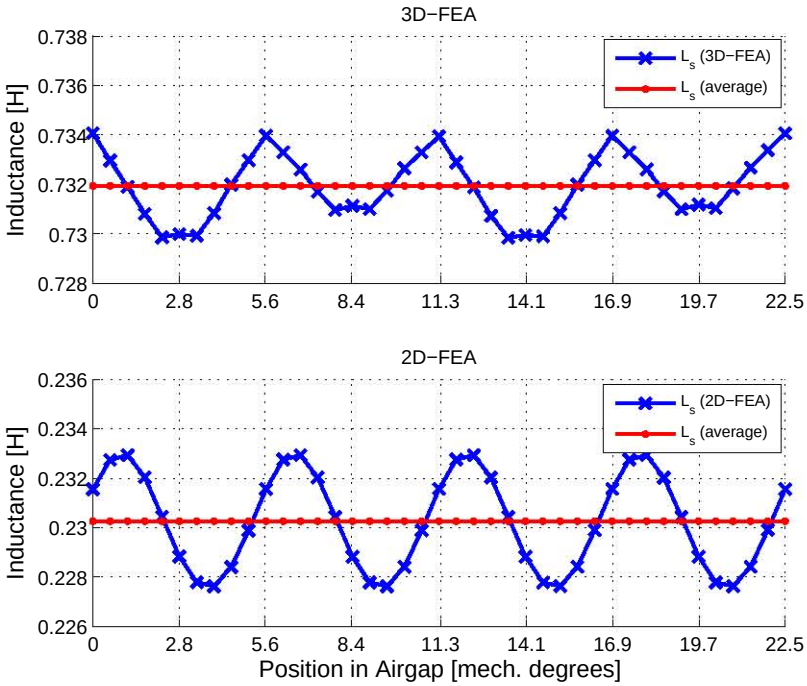

Figure 5.15: Winding inductance obtained with the 2D-FEA and 3D-FEA

5.6 Winding Inductance

For surface mounted PM machines the d-axis and q-axis inductances are equal to the synchronous inductance, since the relative permeability of air is approximately equal to that of the NdFeB PMs. The winding inductance can be considered as the incremental derivative of the flux linkage versus the varying current.

Using the 2D-FEA both magnetizing and leakage fluxes can be taken into account. However, the end winding inductance cannot be calculated, since the end windings are not incorporated in the 2D-model compared to the 3D-model. Thus, the 3D-FEA is capable of taking the end winding inductance into account. The winding inductance was simulated with both models and the results are shown in Fig. 5.15. The top graph in Fig. 5.15 shows the inductance calculated with the 3D-FEA and the inductance for the 2D-FEA is shown at the bottom. It can be seen that the inductance for the 3D-FEA is much higher than that of the 2D-FEA, with the average values for the 3D- and 2D-FEA being 732 μH and 230 μH respectively. The reason for the large discrepancy is due to the large end winding inductance, which is not accounted for in the 2D-FEA. The total length of the end windings per turn is 0.0756 m compared to that of the total active length of the stator windings of 0.03 m per turn.

The positive peak value in Fig. 5.15 corresponds to the q-axis inductance and the negative peak value to the d-axis inductance. The results show a very small difference between the d-axis and q-axis inductance, and can be attributed to the slightly larger magnetic relative

permeability assigned to the PMs, $\mu_{r,PM} = 1.0446$ than that of air, $\mu_r = 1$.

5.7 Influence of the PM Dimensions on the Performance of the Wave Winding

A machine built from identical PMs would need a large number of identical HDDs, since the dimensions of the magnets vary greatly between the types of HDDs found. This requirement would defeat the project's objective, since its scope is to design a generator, which can be built from a wide range of different types of magnet. Therefore, the influence of the PM dimensions on the performance of the generator was investigated by means of the FEA. The FEA will only be conducted in 2D, since the 2D-model has been verified by the 3D-model. The 2D-model assumes a cuboid for the PM shape as shown in Fig. 4.13. The dimensions for the cuboid are as follows: (a) The magnet width (b_p), which is equal to one pole pitch (τ_p), magnet height (h_M) and magnet depth, which is equal to the PM length in the radial direction (l_a). The magnet height and magnet depth will have similar effects on the back-EMF waveform, since both dimensions only reduce the flux per pole. Hence, only the magnet height and the magnet width will be varied in the analysis as illustrated in Fig. 5.16. The machine consists of only two kinds of magnets (a "normal" and a "changing" magnet) and thereafter repeats itself.

Three scenarios were simulated with reference to a machine with identical PMs, i.e.

1. Reduced PM height from 2.9 mm to 2.2 mm.
2. Reduced PM width from the normal pole pitch, $\tau_p = 19.19$ mm to 14 mm and
3. Increased PM width from the normal pole pitch, $\tau_p = 19.19$ mm to 22 mm.

The no-load back-EMF was calculated for one electrical cycle (= 11.25 electrical degrees) and the harmonics of the EMF were also determined. The results are shown in Fig. 5.17a and Fig. 5.17b. From Fig. 5.17a, it can be seen that the magnitude of the back-EMF waveform is only affected. The flux-density is directly influenced by the height of the magnet according to eqn (4.4), and consequently the *rms* value of the EMF is affected. Reducing or increasing the pole pitch changes the flux-density waveform in the airgap and the flux linking the coils will change as well. However, no visible deformation of the back-EMF waveform is noticeable in Fig. 5.17a. Even when analyzing the harmonic content of the EMF waveforms, no deterioration of

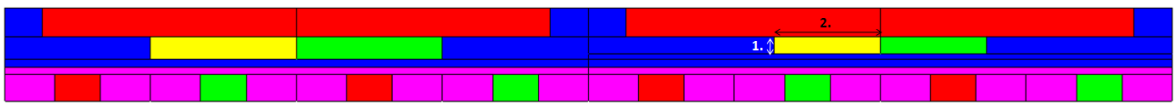

Figure 5.16: 2D-FEA model for analyzing the influence of PM dimensions on the performance of the wave winding; 1. variation of the PM height; 2. variation of the PM width

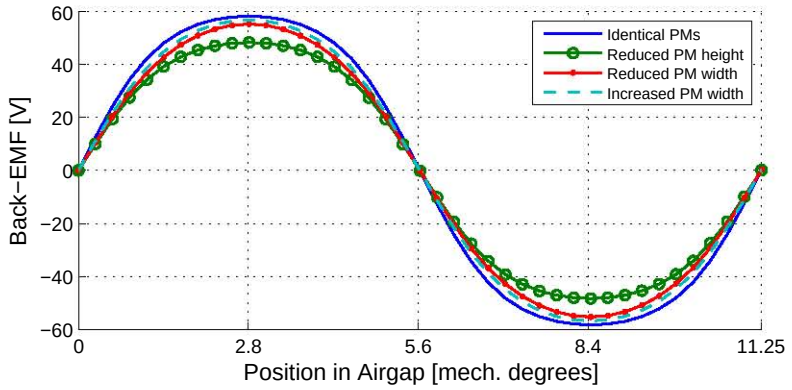

(a) No-load back-EMF waveforms

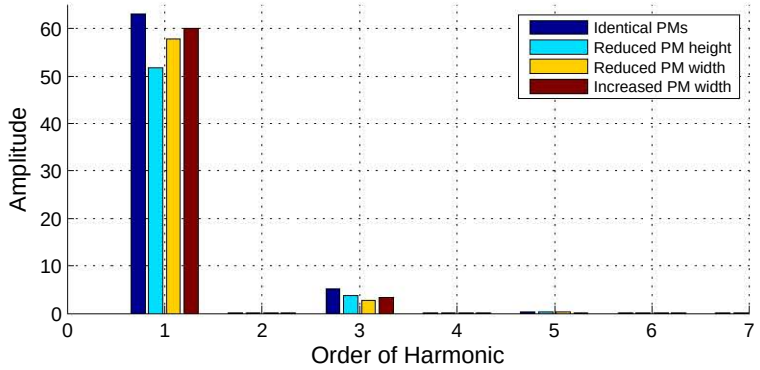

(b) Harmonics of the no-load back-EMF

Figure 5.17: Influence of magnet dimensions on back-EMF production

the output voltage of the machine can be seen. The values for the THD were computed to 7.3 %, 4.9 %, 5.8 % for the reduced PM height, reduced PM width and increased PM width respectively. These values are only slightly higher than that of the machine with identical PMs (= 4.85%).

The wave winding produces a symmetrical 3-phase output system for all simulated cases with a near sinusoidal waveform. It can therefore be concluded that the sustainable generator is only affected by different magnet shapes in terms of output power.

5.8 Conclusion

The performance of the sustainable generator was predicted with 2D-FEA and 3D-FEA and it was shown that the results from the 2D-FEA agreed well with the 3D-FEA, verifying the 2D-model. The *rms* values for the back-EMF, electromagnetic torque, eddy current losses and winding inductance were calculated for a shaft speed of 600 rpm and a phase current of

3.29 A and were found to be 33.13 V, 6.95 Nm, 9.1 W and 732 μH respectively. A method for accurately calculating the flux per pole for the non-sinusoidal flux-density distribution of the uncut HDD magnets was presented. It was found that the flux per pole is under-estimated by 16.3 %, when assuming a sinusoidal flux-density distribution. The influence of the thickness of the phase coils on the back-EMF production was furthermore investigated and it was found that the diameter of the coil should not exceed 6 mm. Finally, it was shown that the magnet dimensions only affected the output of the generator.

The following chapter will present the experimental results obtained from a 3-phase prototype, which are compared to the theoretical and numerical results.

Chapter 6

Prototyping and Testing of the Sustainable Generator

A 3-phase sustainable generator was prototyped to validate the machine topology. The generator was constructed as per the specifications in Table 5.1. Due to the peculiar "pancake-like" shape and the relatively large diameter of the sustainable generator, a new test rig for testing the generator needed to be designed and built. The design of the new test rig and the prototyping process are presented in this chapter. Finally, the generator is tested at different shaft speeds and loading points. The experimental results are discussed and compared with the theoretical and numerical results.

6.1 Design and Development of the 3 kW Servo Motor Test Rig

The test rig must be very versatile and needs to fulfill the following criteria:

1. Be able to accommodate and test a very wide range of machine shapes and sizes.
2. A very fine resolution for the torque transducer is required for measuring cogging torque of small PM machines.
3. The prime mover must be able to operate at the maximum torque of the torque transducer throughout the speed range of 2000 rpm.
4. The prime mover needs to be able to operate in three different operation modes, i.e.
    a) Speed control: The prime mover rotates the test machine at a desired speed (motoring mode).
    b) Torque control: The prime mover applies a desired torque to the shaft of the test machine (generating mode).

Table 6.1: Torque transducers specifications (DR-2112) [59]

Specification	Value
Rated torque [Nm]	10
Maximum torque (CRO) [Nm]	15
Limit Torque [Nm]	20
Accuracy class [%]	0.1
Active output signal [V]	±5
Sensitivity [V/Nm]	0.5
Sample Rate [kSample]	10

Figure 6.1: In-line torque transducer with rigid aluminum couplings

c) Position control: The prime mover steps the test machine at a required angle (operates as a stepper motor). A very fine stepping resolution is required for measuring cogging torque in PM machines.

The individual components of the test rig and their specifications are outlined in the next sub-sections.

6.1.1 Torque Transducer

Accurate torque measurements are vital for determining the performance of an electrical machine. The most common way to measure torque is with a load cell, which is by far the cheapest option. The prime mover is mounted on bearings, which allows it to move freely in the radial direction. The load cell is connected to one side of the machine and measures the torque applied to its shaft. This method is however not very accurate and has the inherent problem of varying the offset due to the stiffness of the entire structure. A brushless in-line torque transducer overcomes these challenges and can measure the torque very precisely, and was therefore chosen for the test rig. These sensors have a strain gauge glued to its shaft, which measures the torque applied to the shaft. The torque signal is transferred from the rotating shaft via a contactless technology. To mitigate or reduce the effect of misalignment on the torque readings, the transducer is connected to the prime mover and the test machine

Table 6.2: 3 kW servo motor specifications (ECMA-F11830PS) [60]

Specification	Value
Rated speed [rpm]	1500
Maximum speed [rpm]	3000
Rated torque [Nm]	19.1
Maximum torque [Nm]	57.29
Rated Current [A]	19.4
Maximum Current [A]	58.2
Torque constant [Nm/A]	0.98
Voltage constant [mV/rpm]	35
Encoder resolution [deg]	0.0036
Weight [kg]	18.5

via rigid couplings. The couplings allow for radial and axial misalignment without introducing unwanted vibrations.

The transducer needs to have an accuracy of at least 0.01 Nm in order to measure low cogging torque values of small PM machines, such as 0.15 Nm. A 10 Nm in-line torque transducer supplied by Lorenz-Messtechnik (DR-2112) met the requirements. It is shown in Fig. 6.1 and its specifications are given in Table 6.1.

6.1.2 Prime Mover

The main challenge in the selection of a prime mover is the fine stepping resolution required for measuring cogging torque. Stepping motors are capable of achieving the required resolution. However, they are not able to drive the test machine at a constant speed without introducing high torque ripple and cannot operate as a generator. Conventional induction machines, which have many poles and are driven by variable speed drives (VSDs) were also considered, but do not fulfill the stepping resolution requirement and are difficult to control in generator mode. DC and PMDC machines can easily be driven as a motor or generator, but do not meet the stepping resolution requirement.

AC servo motors on the other hand, seem to fulfill all the requirements and are wildly used in the automation and precision industry. For example, the automobile manufacturing industry makes extensive use of these servo motors, where they are mainly found in the arms of the robots. These motors have a very high stepping resolution, have high rated output power of up to 95 kW [61] and can easily be operated as a motor or generator. Hence, an AC servo motor was chosen as the prime mover. Since the maximum torque of the torque transducer is 15 Nm, the required rated power can be calculated as

$$P = T\,\omega = 15 \cdot \frac{2\pi 2000}{60} = 3142\ \text{W} \tag{6.1}$$

A 3 kW servo motor was chosen, since the next available rating was 4.5 kW, which was larger is size and much more expensive. The servo motor was kindly supplied and sponsored by Delta Electronics Inc., Taiwan in cooperation with Electromechanica, South Africa. The servo motor has a stepping resolution of 0.0036°, which is equivalent to 100 000 impulses per revolution. Its specifications are given in Table 6.2. The 3 kW servo motor is driven by a 3 kW servo drive and is interfaced by means of a touch panel. A program was developed, which operates the servo motor in the three required operation modes.

6.1.3 Mechanical Structure

The servo motor, torque transducer and test machine were bolted onto a test bed with T-slots. The test machine holding structure can accommodate different shapes and sizes of test machines. Fig. 6.2a shows a 3D-CAD model of the test rig without a mounted test machine. In Fig. 6.2b a machine of conventional shape is mounted onto the test rig, thereby proving its functionality. In order to mount the "pancake-like" sustainable generator, the test rig was modified as shown in Fig. 6.3. The rotor structure of the generator is fixed to the shaft by means of an extension plate which forms part of the shaft and the stator structure is held in place by the square plate as shown in Fig. 6.3b. A 3D-CAD model of the final test rig is shown in Fig. 6.3a.

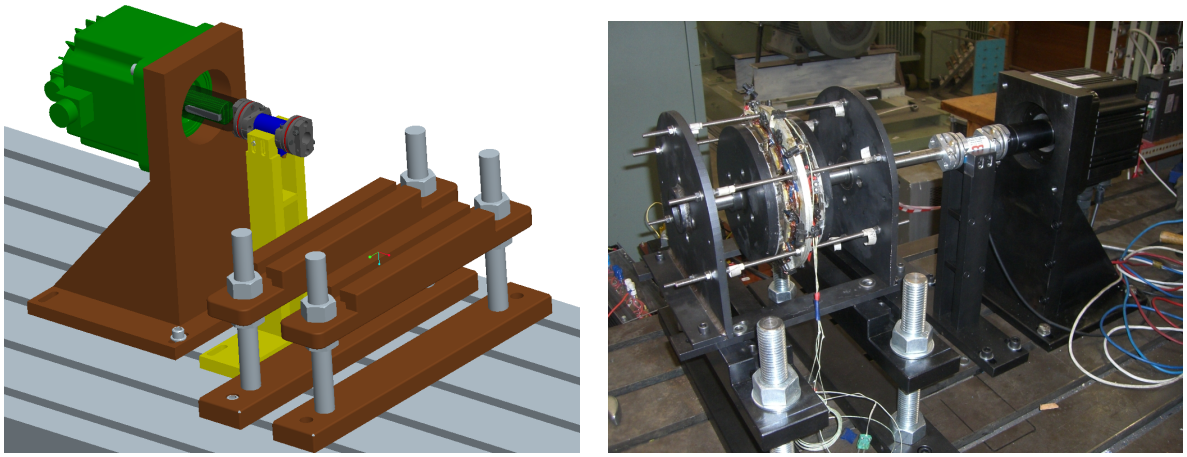

(a) 3D-CAD model of test rig without a test machine

(b) Test rig mounted with a machine of conventional shape

Figure 6.2: Test rig for testing various conventional machine shapes and sizes

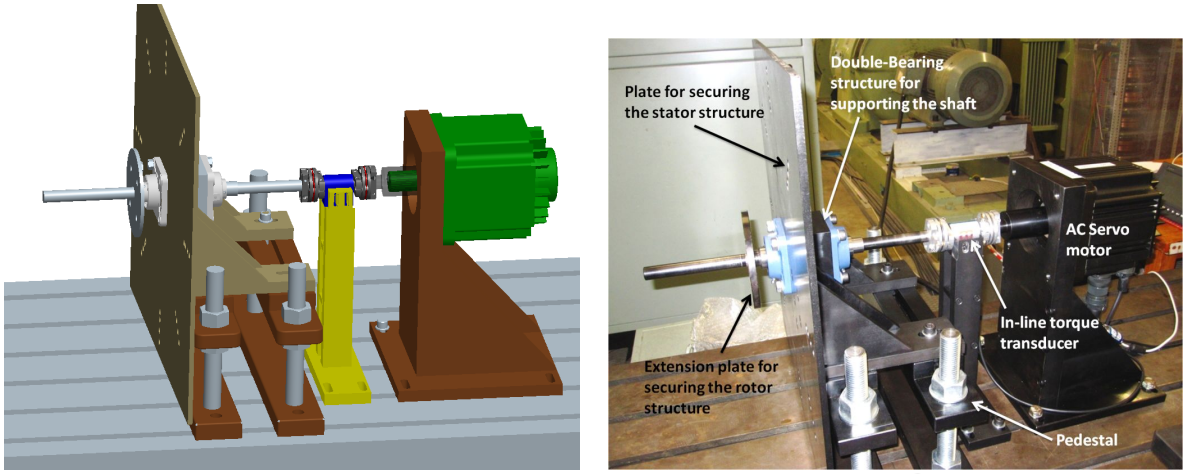

(a) 3D-CAD model of final test rig **(b)** Final test rig

Figure 6.3: Test rig for testing "pancake-like" machines

Structural FEA of the Test Rig

The mechanical structure must withstand the structural forces of the system and a structural FEA was therefore conducted to ensure mechanical integrity of the entire system.

The entire test rig structure was manufactured using mild steel. Each individual component, i.e. the servo motor stand, torque transducer stand, pedestal and the rig for holding the sustainable generator, was simulated in the structural FEA package from Ansys. A linear static problem was defined for each component of the test rig. Standard gravitational acceleration and a moment of 30 Nm (absolute maximum torque of transducer) was applied to the test rig. The total deformation and equivalent stress (von-Mises) for the servo motor stand is shown in Fig. 6.4. Its maximum deformation was computed to 6.4 μm and the maximum stress was 7.4 MPa. To accommodate different machine shapes and sizes, the complete rig was over-designed to ensure that the stresses do not exceed the maximum allowable stress of 220 MPa of mild steel.

Another concern regarding the structural integrity of the test rig was related with the unconventional shaft structure used. The shaft is supported at its center by a double bearing structure as shown in Fig. 6.3b. The shaft ends are extended by 0.16 m from the bearings, which could cause excessive vibrations. Additionally, the deflection of the shaft might exceed the tolerances of the couplings. In order to ensure safe operation, a structural FEA was conducted for the shaft structure with two rotor structures secured to it. The worst case scenario, with the rotor structures being made of mild steel, was assumed. The shaft was supported by two frictionless supports (bearing faces), standard gravitational acceleration and a rotational speed of 2000 rpm were defined. The simulation results are shown in Fig. 6.5. The shaft end coupled to the transducer shows a deflection of only 1.6 μm, which is far

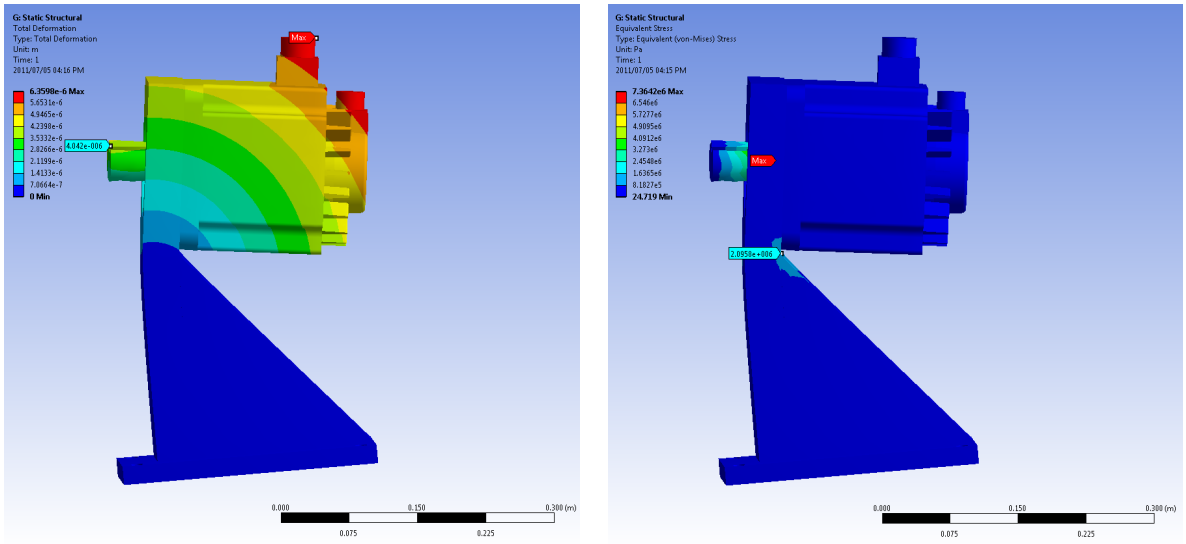

(a) Total deformation **(b)** Equivalent stress (von-Mises)

Figure 6.4: Simulation results for the servo motor stand

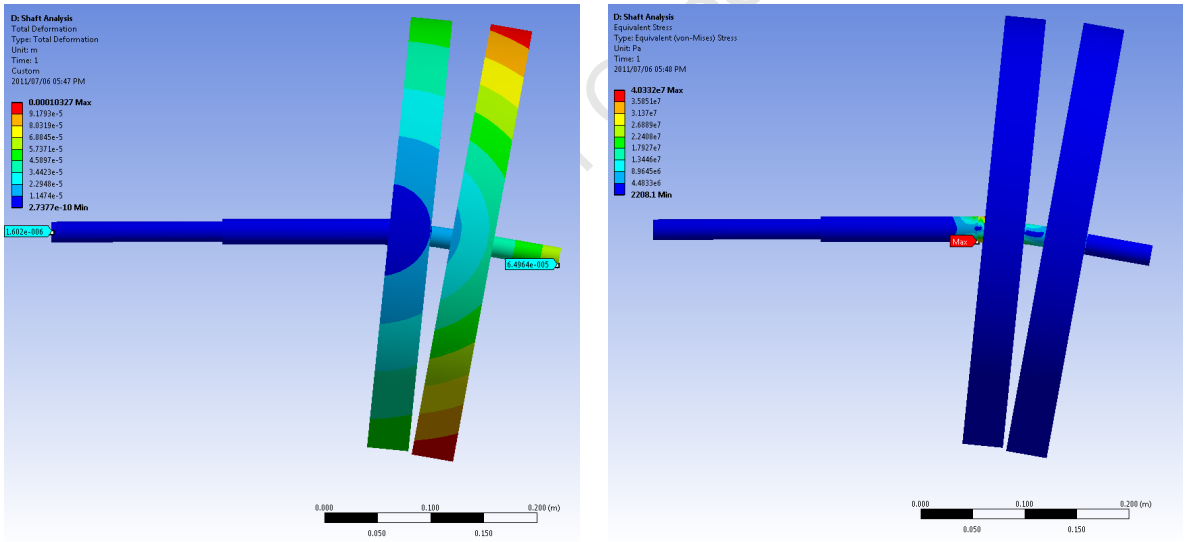

(a) Total deformation **(b)** Equivalent stress (von-Mises)

Figure 6.5: Simulation results for shaft structure

below the tolerance of 0.1 mm. The shaft end with the two solid mild steel rotor structures secured to it shows a deflection of 65 μm. The maximum equivalent stress was computed to 40 MPa and is clearly below the tensile yield strength of 220 MPa for mild steel.

6.2 Prototyping of the Sustainable Generator

This section presents the prototyping of the sustainable wind generator. The prototyping procedures of the rotor and stator structures are outlined and the cost break-down of the generator are further presented. Finally, the test set-up with which the experimental results were obtained is described.

6.2.1 Rotor Structure

The HDD magnets should be mounted on a relatively cheap, but robust rotor structure, since the goal is to use low cost and readily available materials. The rotor structure is not required to be ferromagnetic, since the HDD PMs are used with their backing plates. This allows far cheaper materials than mild steel to be utilized. Perspex and medium density fiberboard (MDF) are suitable options, because they are readily available, relatively cheap and have good mechanical properties, which will ensure mechanical integrity of the machine. To find the suitable thickness of the rotor disc, which satisfies the critical strength requirements of the rotor structure, a linear FEA static analysis was performed for different thicknesses for both Perspex and MDF rotor structures. The attraction force between the two parallel rotor discs was calculated using the virtual work method as described in [15]. Only one HDD magnet needed to be modeled due to the periodicity of the machine. The force acting on one HDD magnet was found to be 23.6 N. The mechanical properties of the materials used in the simulation are given in Table 6.3. It was found that for both Perspex and MDF, the rotors are required to have a minimal thickness of 6 mm. Perspex of 6 mm thickness was found to be roughly 11 times more expensive than MDF (Price for Perspex: R $505.5/m^2$ and MDF: R $47.3/m^2$ [62][63]). Moreover, MDF presents a more environmental friendly and sustainable solution since it is usually manufactured from quick growing pine woodlands. In addition, MDF can be manufactured from renewable agricultural residues, such as hazelnut husk or canola straw [64][65]. Other sources for MDF production are waste paper, waste wood and bamboo [66]. Therefore, MDF was chosen for the rotor structure.

Fig. 6.6 shows the simulation results for the 6 mm MDF rotor structure. As expected, the maximum deflection occurs at the far end of the rotor structure and is 0.25 mm. This deflection is within the limits of the design, since the total reduction of the airgap will be 0.5 mm. The maximum equivalent stress for the MDF rotor structure occurs just above the rotor spacer and is 2.11 MPa, which is far below the minimal tensile yield strength of 20 MPa for MDF.

The outer radius of the rotors and the number of poles of the sustainable generator were calculated in sub-section 4.3.7 and were found to be 0.203 m and 64 respectively. In order to realize 64 poles, 16 uncut HDD magnets are needed per rotor disc. These magnets were bolted onto each rotor disc, ensuring that the distance between each magnet is exactly two

Table 6.3: Mechanical properties for materials used in the FEA [67][68]

Specification	Perspex	MDF	Mild Steel
Young's Modulus [GPa]	2.3	3	200
Poisson Ratio	0.4	0.25	0.303
Tensile Yield Strength [MPa]	40-70	20-80	220
Density [kg/m^3]	1190	795	7850

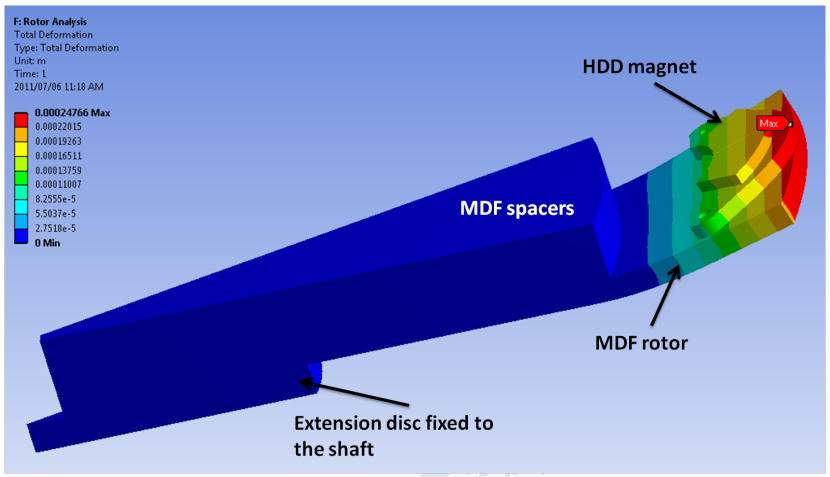

(a) Total deformation

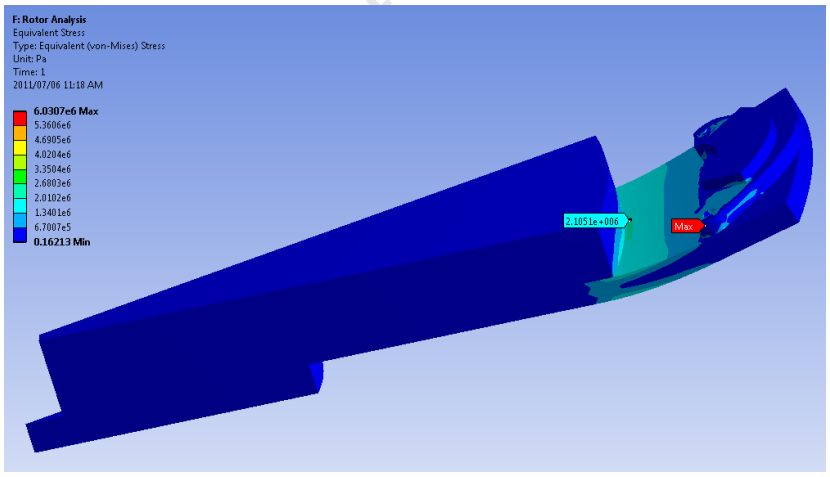

(b) Equivalent stress (von-Mises)

Figure 6.6: Simulation results for the rotor structure using 6 mm MDF

pole pitches, i.e. two "imaginary poles" as illustrated in Fig. 6.7. A 3D-CAD model of a rotor disc and a prototyped MDF rotor disc are shown in Fig. 6.8.

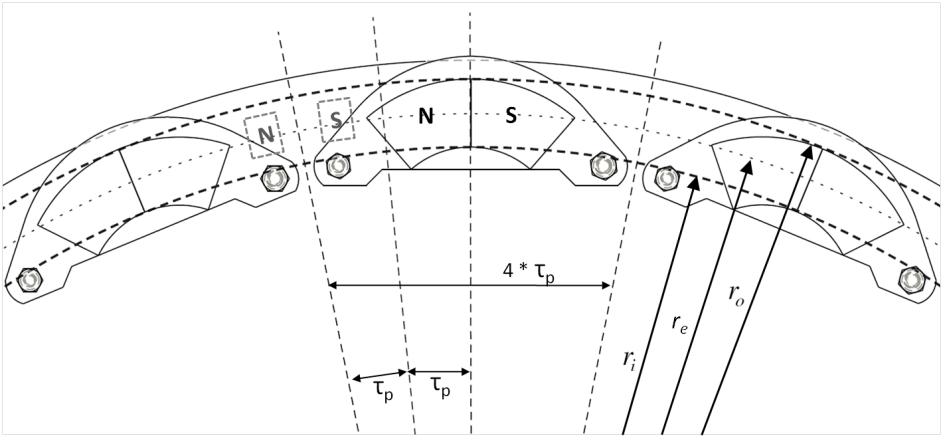

Figure 6.7: Positioning of the uncut HDD PMs along the perimeter of the rotor disc

(a) 3D-CAD model of rotor disc **(b)** Prototyped MDF rotor disc

Figure 6.8: Rotor disc with sixteen uncut HDD magnets bolted to it

6.2.2 Stator Structure

Coreless stator structures are the cheapest and easiest to manufacture, due to the absence of a ferromagnetic stator core and the simplicity of the manufacturing process. The stator windings are usually encased in an epoxy resin structure. For the prototype, Ampreg AP21 resin and 0.7 mm winding wire of insulation class 2F was used. 22 turns were wound around a mold as illustrated in Fig. 6.9a, in order to ensure a symmetrical winding structure for all phases. Three wave windings were formed in this manner and the end windings twisted to allow for overlapping between the phases as shown in Fig. 5.2 and Fig. 6.9b. The main drawback associated with a coreless stator is the large effective airgap introduced in the

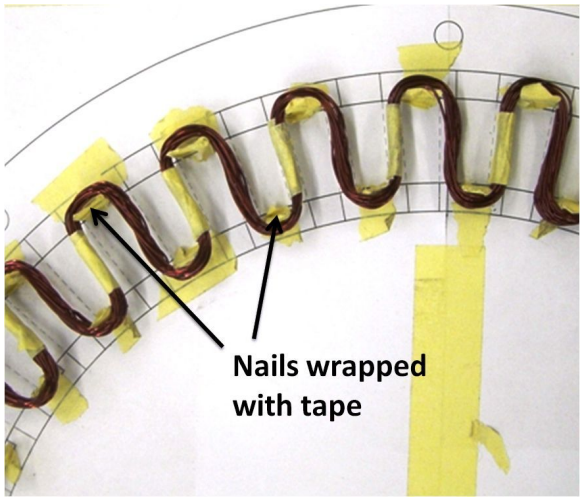

(a) Mold for winding the wave winding

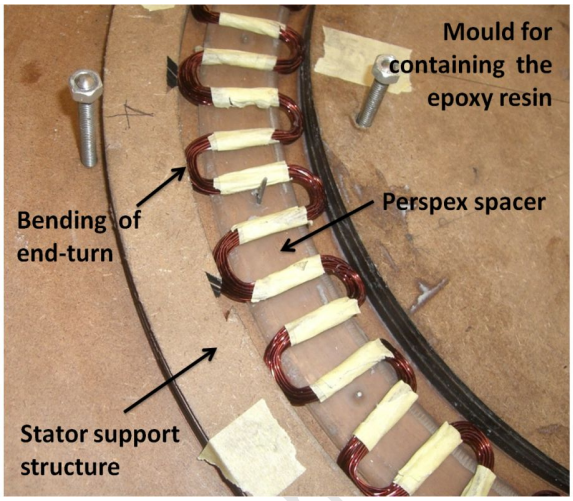

(b) Stator mold for containing the epoxy resin and creating the groove for the magnets

Figure 6.9: Molds for prototyping of the stator structure

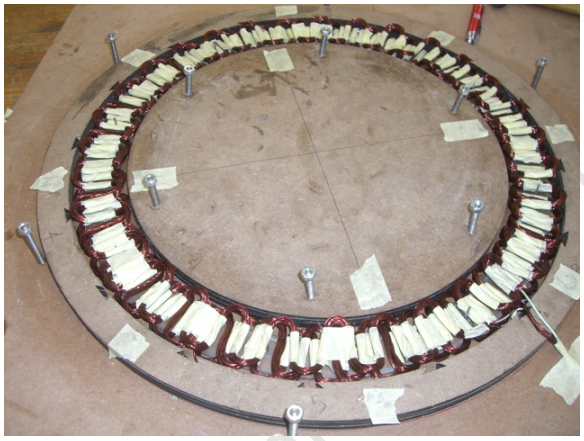

(a) Before pouring epoxy resin

(b) Complete 3-phase stator with groove

Figure 6.10: 3-phase wave winding stator structure

machine, due to the absence of a ferromagnetic stator core. Consequently, the airgap of the sustainable generator should be kept as small as possible, because of the fixed shape and energy product of HDD magnets compared to that of magnets that are customized for a particular machine design. For this reason, the stator was designed with a groove in which the magnets can rotate, which minimizes the effective airgap. The mold is shown in Fig. 6.9b. Fig. 6.10 shows the complete stator structure before and after pouring of epoxy resin.

In order to determine the friction and windage losses, a dummy stator is necessary, which needs to be identical to the coreless stator. The dummy stator was built from MDF and is shown in Fig. 6.11.

Figure 6.11: Dummy stator for measuring friction and windage losses

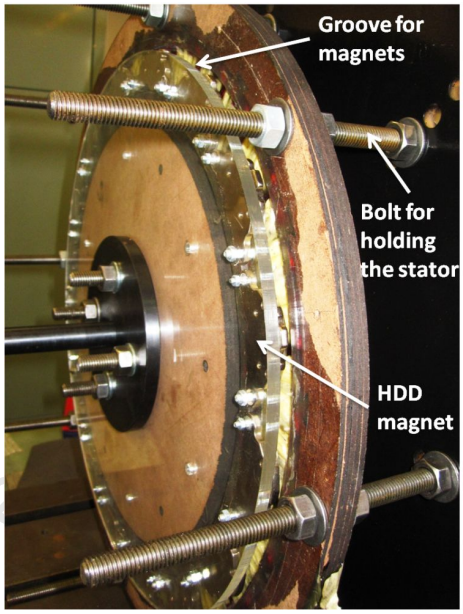

Figure 6.12: Complete generator assembly

6.2.3 Assembled Generator

The two rotor discs are kept apart by a MDF spacer as shown in Fig. 6.6a. A spacer thickness of 24 mm is required to realize an effective airgap of 10 mm. The rotor structure was bolted to the extension plate of the shaft and the stator structure was held in place with eight threaded M12 rods, which were secured to the square plate as shown in Fig. 6.3. The airgap was carefully adjusted until the magnets could rotate freely and the stator was at the center of the opposing magnets. The complete generator assembly is shown in Fig. 6.12.

Table 6.4: Cost break-down of prototyped generator

Part	**Cost [ZAR]**
Copper wire (0.7 mm, 220°C, 2F)	89
Epoxy Resin (Ampreg 21 Resin)	66.9
MDF (6mm)	36
MDF (3mm)	25.6
HDD magnets	26
Total	**243.5**

6.2.4 Cost of Generator

In addition to the sustainability of the generator, the total cost is regarded as a crucial factor in the design process. The materials for the components were carefully chosen with most materials being either cheap, readily available or recycled. The PMs for the rotor discs were taken from discarded HDDs, which were sourced from various places, such as electronic scrap yards, recycling warehouses and the Information Technology (IT) department of the University of Cape Town. The copper wire for the windings could not be sourced from used components, since the winding wire of electrical equipments is generally encased in an epoxy resin structure. The epoxy resin for securing the stator windings cannot be recycled or reused either. The MDF for the rotor discs, rotor spacers and stator frame can be manufactured from off-cuts. However, off-cuts with the required dimensions could not be sourced. Thus, the copper wire, the epoxy resin and the MDF were bought from commercial retailers. In addition, all other miscellaneous parts, i.e. bolts, screws and nuts, were obtained from a hardware shop. The cost break-down is given in Table 6.4.

Figure 6.13: Test set-up; (1) 3 kW servo motor; (2) 3 kW drive for servo motor; (3) touch panel for controlling the servo motor; (4) 10 Nm in-line torque transducer; (5) rig for holding generator; (6) power analyzer; (7) resistor bank

6.2.5 Test Set-Up

The generator was tested using the test set-up shown in Fig. 6.13. The 3 kW servo motor was used to drive the generator. The servo motor was run in speed control mode and the speed was displayed by the touch panel. The in-line torque transducer measured the shaft torque of the generator and a software provided by Lorenz was used to display and record the torque values. The machine was loaded using a 3-phase resistor bank. Different loading points were obtained by switching combinations of 10 Ω resistors in series or parallel. A WT 1600 Yokagawa power analyzer was used to acquire the current, voltage and power readings.

6.3 Discussion of Results

This section presents the results obtained from the prototype and compares them with the results obtained from the theoretical and numerical analyses. The sustainable generator was tested at four different shaft speeds, i.e. 100 rpm, 250 rpm, 400 rpm and 600 rpm. The back-EMF and no-load losses were obtained from the no-load test. From the load test, the output power, efficiency and losses due to the loading of the machine were obtained.

6.3.1 Back - EMF

The measured waveforms of the experimental generator for the no-load phase back-EMF, the phase voltage and the phase current are shown in Fig. 6.14. From Fig. 6.14, it can be seen that the machine output is balanced in magnitude and in phase.

The back-EMF versus the rotational speed plot is shown in Fig. 6.15. The theoretical and FEA results agree well with the experimental result. This can be attributed to the choice of magnet grade in the theoretical and numerical analyses, since the magnet grade of the HDD magnets is unknown. The per-phase back-EMF of the prototype was analyzed using a power analyzer and the harmonics were acquired. At 600 rpm, the total harmonic distortion (THD) is 4.85 % and the third harmonic has a *rms* value of 2.185 V, which is 4.84 % of the fundamental of 45.18 V. It was found that the THD was relatively constant for varying speeds and loading points. A bar chart, showing the harmonics for the 2D-FEA, 3D-FEA and the prototype was presented in Fig. 5.10 in chapter 5.

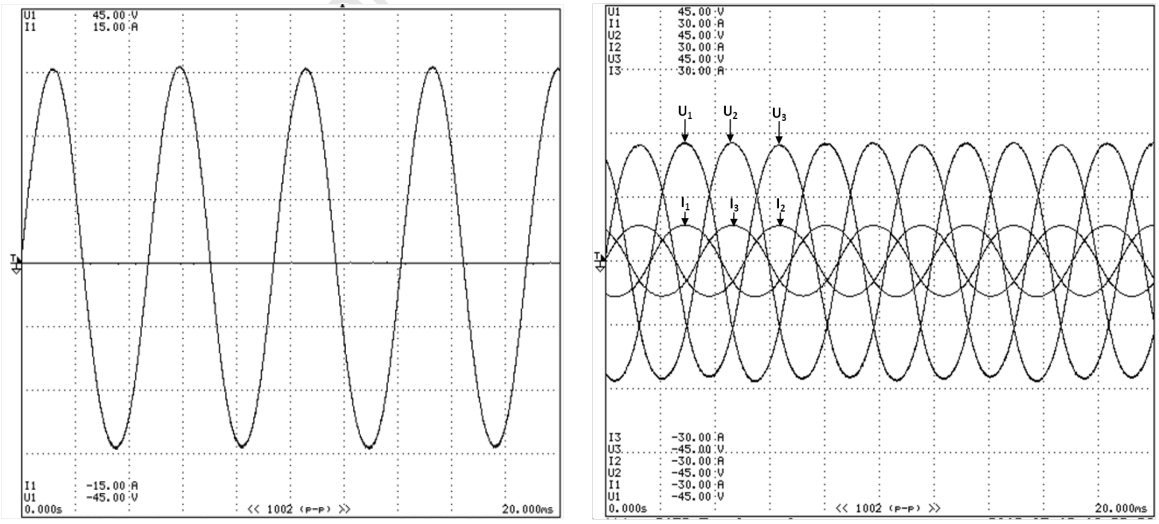

(a) Phase no-load back-EMF **(b)** Phase voltage and current

Figure 6.14: Measured output waveforms for the prototype

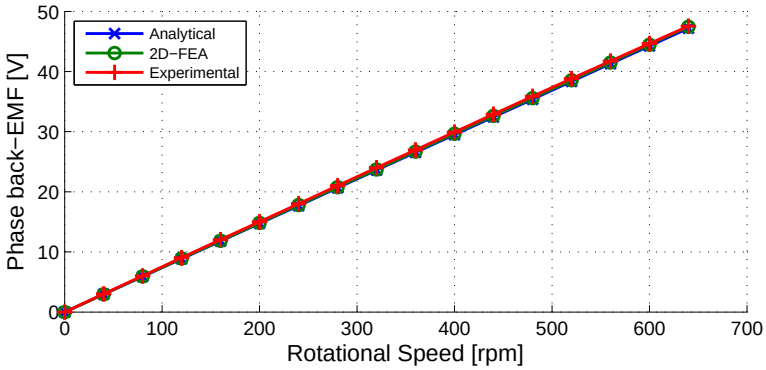

Figure 6.15: Back EMF vs rotational speed plot

The PM flux linkage (ψ_{PM}) can be calculated from the slope of the back-EMF versus speed characteristic of the machine according to eqn (6.2). The results for the three methods are given in Table 6.5.

$$E_f = \omega_e \psi_{PM} \tag{6.2}$$

where ω_e is the electrical angular speed of the machine in radians per second.

6.3.2 No - Load Losses

Friction and windage losses can be determined experimentally by means of a dummy stator in place, which is identical to the coreless stator structure but contains no conductors, and is shown in Fig. 6.11. With the actual stator in situ, the total no-load losses can then be determined. Subtracting the friction and windage losses from the no-load losses gives the eddy current losses induced in the stator windings [15].

6.3.2.1 Friction and Windage Losses

The theoretical and experimental friction windage losses are shown in Fig. 6.16a. From Fig. 6.16a it can be seen that the theoretical analysis over-estimates the friction and windage losses at low speeds, with the maximum deviation of 39.6 % occurring at 200 rpm. However, the losses are under-estimated for shaft speeds above 450 rpm, with a deviation of 16.2 % occurring at 640 rpm. Note that a k_{fb} of 4 is used in eqn (4.46) for the theoretical calculation of friction losses, since the deep groove roller bearings have a relatively high frictional coefficient. However, from Fig. 6.16a, it can be deduced that the friction losses are rather over-estimated and the windage losses under-estimated. The higher windage losses can be attributed to the fanning effect of the PMs rotating in the groove of the stator. Hence, the theoretical friction and windage losses were improved and are shown in Fig. 6.16b.

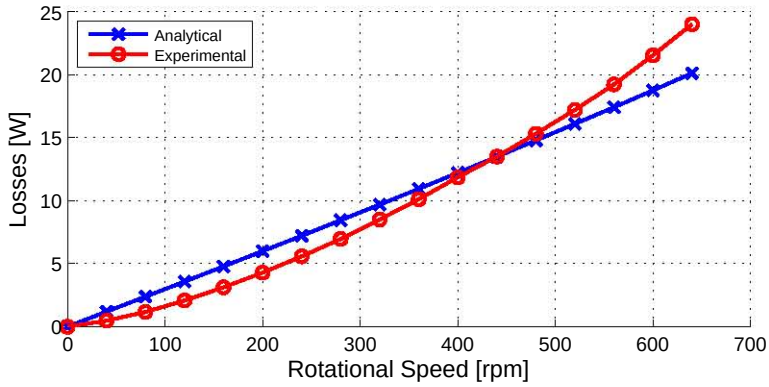

(a) Original $P_{f\&w}$ estimation, with $k_{fb} = 4$

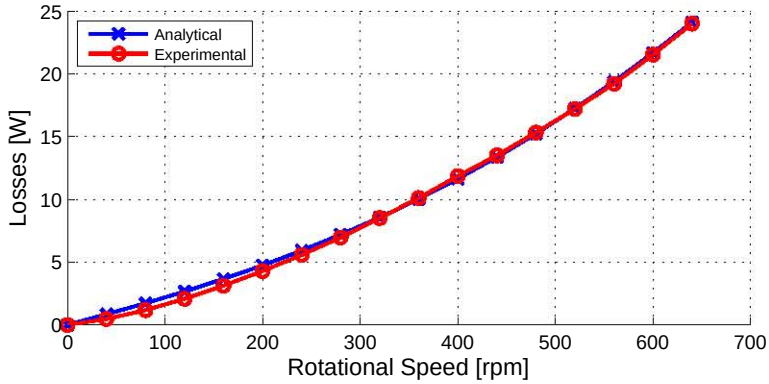

(b) Improved $P_{f\&w}$ estimation, with increased windage loss component and reduced friction loss component

Figure 6.16: Comparison of friction and windage losses

6.3.2.2 Eddy Current Losses

The eddy current losses determined with the three methods are shown in Fig. 6.17. Both methods, the theoretical and the numerical analysis, produce accurate results for the eddy current losses. To account for the non-sinusoidal flux-density distribution of the uncut HDD magnets in the theoretical analysis, the harmonic components for the flux-density were obtained from the 2D-FEA and inserted into eqn (4.43).

Fig. 6.18 shows the separation of the no-load losses into eddy current losses and friction and windage losses for the prototype.

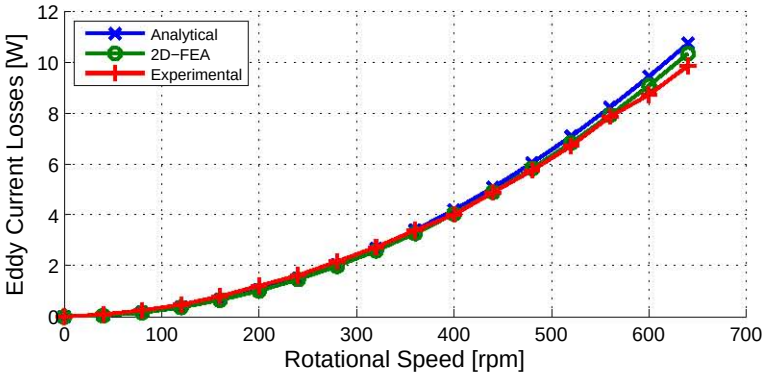

Figure 6.17: Comparison of eddy current losses

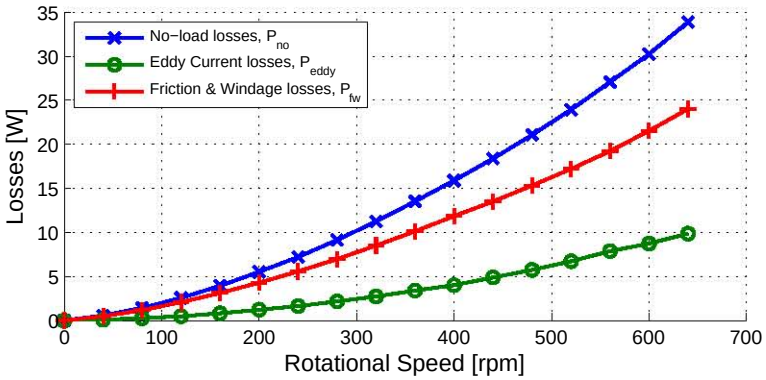

Figure 6.18: No-load, eddy current and friction and windage losses for the prototype

6.3.3 Voltage Regulation

Fig. 6.19 shows the per phase voltage regulation of the machine for a purely resistive load at different shaft speeds. The voltage regulations ($\epsilon = E_f/V_a$) at 3.3 A and 600 rpm, 2.7 A and 400 rpm, 2.2 A and 250 rpm, and 1.1 A and 100 rpm, are 1.34, 1.47, 1.68 and 2.03 respectively. The latter values depict a poor voltage regulation for the generator and can be attributed to the relatively high phase winding resistance of 3.33 Ω. The gradient of the terminal voltage characteristic in Fig. 6.19 is approximately 3.4 volt per ampere for all four speeds.

6.3.4 Winding Resistance and Inductance

The per phase winding resistance and inductance were measured using an LCR-meter, and the average per phase values for the resistance and inductance were found to be 3.33 Ω and 834 μH respectively. These values agree well with the theoretical estimation of the phase resistance and inductance of 3.48 Ω and 901 μH respectively. The resistance for all three phase windings were found to be approximately equal to each other, i.e. 3.33 Ω, 3.31 Ω and 3.36 Ω for phase A, B and C respectively. This proves the effectiveness of the winding technique,

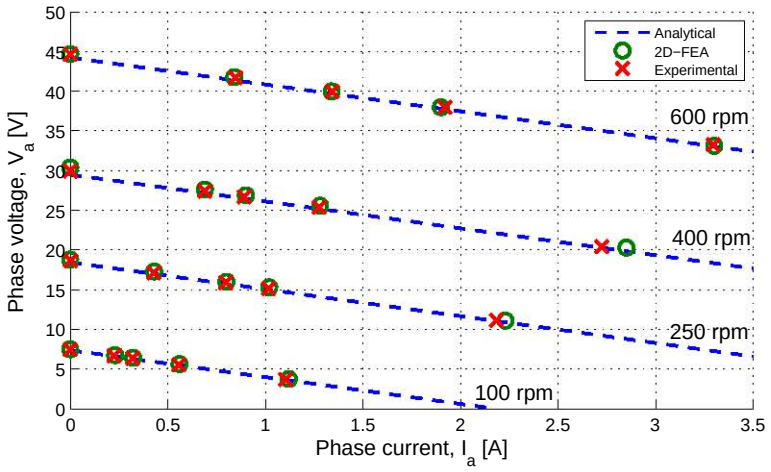

Figure 6.19: Voltage regulation at difference shaft speeds

which was used to wind the wave winding. The individual components for the theoretical estimation of the winding inductance were computed to 218 μH, 175 μH, 50 μH and 458 μH for the armature reaction, slot leakage, differential and end winding inductance respectively. The winding inductance obtained from the 3D-FEA was 732 μH, which is lower than the theoretical and measured inductance.

6.3.5 Efficiency

The efficiency of the generator was calculated analytically by computing all losses and using eqn (4.53). For the prototype, the efficiency was obtained as the ratio of the measured input shaft power ($P_{sh} = T\omega_m$) to the measured output power ($P_{out} = 3V_a I_a \cos\phi$). The generator operated with unity power factor since a purely resistive load was used. Fig. 6.20a shows a comparison of the analytical and experimental efficiencies at different shaft speeds and various loading points. The efficiency for the prototype peaks at 77.41 % at a phase current of 1.34 A and a shaft speed of 600 rpm. The efficiency of the generator drops as the load increases and is due to the excessive copper losses with increasing load. The efficiency furthermore decreases with speed, and reaches 46.46 % at a phase current of 1.12 A and a shaft speed of 100 rpm. This can be attributed to the decreasing terminal voltage with decreasing speed. Also, a bigger drop in efficiency occurs with increasing load at low speeds and is due to the large voltage drop across the stator winding resistance relative to the induced no-load back-EMF. From Fig. 6.20a, the greater discrepancy between the analytical and experimental efficiencies at low speeds is clearly visible. As already mentioned, the analytical analysis over-estimates the friction and windage losses at low speeds as shown in Fig. 6.16b.With the theoretical analysis improved, the analytical efficiencies agree well with the experimental efficiencies as shown in Fig. 6.20b.

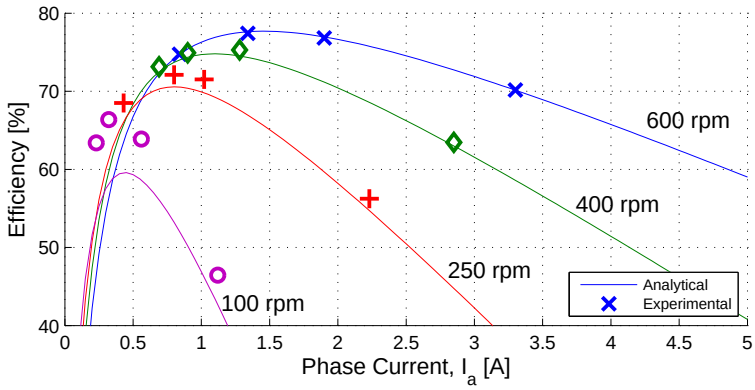

(a) Original $P_{f\&w}$ estimation

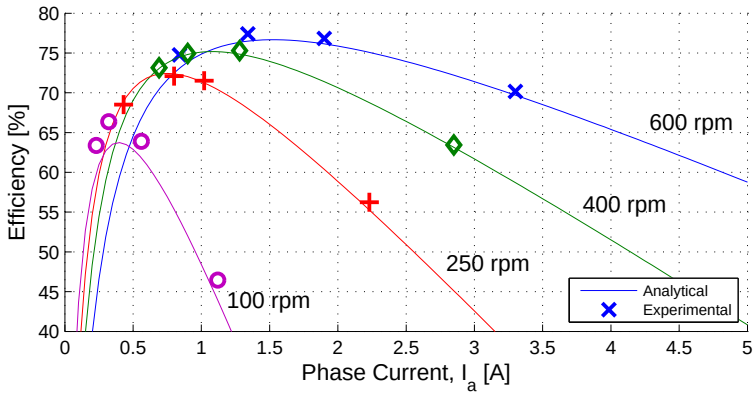

(b) Improved $P_{f\&w}$ estimation

Figure 6.20: Efficiency of generator at different shaft speeds for various loading points

6.3.6 Electrical Output Power

Fig. 6.21 shows the electrical output power of the generator for the four shaft speeds at various loading points. At 600 rpm and a phase current of 3.3 A, the experimental generator has an output power of 328 W, whereas at 100 rpm and a phase current of 1.12 A, the generator produces 12.6 W of electrical power only.

Table 6.5 compares the generator performance calculated with the different methods at a single operating point, i.e. at a shaft speed of 600 rpm and a phase current of 3.3 A. It can be seen that the theoretical and 2D-FEA predict the generator performance well. For low speed machines, copper losses is the most dominant loss component [69], which is also the case for the experimental generator, where the copper losses are 33.3 % of the output power.

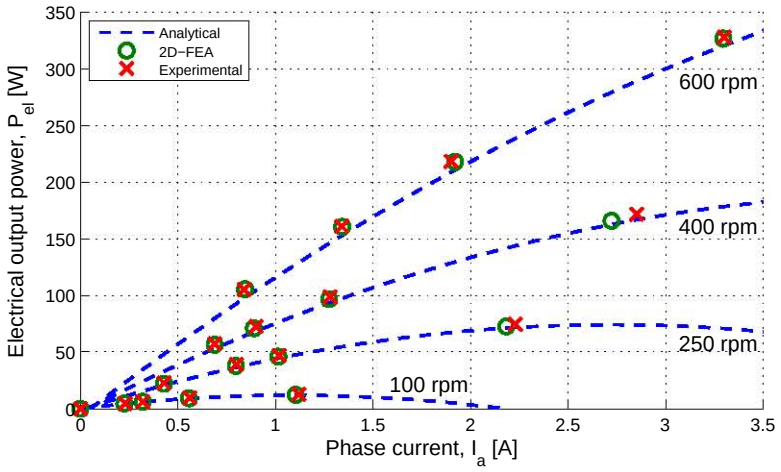

Figure 6.21: Electrical output power for different speeds and loading points

Table 6.5: Machine Performance at 600 rpm

Specification	**Analytical**	**2D-FEA**	**Experiment**
Shaft speed, n [rpm]			600
Effective airgap, g [mm]	10	10	10.2
Average length of turn, l_{avg} [m]	0.108	-	0.106
Per phase resistance, R_{dc} [Ω]	3.48	3.4	3.33
Per phase inductance, L_s [μH]	901	732 (3D-FEA)	834
Airgap flux-density, B_{mg} [T]	0.403	0.415	$\sim$0.405
Flux linkage, ψ [Wb-turns]	0.022	0.0221	0.0222
EMF, E_f [V]	44.25	44.68	44.7
Phase current, I_{an} [A]	3.3	3.29	3.3
Phase voltage, V_{an} [V]	33.1	33.13	33.2
Copper losses, ΔP_{cu} [W]	113.6	109.8	109.2
Rotational losses, ΔP_{rot} [W]	17.8	-	21.5
Eddy current losses, $\Delta P_{e,w}$ [W]	9.43	9.1	8.7
Electrical output power, P_{el} [W]	315	327	328
Efficiency [%]	69.1	71.84	70.2

6.3.7 Temperature Responds

The winding and epoxy temperatures were measured with thermocouples secured on the phase windings and the epoxy resin. The temperature responses for three different operating points are shown in Fig. 6.22. The temperature difference between the windings and the epoxy is small, which indicates that the entire stator structure heats up equally. The windings are encased in epoxy resin and the stator structure support is made from MDF. Both materials have weak thermal conductivity characteristics and therefore act as insulators. For a load current of 1.3 A and a shaft speed of 400 rpm, the temperature stabilized after 50 min,

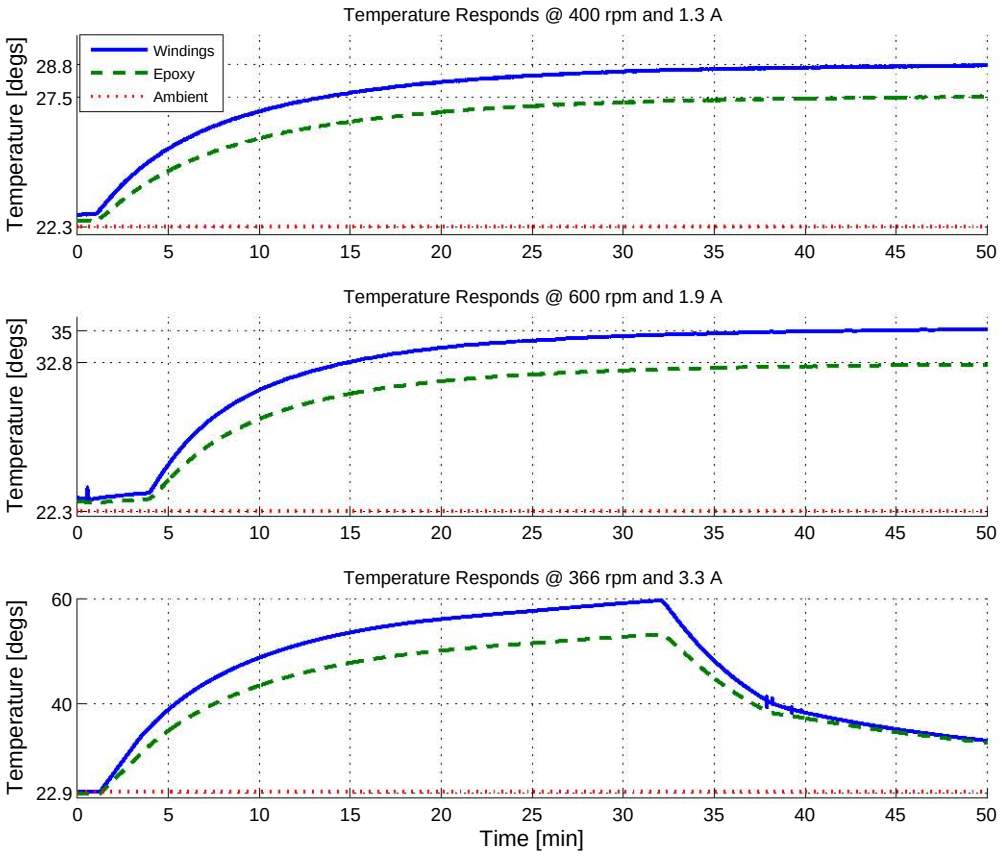

Figure 6.22: Temperature responds of generator at different operation points

reaching a maximum of 28.8°C at the windings, whereas the winding temperature reached 35°C for a load current of 1.9 A at 600 rpm. When the generator was loaded with a phase current of 3.3 A and operated at 366 rpm, the temperature reached 60°C, before the load was disconnected due to safely requirements.

6.4 Conclusion

A new test rig for testing large disc PM motors was presented and it was shown that the rig met all requirements and performed well. The prototyping process, together with the manufacturing techniques used to build the sustainable generator, was discussed. It was shown that by winding the wave winding around the developed mold, a symmetrical shape for the wave winding was achieved, which resulted in a similar per phase resistance.

The performance of the machine as predicted analytically and through FEA were found to correlate well with the experimental results of the prototyped machine. The wave winding

produced a near perfect sinusoidal and balanced 3-phase output despite the non-uniform airgap flux-density distribution. The total harmonic distortion of the back-EMF at a shaft speed of 600 rpm was 4.85 %. At a shaft speed of 600 rpm and a phase current of 3.3 A, the generator produced 328 W of electrical power. At this operation point, the phase voltage dropped by 25.7 % to 33.2 V, highlighting the poor voltage regulation of the generator. This can be attributed to the relatively high phase winding resistance of 3.33 Ω associated with overlapping windings. The efficiency of the generator at this specific loading point was 70.2 %, which is acceptable for small machines. The temperature responses of the machine were recorded for different operation points. Since the epoxy resin and the MDF stator structure have low thermal properties, the machine should be carefully loaded in order to ensure thermal integrity of the machine.

Chapter 7

Conclusions and Recommendations

The conclusions and recommendations drawn from the sizing of the sustainable wind energy capture and storage system and the design and analysis of a sustainable wind generator are presented in this chapter.

7.1 Conclusions

The following conclusions are drawn from the work presented in this dissertation.

7.1.1 Sizing of a Sustainable Wind Energy Capture and Storage System

A topology for a sustainable wind energy capture and storage system was presented and a sizing methodology for the individual system components was developed. It was found that materials sourced from e-waste are available, and can be used for the proposed sustainable topology. It was shown that 11.4 Wh of electrical energy can be stored in a sustainable flywheel and 277 W of electrical power can be generated by the sustainable generator at a rated wind speed of 8 m/s. The wind turbine was selected to have a wide operating wind speed range, i.e. from 2.5 - 8 m/s, which guarantees maximum supply of power to a rural household. It was furthermore shown that the wind energy system is capable of powering the basic electrical appliances of a rural household, such as lighting, radio- and telecommunication. In the event that no wind blows, the flywheel can supply the maximum power demand of 14 W to the household for up to 12 min. Nevertheless, with wind blowing at very low speeds ($>$ 2.5 m/s), the system is capable of supplying the household continuously with power.

7.1.2 Proposed Topology for the Sustainable Wind Generator

The most suitable topology for a sustainable wind generator was reviewed and its advantages and disadvantages discussed. A coreless axial flux PM machine topology was selected for the sustainable wind generator, which uses uncut PMs from HDDs. These magnets were shown to

produce a non-uniform airgap flux-density distribution, which results in unsymmetrical and unbalanced voltage waveforms if conventional tooth-concentrated non-overlapping winding configurations are used. Hence, a concentrated full-pitch overlapping winding configuration was adapted to resemble a conventional wave winding of brushed DC machines, which was shown to produce a balanced and symmetrical 3-phase output. Furthermore, it was shown that this winding configuration reduced the number of coil inter-connecting leads associated with direct-drive wind generators which have many poles.

7.1.3 Analytical Design and Theoretical Performance Analysis of the Sustainable Generator

An analytical model was developed for the sustainable generator using classical machine theory. It is shown that the traditional sizing approach for axial flux machines needs modification to accommodate the design of the proposed machine topology. For the traditional sizing methodology, the ratio of the *inner-to-outer PM radius* is set to a desired value (e.g. maximum efficiency, minimum magnet volume etc.) and the PM length in the radial direction is dependent on the outer radius. The PMs of the HDDs have a fixed shape and therefore have a constant PM length in the radial direction. Hence, the ratio of the PM radii changes as the outer radius is varied. A methodical design approach is presented for calculating the dimensions of the machine, which uses the PM length in the radial direction as a constant. Two generator concepts were considered, namely a single generator with an output power of 277 W and two generator stages connected in series, with each stage producing half of the required output power (138.5 W). The former concept was not considered viable due to concerns about the mechanical integrity associated with its relatively large radius. Thus, the series connected generator stage concept was chosen and it was shown that is met the requirements. With a PM length in the radial direction of 0.015 m, the outer radius of the generator was calculated to 0.203 m. Furthermore, with 16 HDD magnets mounted on the periphery of the machines 22 turns per phase were needed to produce a *rms* back-EMF of 25.55 V. The phase voltage and current were computed to 15.39 V and 3 A respectively. The generator was shown to have a poor voltage regulation, which was due to the relatively high phase resistance of 3.39 Ω.

7.1.4 Numerical Analysis of the Sustainable Generator

The performance of the machine was predicted with 2D-FEA and 3D-FEA, which was found to agree well with the theoretical performance estimation. The 2D-FEA was verified by means of the 3D-FEA, and the 2D-FEA was shown to yield results with sufficient accuracy. A method was presented for accurately calculating the flux per pole from the non-sinusoidal flux-density distribution caused by the uncut HDD magnets. It was found that the flux per pole is under-estimated by 16.3 %, when assuming a sinusoidal flux-density distribution for

the machine. Furthermore, the influence of the thickness of a phase coil on the back-EMF production was investigated, and it was shown that the thickness of a coil side should not exceed 6 mm. Finally, the influence of the magnet dimensions on the performance of the machine was analyzed and it was found to affect the output power of the generator. The back-EMF waveform and harmonic content was unaffected by the dimensions of the PMs.

7.1.5 Prototyping and Testing of the Sustainable Generator

A new test rig for testing large disc-type PM motors was presented and it was shown that the rig met all requirements and performed well. A technique for winding the continuous coil of the wave winding was developed. It was shown that by winding the coil around the developed mold, the phase windings were symmetrical and had a similar resistance.

The performance of the machine as predicted by means of theoretical analysis and the FEA were found to correlate well with the experimental results of the prototyped machine. The wave winding produced a near perfect sinusoidal voltage waveform with a balanced 3-phase output, despite the non-uniform airgap flux-density distribution. The total harmonic distortion of the back-EMF waveform was 4.85 % at a shaft speed of 600 rpm. It was shown that by using the proposed methodical design approach, a reasonable amount of electrical power can be generated when using recycled, cheap and readily available materials and parts. At a shaft speed of 600 rpm and a phase current of 3.3 A, the generator produced 328 W of electrical power. This rated output power is quite reasonable when compared to the most commonly installed 1 kW wind energy systems in South Africa [70][71]. At this operation point, the phase voltage dropped by 25.7 % to 33.2 V, highlighting the poor voltage regulation of the generator, which is due to the relatively high phase winding resistance of 3.33 Ω. The efficiency of the generator at this specific loading point was 70.2 %, which is acceptable for small machines.

7.2 Recommendations

Based on the aforementioned conclusions, the following recommendations are made for future work.

7.2.1 Sustainable Flywheel

It was concluded that the sustainable flywheel is relatively inefficient and that most of the energy produced by the generator will be used to keep the flywheel rotating. Thus, the overall efficiency of the system is low. It is therefore recommended that future work is done on reducing the losses of the flywheel. Some optimization methods include: reducing the frictional losses in the bearings by replacing the conventional bearing with magnetic bearings, which are built from HDD PMs, reducing the windage losses by placing the flywheel into a vacuum chamber and reducing the frictional coefficient of the flywheel by improving the wheel profile.

7.2.2 PM Machine Winding Configuration

For low speed machines, copper losses are the most dominant loss component [69], which was also found to be the case for the prototyped generator (33.3 % of rated output power). Therefore, it is recommended that further work should be done to optimize the overlapping wave winding configuration to reduce the copper losses. An iterative optimization algorithm, which finds the optimal values for the number of turns per phase, the conductor diameter and determines the most effective current loading of the machine, is proposed.

The obvious choice for the winding configuration for coreless PM machines are tooth-concentrated non-overlapping winding configurations, since the copper losses associated with these windings are lower than that of overlapping windings [14]. It was shown throughout this dissertation that tooth-concentrated non-overlapping winding configurations with *equal* tooth widths are not suitable for the sustainable machine topology due to the non-uniform air-gap flux-density distribution. Novel topologies of concentrated single layer tooth-concentrated non-overlapping windings with *unequal* teeth have been introduced in [72][73][74], which mainly reduce torque ripple and optimize the shape of back-EMF waveform. This topology seems very promising to overcome the challenges associated with the non-uniform airgap flux-density distribution, since the coils do not need to be placed uniformly along the perimeter of the machine, and should be investigated for the sustainable PM wind generator.

7.2.3 Increasing the Output Power

The easiest way to increase the output power is by increasing the outer radius of the machine, since the power increases with the cube of the outer radius [15]. However, the sustainable generator has already reached its maximum diameter of around 0.5 m, so alternative methods should be explored. The output power of the generator can be increased by increasing the height of the magnets. This would increase the flux-density in the airgap as expressed in eqn (4.4), and consequently increase the output power of the generator. Practically this can be achieved by removing PMs from their backing plate and placing them on top of an existing uncut HDD PM with backing plate.

Increasing the speed of the generator is another method to increase the output power, since the back-EMF is proportional to the speed of the generator. This can be achieved by implementing a gearbox between the turbine and generator, as is the case for large-scale wind turbines. However, the problems and losses associated with gearboxes offset their advantages, and therefore alternative methods have been researched. The first recommended concept is the incorporation of a magnetic gear into the sustainable wind energy system, which would increase the speed of the generator by introducing minimal losses. The second concept is the pseudo-direct-drive (PDD®), which is a clever combination of a magnetic gear and a PM brushless motor. PMs are essential for both concepts, which could be adapted to use PMs from HDDs, thereby creating a sustainable magnetic gear or a sustainable PDD. The overall efficiency and output power of the generator would improve greatly for both cases, which should be investigated in future.

7.2.4 Thermal Analysis

Since the epoxy resin and MDF stator structure have low thermal properties, a thorough thermal analysis should be conducted for the machine, in order to evaluate the thermal behavior of the proposed sustainable topology. This could reveal exact margins to which an optimized sustainable machine design can be taken.

Appendix A

Detailed Description of the Numerical Analysis

Since the invention of electrical machines, the electromagnetic phenomena found in electrical machines, were modeled using analytical approximation formulas and experimental results. The theoretical analysis is often very difficult to solve and can give erroneous results, since they seldom account for the effect of e.g. leakage flux and iron saturation [75]. Numerical analysis on the other hand, is capable of taking all effects into account and therefore gives very accurate results. With the introduction of fast, affordable and readily available computers, the numerical analysis of electrical machines has become increasingly popular to solve the electromagnetic problems of electrical machines.

2D- and 3D-FEA tools were used to simulate the sustainable generator. The analytical machine model was verified by means of the FEA and its results agreed well with the experimental results. Detailed descriptions of the FEA process, as well as the performed simulations are described in this appendix. The software packages Flux 2D & 3D from Cedrat were used for the simulations [76].

A.1 Solving an Electromagnetic Problem

The FEA process can be divided into three stages when solving an electromagnetic problem, i.e. pre-processing, solving and post-processing of the project.

During the pre-processing stage, geometry ("problem space") is modeled, boundary condition are defined, materials are assigned to the different regions of the geometry and lastly the geometry is meshed, where the problem space is divided into small regions known as finite elements. An external circuit is coupled to the meshed geometry, which defines the electrical set-up of the model. Finally, a solving scenario is defined, which controls the simulations. The simulation can either be controlled by time (time-stepped computation) or by the position of the moving part (position-stepped computation). During the solving stage, the magnetic

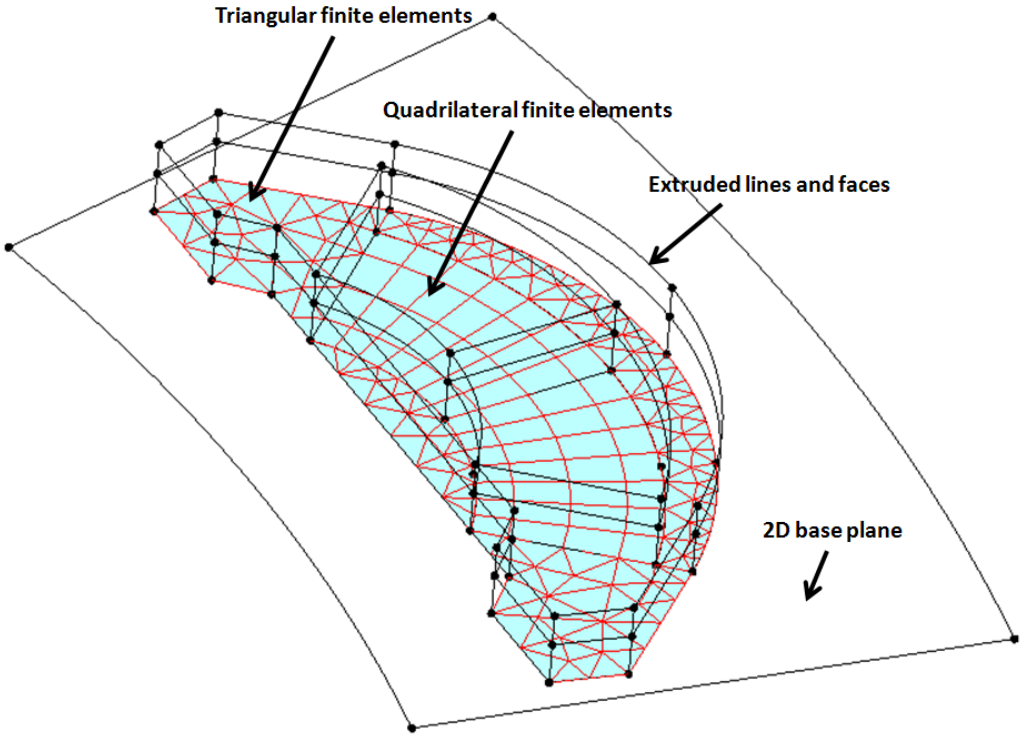

Figure A.1: Building of the 3D model for the sustainable machine

vector potential for each node of the model is calculated. During the post-processing stage, the required results, e.g. the no-load EMF, electromagnetic torque or eddy current losses are computed by manipulation of the magnetic vector potential.

A.2 Building of the Axial Flux PM Machine FEA Models

Literature gives a detailed account on the modeling process of 2D models, and is therefore not be presented is this section. However, information about axial flux 3D models is very limited and the building procedure is described in this section.

In the 3D-FEA, the analyzed machine is modeled to scale. All 3D features of the machine are projected on a 2D base plane. The periodicity of the axial flux machine (even/cyclic or uneven/anti-cyclic) allows a portion of the machine to be modeled; nonetheless the solution can be generated for the whole machine [18]. Once the base plane is constructed and the surface elements are chosen to be triangles or quadrilaterals, the process of extrusion starts. The building procedure is illustrated in Fig. A.1. If the machine has a symmetry condition (tangential or perpendicular flux constraint), the 3D-model can further be halved. The

complete model is then placed in an infinity box, which forces the field lines to follow the boundaries of the model. The model is then meshed, during which the lines, faces and volumes are divided into small finite elements. Depending on the geometry of the different parts of the model, the finite elements will be either tetrahedrons or cuboids. In some FEA packages the airgap area is re-meshed after every computational step, which results in much longer solving time. Flux overcomes this problem by allowing the fixed and rotating parts to "slide" over each other. When using this method, the airgap needs to be meshed very precisely to ensure that all nodes on the sliding surface coincide after every step. For the 2D-model, this is achieved by dividing the sliding surface into equally spaced finite elements as shown in Fig. A.3. For the 3D-model, the sliding surface is meshed with the mapped algorithm, which uses quadrilateral (cuboids) finite elements as shown in Figs. A.1 and A.2. The 2D model contained 3488 2^{nd} order surface finite elements and the 3D model consisted of 167 476 2^{nd} order volume finite elements.

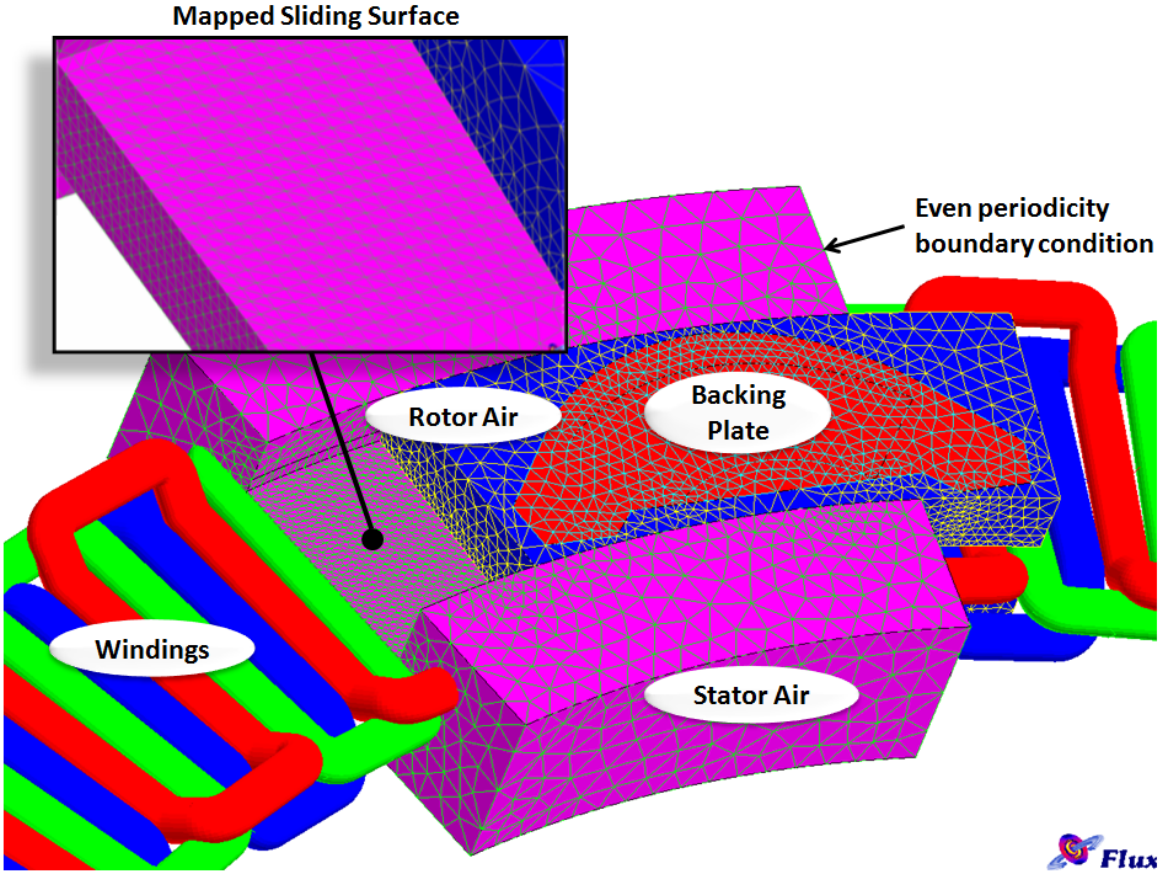

Figure A.2: 3D-meshed model

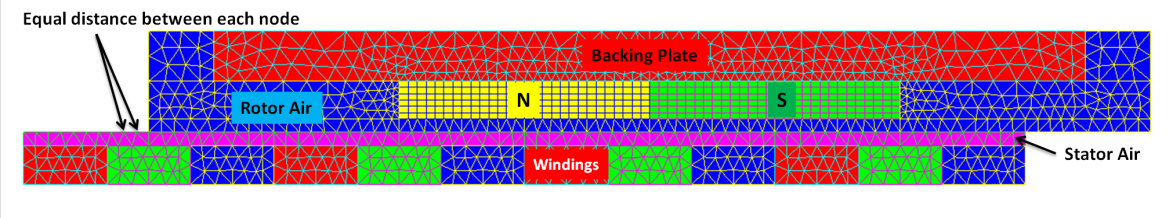

Figure A.3: 2D-meshed model

A.3 Simulations

The FEA simulations performed in this dissertation were generally position controlled. Normally, 20 steps per electrical period were used, which is equal to 0.625 mechanical degrees per step. The rotor rotated at either zero or constant speed, depending on the nature of the simulation. For determining the harmonic content of the back-EMF and terminal voltage the mesh was refined and a smaller step size of 0.141 mechanical degrees was taken.

A.3.1 Simulations at Open-Circuit Condition

The no-load condition was simulated by using the circuits shown in Fig. A.4a and Fig. A.4b for the 2D and 3D simulation respectively. The coil conductors of the circuit are coupled to coils of the meshed geometry. A large resistor (R_{nl} =1 MΩ) is connected across the phases and the neutral point so that the current in the coils is negligible. The rotor rotates at a constant speed. The no-load airgap flux-density, PM flux linkage, no-load back-EMF, and no-load eddy current losses in the PMs and backing plates could be computed from this simulation.

A.3.2 Simulations at Loaded Condition

The loaded condition was simulated by using the same circuit as the no-load. The per phase winding resistance (R_{dc}) is defined in the simulation and the FEA software automatically calculates the voltage drop across the winding resistance when current flows through it. The high ohm no-load resistor (R_{nl}) is replaced by an appropriate load resistor (R_l), which allows the required current to pass through it. The load resistor is calculated by dividing the terminal voltage ($V = E_f - I\,R_{dc}$) by the desired current. The rotor rotates at constant speed and the load voltage, load current, electromagnetic torque and the losses associated with the loading of the machine could be computed from this simulation.

A.3.3 Computation of Eddy Current Losses in the Stator Windings

The simulation of eddy current losses in the stator windings was only conducted in 2D, since its accuracy has been verified by the 3D model. Moreover, the simulation in the 3D environment

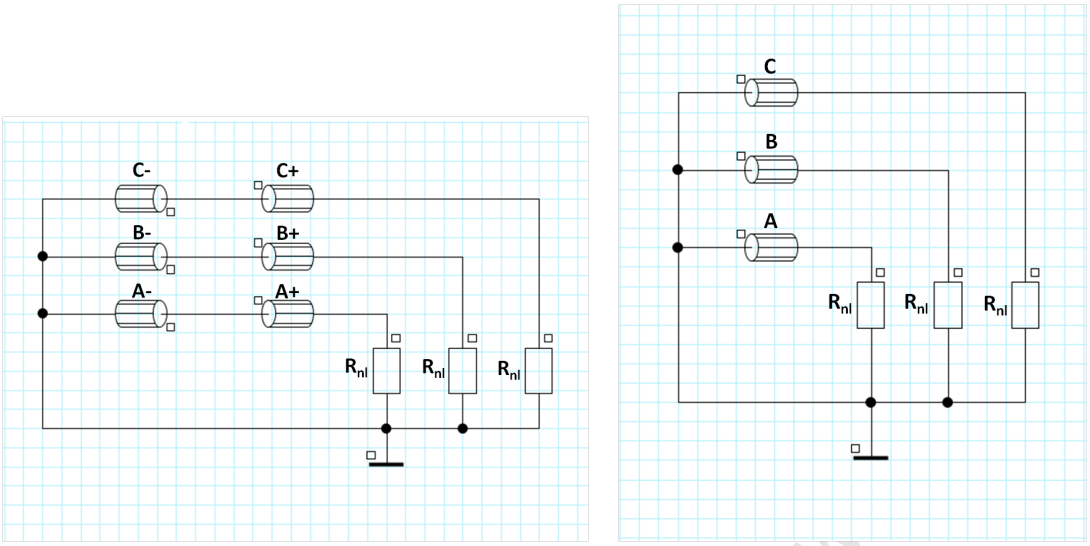

(a) 2D-FEA **(b)** 3D-FEA

Figure A.4: Circuits used for the FEA at no-load condition

is extremely time consuming, because each turn of a phase needs to be modeled individually. In the 2D environment every turn of a phase coil is modeled as a circle in the 2D-plane as shown in Fig. A.5a. Each turn is then coupled to a solid conductor of the circuit as shown in Fig. A.5b. All conductors of one phase are connected in series with a high resistor. The rotor rotates at a constant speed. The eddy current losses could then be calculated directly by computing the joule losses in the solid conductors.

A.3.4 Simulations to Obtain the Winding Inductance

The inductance was simulated with two methods. The first method is presented in the tutorials of Cedrat [56], where the inductance is considered as the incremental derivative of the flux versus the varying current as given by eqn (A.1). The phase DC currents at time zero are injected into the windings as shown in Fig. A.6a, i.e. $I_1 = I_0$ and $I_{2+3} = -I_0/2$. The rotor rotates at constant speed, and the DC current is stepped from zero to rated value (I_0). The flux linking the phase coils is directly computed and divided by the armature current.

$$L_s = \frac{d\psi}{di} = \frac{\Delta\psi_2 - \Delta\psi_1}{i_2 - i_1} \tag{A.1}$$

The second method is most commonly used and is presented in [24] and [77] for example. The rotor is aligned with the d-axis, the B- and C-phases connected together, and a sinusoidal current is applied across the stator as shown in Fig. A.6b. The rotor speed is set to zero and the d-axis inductance can now be calculated by using eqn (A.1). For surface mounted PM

machines, the d- and q-axis inductance is equal to the synchronous inductance, and only the d- or q-axis inductance needs to be computed.

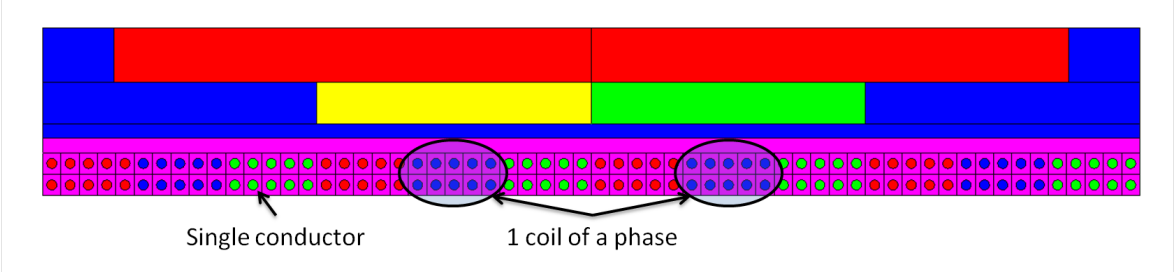

(a) 2D-FEA model

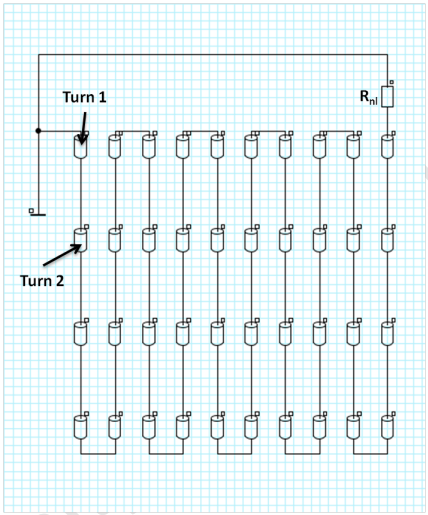

(b) Circuit used for the FEA

Figure A.5: Computation of eddy current losses in the stator windings

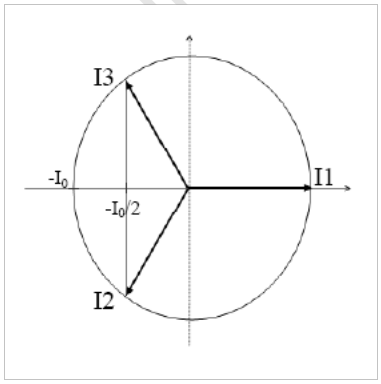

(a) Current phasor at time zero (Method 1) [56]

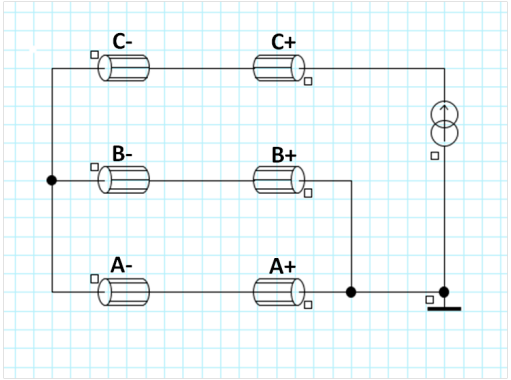

(b) Circuit used for the FEA (Method 2)

Figure A.6: Computation of the winding inductance

References

[1] Statistics South Africa, "Quarterly labour force survey," Tech. Rep., 2010. [Online]. Available: http://www.statssa.gov.za/publications/statsdownload.asp?PPN=P0211&SCH=4852

[2] O. Davidson and S. A. Mwakasonda, "Electricity access for the poor: A study of South Africa and Zimbabwe," *Energy for Sustainable Development*, vol. 8, no. 4, pp. 26 – 40, Dec. 2004.

[3] Energy Information Administration (EIA), "Levelized cost of new electricity generating technologies," [last accessed July 2011]. [Online]. Available: http://www.instituteforenergyresearch.org/wp-content/uploads/2011/02/Levelized-Cost-of-New-Electricity-Generating-Technologie1.pdf

[4] US Energy Information Administration (EIA), "Annual energy outlook 2011," Tech. Rep., Apr. 2011. [Online]. Available: http://www.eia.gov/forecasts/aeo/pdf/0383(2011).pdf

[5] US Environmental Protection Agency, "Fact sheet: Management of electronic waste in the United States," Tech. Rep., May 2005. [Online]. Available: http://www.epa.gov/epawaste/conserve/materials/ecycling/docs/fact7-08.pdf

[6] e-Waste Association of South Africa (eWASA), "eWaste assessment South Africa," Tech. Rep., Nov. 2008. [Online]. Available: http://www.ewasa.org/downloads/files/SA%20e-Waste%20Assessment.pdf

[7] H. van der Linde, "Low-cost wind-driven generator design," in *Proceeding of the 3rd AFRICON Conference*, Sep. 1992, pp. 213 – 216.

[8] A. Nesba, R. Ibtiouen, S. Mekhtoub, O. Touhami, and S. Bacha, "Low-cost wind generator for supplying isolated dc loads," in *International Conference on Clean Electrical Power (ICCEP)*, May 2007, pp. 690 – 695.

[9] S. Hosseini, M. Agha-Mirsalim, and M. Mirzaei, "Design, prototyping, and analysis of a low cost Axial-Flux coreless Permanent-Magnet generator," *IEEE Transactions on Magnetics*, vol. 44, no. 1, pp. 75 – 80, 2008.

[10] Fieldlines 1, "HDD magnet generator," [last accessed July 2011]. [Online]. Available: http://www.fieldlines.com/board/index.php/topic,139473.html

[11] Fieldlines 2, "Wind generator with HDD magnets," [last accessed July 2011]. [Online]. Available: http://www.fieldlines.com/board/index.php/topic,138725.html

[12] P. Krige, "Design and prototyping a permanent magnet generator from scrap," Bsc Thesis, Electrical Engineering, University of Cape Town, Cape Town, South Africa, 2008.

[13] J. Alvey, "Building a wind generator and controller for battery charging applications making use of scrap materials," Bsc Thesis, Electrical Engineering, University of Cape Town, Cape Town, South Africa, 2009.

[14] M. Kamper, R. Wang, and F. Rossouw, "Analysis and performance of axial flux Permanent-Magnet machine with Air-Cored nonoverlapping concentrated stator windings," *IEEE Transactions on Industry Applications*, vol. 44, no. 5, pp. 1495 – 1504, 2008.

[15] J. F. Gieras, R. Wang, and M. J. Kamper, *Axial Flux Permanent Magnet Brushless Machines*, 2nd ed. Springer, Jun. 2008.

[16] J. F. Gieras and M. Wing, *Permanent Magnet Motor Technology Revised*, 2nd ed. CRC Press, Jan. 2002.

[17] R. Wang, M. J. Kamper, K. Van der Westhuizen, and J. F. Gieras, "Optimal design of a coreless stator axial flux permanent-magnet generator," *IEEE Transactions on Magnetics*, vol. 41, no. 1, pp. 55 – 64, Jan. 2005.

[18] A. Novinschi, N. L. Brown, E. Spooner, A. Mebarki, and L. Haydock, "Finite element analysis of a novel axial flux PM synchronous machine with excitation control," in *Power Electronics, Machines and Drives (PEMD). Second International Conference on (Conf. Publ. No. 498)*, vol. 1. IET, Apr. 2004, pp. 420 – 425.

[19] A. Parviainen, J. Pyrhonen, and P. Kontkanen, "Axial flux permanent magnet generator with concentrated winding for small wind power applications," in *IEEE International Conference on Electric Machines and Drives (IEMDC)*. IEEE, May 2005, pp. 1187 – 1191.

[20] D. Gonzalez-Lopez, J. Tapia, R. Wallace, and A. Valenzuela, "Design and test of an axial flux Permanent-Magnet machine with field control capability," *Magnetics, IEEE Transactions on*, vol. 44, no. 9, pp. 2168 – 2173, 2008.

[21] M. Aydin, S. Huang, and T. Lipo, "Design and 3d electromagnetic field analysis of non-slotted and slotted torus type axial flux surface mounted permanent magnet disc machines," in *IEEE International Conference on Electric Machines and Drives (IEMDC)*, 2001, pp. 645 – 651.

[22] Renewable Energy Policy Network for the 21st Century, "Renewables 2011 - Global status report," Tech. Rep., Jul. 2011. [Online]. Available: http://www.ren21.net/Portals/97/documents/GSR/GSR2011_Master18.pdf

[23] World Wind Energy Association, "World wind energy report 2010," Tech. Rep., Apr. 2011. [Online]. Available: http://www.wwindea.org/home/images/stories/pdfs/worldwindenergyreport2010_s.pdf

[24] F. G. Rossouw, "Analysis and design of axial flux permanent magnet wind generator system for direct battery charging applications," Msc Thesis, University of Stellenbosch, Stellenbosch, South Africa, 2009.

[25] S. Heier, *Grid integration of wind energy conversion systems*. Wiley, May 2006.

[26] R. Howell, N. Qin, J. Edwards, and N. Durrani, "Wind tunnel and numerical study of a small vertical axis wind turbine," *Renewable Energy*, vol. 35, no. 2, pp. 412 – 422, Feb. 2010.

[27] M. M. Duquette, "The effect of solidity and blade number on the aerodynamic performance of small horizontal axis wind turbines," Msc Thesis, Department of Mechanical and Aeronautical Engineering, Clarkson University, Potsdam, New York USA, 2002.

[28] M. A. Khan, "Contributions to permanent magnet wind generator design including the application of soft magnetic composites," PhD Thesis, Electrical Engineering, University of Cape Town, Cape Town, South Africa, 2006.

[29] ENERCON, "Product overview of ENERCON wind turbines," [last accessed August 2011]. [Online]. Available: http://www.enercon.de/p/downloads/EN_Produktuebersicht_0710.pdf

[30] A. D. Hansen and L. H. Hansen, "Market penetration of wind turbine concepts over the years," in *Proc. of the European Wind Energy Conference and Exhibition*, Milan, Italy, 2007. [Online]. Available: http://130.226.56.153/rispubl/art/2007_136_paper.pdf

[31] H. Li and Z. Chen, "Overview of different wind generator systems and their comparisons," *Renewable Power Generation, IET*, vol. 2, no. 2, pp. 123 – 138, June 2008.

[32] J. H. J. Potgieter, "Design and analysis of gearless direct-grid permanent magnet induction wind generator," Msc Thesis, University of Stellenbosch, Stellenbosch, South Africa, Mar. 2011.

[33] Y. Chen, P. Pillay, and A. Khan, "PM wind generator comparison of different topologies," in *Conference Record of the 2004 IEEE Industry Applications Conference. 39th IAS Annual Meeting*, vol. 3. IEEE, Oct. 2004, pp. 1405 – 1412.

[34] M. Aydin, S. Huang, and T. Lipo, "Axial flux permanent magnet disc machines: A review," in *Conference Record of SPEEDAM*, May 2004, pp. 61 – 71.

[35] Clean Energy Technologies, "Industrial 500kW wind turbine," [last accessed July 2011]. [Online]. Available: http://www.cleanenergytechnologies.net/industrial/industrial_500kw.html

[36] NGenTec, "Novel generator technology," [last accessed July 2011]. [Online]. Available: http://www.ngentec.com/demonstration.asp

[37] R. Okou, "High speed flywheel and test rig design for energy storage," PhD Thesis, Electrical Engineering, University of Cape Town, Cape Town, South Africa, 2010.

[38] W. Kamkwamba and B. Mealer, *The Boy Who Harnessed the Wind: Creating Currents of Electricity and Hope*. HarperCollins, Jul. 2010.

[39] G. Pauli, *The Blue Economy: 10 Years, 100 Innovations, 100 Million Jobs*. Paradigm Publications, Jun. 2010.

[40] A. Maclaurin, R. Okou, P. Barendse, M. A. Khan, and P. Pillay, "Control of a flywheel energy storage system for rural applications using a Split-Pi DC-DC converter," in *IEEE International Conference on Electric Machines and Drives (IEMDC)*, Niagara Falls, Canada, 2011, in press.

[41] T. Harris, "Sustainable VAWT running in Mitchell's Plain in Cape Town, South Africa."

[42] K. Harris, "DIY horizontal axis wind turbine," [last accessed July 2011]. [Online]. Available: http://www.thekevdog.com/projects/wind_generator/

[43] R. Doller, "Low speed flywheel system built using scrap materials," Bsc Thesis, Electrical Engineering, University of Cape Town, Cape Town, South Africa, Oct. 2010.

[44] I. A. Ferguson, H. J. Geldenhuys, P. Crowdy, and M. N. Bailey, "Distribution standard, planning guidelines, electrification load forecasting," 2003.

[45] P. C. Sen, *Principles of Electric Machines and Power Electronics, Second Edition*, 2nd ed. John Wiley & Sons, Inc., Dec. 1996.

[46] N. Mohan, T. M. Undeland, and W. P. Robbins, *Power Electronics: Converters, Applications, and Design*, 3rd ed. Wiley, Oct. 2002.

[47] H. Piggott, "Hugh piggott's homepage," [last accessed May 2011]. [Online]. Available: http://www.scoraigwind.com/

[48] M. Kamper, A. Rix, D. Wills, and R. Wang, "Formulation, finite-element modeling and winding factors of non-overlap winding permanent magnet machines," in *18th International Conference on Electrical Machines (ICEM)*, 2008, pp. 1 – 5.

[49] J. Soulard, "Investigation on Pole-Slot combinations for Permanent-Magnet machines with concentrated windings," in *International Conference on Electrical Machines (ICEM)*, Cracow, Poland, 2004.

[50] S. E. Skaar, O. Krovel, and R. Nilssen, "Distribution, coil-span and winding factors for PM machines with concentrated windings," in *International Conference on Electrical Machines (ICEM)*, Chania, Greece, 2006.

[51] F. Magnussen and C. Sadarangani, "Winding factors and joule losses of permanent magnet machines with concentrated windings," in *IEEE International Conference on Electric Machines and Drives (IEMDC)*, vol. 1. IEEE, Jun. 2003, pp. 333 – 339.

[52] J. G. Wanjiku, "Design of an axial-flux generator for a small-scale wind electrolysis plant," Msc Thesis, Electrical Engineering, University of Cape Town, Cape Town, South Africa, 2010.

[53] M. Khan and P. Pillay, "Design of a PM wind generator, optimised for energy capture over a wide operating range," in *IEEE International Conference on Electric Machines and Drives (IEMDC)*, May 2005, pp. 1501 – 1506.

[54] S. Huang, J. Luo, F. Leonardi, and T. Lipo, "A general approach to sizing and power density equations for comparison of electrical machines," *IEEE Transactions on Industry Applications*, vol. 34, no. 1, pp. 92 – 97, Jan/Feb 1998.

[55] T. J. E. Miller, *Speed's Electric Motors*. Glasgow, UK: University of Glasgow, 2004.

[56] Cedrat, "Tutorials for Flux 2D and Flux 3D," 2011.

[57] F. Sahin, "Design and development of a high speed Axial-Flux Permanent-Magnet machine," PhD Thesis, Technische Universiteit Eindhoven, Eindhoven, Netherlands, 2001.

[58] H. Jagau, M. Khan, and P. Barendse, "Design of a sustainable wind generator system using redundant materials," in *IEEE Energy Conversion Congress and Exposition (ECCE)*, Phoenix, Arizona, 2011, in press.

[59] Lorenz-Messtechnik, "Lorenz - Torque Transducers," [last accessed July 2011]. [Online]. Available: http://www.lorenz-messtechnik.de/english/products/torque_rotating_contactless.php

[60] Delta Electronics, Inc., "AC Servo Motor and Drive," [last accessed July 2011]. [Online]. Available: http://www.delta.com.tw/product/em/motion/motion_servo/motion_servo_main.asp

[61] Lenze, "Lenze Servo Systems," [last accessed July 2011]. [Online]. Available: http://www.lenze.com/lenze.com_en_active/020_Products/020_Servo_drives/020_Servomotoren/Produktfamilie_Servomotoren.com.jsp?cid=0b0164e0800906ad

[62] Maizey, "Maizey plastics," [last accessed July 2011]. [Online]. Available: http://www.maizey.co.za/

[63] BG Bison, "Supawood," [last accessed July 2011]. [Online]. Available: http://www.pgbison.co.za/panel-products/supawood.html

[64] Y. Çöpür, C. Güler, C. TasçIoglu, and A. Tozluoglu, "Incorporation of hazelnut shell and husk in MDF production," *Bioresource Technology*, vol. 99, no. 15, pp. 7402 – 7406, 2008.

[65] H. Yousefi, "Canola straw as a bio-waste resource for medium density fiberboard (MDF) manufacture," *Waste Management*, vol. 29, no. 10, pp. 2644 – 2648, 2009.

[66] Thistlejoinery, "MDF and the environment," [last accessed July 2011]. [Online]. Available: http://www.thistlejoinery.co.uk/html/mdf_and_the_environment.html

[67] SpanoLux, "MDF manual," [last accessed July 2011]. [Online]. Available: http://www.spanogroup.be/upload/docs/MDF-manual%20ENG%20LOW%20RES.pdf

[68] Perspex South Africa, "Acrylic sheet information manual," [last accessed July 2011]. [Online]. Available: www.perspex.co.za

[69] A. Parviainen, "Design of Axial-Flux Permanent-Magnet low-Speed machines and performance; comparison between Radial-Flux and Axial-Flux machines," D.Sc, Lappeenranta University of Technology, Lappeenranta, Lappeenranta, Finland, 2005.

[70] T. Hancock, "EC schools benefit from wind power," *Engineering News*, vol. 31, no. 14, p. 55, Apr. 2011.

[71] C. Van der Merwe, "Green banking," *Engineering News*, vol. 31, no. 14, p. 79, Apr. 2011.

[72] H. J. Kierstead, R. Wang, and M. J. Kamper, "Torque performance of axial flux permanent magnet fractional open slot machine with unequal teeth," in *Southern African Universities' Power Engineering C0nference (SAUPEC)*, Cape Town, South Africa, 2011, pp. 203 – 207.

[73] J. Cros and P. Viarouge, "Synthesis of high performance PM motors with concentrated windings," *IEEE Transactions on Energy Conversion*, vol. 17, no. 2, pp. 248 – 253, Jun. 2002.

[74] D. Ishak, Z. Q. Zhu, and D. Howe, "Permanent-magnet brushless machines with unequal tooth widths and similar slot and pole numbers," *IEEE Transactions on Industry Applications*, vol. 41, no. 2, pp. 584 – 590, Apr. 2005.

[75] P. Thelin, J. Soulard, H.-P. Nee, and C. Sadarangani, "Comparison between different ways to calculate the induced no-load voltage of pm synchronous motors using finite element methods," in *Proceedings of 4th IEEE International Conference on Power Electronics and Drive Systems*, vol. 2, Oct. 2001, pp. 468 – 474.

[76] Cedrat, "Flux 2D/3D," [last accessed June 2011]. [Online]. Available: www.cedrat.com

[77] F. Meier, "Permanent-Magnet synchronous machines with Non-Overlapping concentrated windings for Low-Speed Direct-Drive applications," PhD Thesis, Royal Institute of Technology, School of Electrical Engineering, Stockholm, Sweden, 2008.